

INVESTIGATION OF ELECTROMIGRATION INDUCED HILLOCK AND
EDGE VOID DYNAMICS ON THE INTERCONNECT SURFACE BY
COMPUTER SIMULATION

A THESIS SUBMITTED TO
THE GRADUATE SCHOOL OF NATURAL AND APPLIED SCIENCES
OF
MIDDLE EAST TECHNICAL UNIVERSITY

BY

AYTAÇ ÇELİK

IN PARTIAL FULFILLMENT OF THE REQUIREMENTS
FOR
THE DEGREE OF MASTER OF SCIENCE
IN
METALLURGICAL AND MATERIALS ENGINEERING

SEPTEMBER 2004

Approval of the Graduate School of Natural and Applied Sciences

Prof. Dr. Canan ÖZGEN
Director

I certify that this thesis satisfies all the requirements as a thesis for the degree of Master of Science.

Prof. Dr. Bilgehan ÖGEL
Head of Department

This is to certify that we have read this thesis and that in our opinion it is fully adequate, in scope and quality, as a thesis for the degree of Master of Science.

Prof. Dr. Tarık Ö. OĞURTANI
Supervisor

Examining Committee Members

Prof. Dr. Erman TEKKAYA (METU, ME)_____

Prof. Dr. Tarık Ö. OĞURTANI (METU, METE)_____

Prof. Dr. Bilgehan ÖGEL (METU, METE)_____

Prof. Dr. Abdullah ÖZTÜRK (METU, METE)_____

Prof. Dr. Yavuz TOPKAYA (METU, METE)_____

I hereby declare that all information in this document has been obtained and presented in accordance with academic rules and ethical conduct. I also declare that, as required by these rules and conduct, I have fully cited and referenced all material and results that are not original to this work.

Name, Last name : Aytaç ÇELİK

Signature :

ABSTRACT

INVESTIGATION OF ELECTROMIGRATION INDUCED HILLOCK AND EDGE VOID DYNAMICS ON THE INTERCONNECT SURFACE BY COMPUTER SIMULATION

ÇELİK, Aytaç

M.S., Department of Metallurgical and Materials Engineering

Supervisor: Prof. Dr. Tarık Ö. OĞURTANI

September 2004, 151 pages

The Electromigration-induced failure of metallic interconnects is a complicated process, which involves flux divergence, vacancy and atom accumulation with or without compositional variations, void and hillocks nucleation, growth and shape changes.

Hillocks and surface void dynamics in connection with the critical morphological evaluation have been investigated in order to understand the conditions under which premature failure of metallic thin interconnects occur.

In this thesis, an interconnect is idealized as a two dimensional electrically conducting strip which contains gaussian form hillock or edge void. Indirect boundary element is used to predict the evolution of the surface after the applied electric field.

Computer simulation results show that the surface crystal structure of is extremely important in the determination of the life time of thin film single crystal interconnect lines. Under the applied electrostatic field not only the degree of rotational symmetry (parameter, m) but also the orientation of the surface plane play dominant role in the development of the surface topology and the formation of the fatal EM induced voids. The degree of anisotropy in the surface diffusion coefficient, and the intensity of the electron wind parameter may have great influence on the evolution regime actually taking place on the surfaces and at sidewalls of the interconnects.

Keywords: Electromigration, Hillocks, Surface Voids, Surface Diffusion.

ÖZ

YÜZEY TEPECİK VE BOŞLUKLARININ ELEKTROGÖÇ NEDENLİ DİNAMİĞİNİN BİLGİSAYAR SİMÜLASYONU ARACILIĞI İLE ARAŞTIRILMASI

ÇELİK, Aytaç

Y.Lisans, Metalurji ve Malzeme Mühendisliği Bölümü

Tez Yöneticisi: Prof. Dr. Tarık Ö. OĞURTANI

Eylül 2004, 151 sayfa

Elektrogöç nedenli metalik ara bağlantı elemanı bozulması akı sapması, boşluk ve atom kümelenmeleri, boşluk ve tepecik kümelenmeleri, büyümesi ve şekil değişikliklerini içeren oldukça karmaşık bir süreçtir.

Bu tezde, metalik ara bağlantı elemanlarının zamansız bozulmalarına neden olan kritik durumları anlamak için yüzeyde yer alan tepecik ve boşluklarının dinamiği ile bağlantılı kritik morfolojik evrim süreçleri araştırılmıştır.

Metalik ara bağlantı elemanı,iki boyutlu ve yüzeyinde gaussian formda tepelik veya boşluk bulunduran iletken serit olarak modellenmiştir. Yüzeyin evrim sürecini dolaylı sınır elemanları metodu kullanılarak tahmin edilmeye çalışılmıştır.

Bilgisayar simülasyonları göstermiştir ki, tek taneli metalik ara bağlantılarının ömrünün tahmininde yüzey kristal yapısı oldukça önemli rol oynamaktadır. Elektrik alan altında yüzey topolojisinin gelişiminde ve elektrogöç nedenli ölümcül boşlukların oluşumunda sadece rotasyon simetrisi değil aynı zamanda yüzey düzleminin yönelimide baskın rol oynamaktadır. Yüzey difüzyonundaki eşyözlüğün miktarının ve elektron rüzgarı katsayısının metalik ara bağlantı elemanlarının yüzeylerinin morfolojik evrimde etkisi büyüktür.

Anahtar Sözcükler: Elektrogöç, tepelikler, yüzey boşlukları, yüzey difüzyonu.

To My Parents...

ACKNOWLEDGEMENTS

I would like to specially thank my advisor Prof. Dr. Tarık Ö. Oğurtanı for all his patience and invaluable guidance.

I would like to thank Dr. Ersin E. Ören for his invaluable help and guidance.

It was a great pleasure to work with laboratory members T. Tolga Ören, Öncü Akyıldız.

I would also like to thank R. Ersen Cerit and Umut Adem for all their encouragement and friendship.

Finally, I deeply thank to my parents and my brother for their support and patience. It is difficult for me to put into words the sacrifices they have done for me.

TABLE OF CONTENTS

ABSTRACT	iv
ÖZ	vi
DEDICATION	viii
ACKNOWLEDGEMENTS	ix
TABLE OF CONTENTS	x
LIST OF TABLES	xiii
LIST OF FIGURES	xiv

CHAPTER

1. LITERATURE SURVEY	1
1.1. Overview.....	3
1.2. The Physical Basis of Electromigration.....	7
1.3. Experimental and Theoretical Observations in Literature	16
1.4. Electromigration Failure	25
1.5. Electromigration Resistance	28

2. MORPHOLOGY AND STRUCTURE OF SURFACES & INTERFACES: IRREVERSIBLE THERMOKINETIC THEORY	
OF SURFACES & INTERFACES.....	36
2.1. Introduction.....	36
2.2. Irreversible Thermokinetics of Micro-Discrete Open Composite Systems with Interfaces.....	37
2.3. Ordinary Point Motion Along the Surface Normal.....	46
i. Internal Entropy Production.....	47
ii. Rate of Entropy Flow.....	53
iii. The Local Rate of Change in the Entropy Density.....	55
2.4. Mathematical Model for the Evolution Dynamics of the Surface of Interconnects	64
3. MATHEMATICAL MODEL & NUMERICAL PROCEDURES.....	68
3.1. Introduction.....	68
3.2. Numerical Methods.....	69
i. Initial System	70
ii. Calculation of the Turning Angles at the Nodes.....	70
iii. Calculation of Node Curvatures.....	71
iv. Calculation of the Local Line Normal Vectors.....	73
v. Calculation of the Electrostatic Potentials by using the Indirect Boundary Element Method Solution of the Laplace's Equation.....	74
vi. Anisotropic Surface Diffusivity	85
vii. Explicit Euler's Method.....	88

viii.	Remeshing.....	88
ix.	The Flowchart of the Program	89
4.	RESULTS AND DISCUSSIONS.....	91
4.1.	Surface Void Configuration.....	94
i.	Two Fold Symmetry, {110} Planes in FCC.....	94
ii.	Four Fold Symmetry, {110} Planes in FCC.....	102
iii.	Six Fold Symmetry, {110} Planes in FCC.....	106
4.2.	Edge Hillock Configuration.....	111
i.	Two Fold Symmetry, {110} Planes in FCC	112
ii.	Four Fold Symmetry, {110} Planes in FCC	117
iii.	Six Fold Symmetry, {110} Planes in FCC	123
5.	CONCLUSIONS.....	129
	BIBLIOGRAPHY.....	130
	APPENDIX	
	Selected Simulation Results	136

LIST OF TABLES

4.1.1	Summary of edge void evolution for two fold crystal symmetry.....	101
4.1.2	Summary of edge void evolution for four fold crystal symmetry.....	106
4.1.3	Summary of edge void evolution for six fold crystal symmetry.....	111
4.2.1	Summary of hillock evolution for two fold crystal symmetry.....	116
4.2.2	Summary of hillock evolution for four fold crystal symmetry.....	123
4.2.3	Summary of hillock evolution for six fold crystal symmetry.....	128

LIST OF FIGURES

1.1.1 Cross-sectional view of the interconnect structure.....	5
1.1.2 Hillock and Void formation sites	7
1.2.1 The driving force for electromigration	9
1.2.2 The diffusion paths of electromigration	11
1.2.3 Schematic illustration of several sites at which flux divergence is expected in metallization systems: (a) triple points in conductor layers; (b) regions where the conductor changes in width; (c) a gold wire/aluminum film contact; (d) at defects in an interconnect.	13
1.2.4 increasing ratio of w/d	14
1.2.5 A narrow slit emanates from a edge void and hillock.....	15
1.4.1 A scanning electron micrograph of a large metal protrusion created in an accumulation region of an interconnect during electromigration.....	27
1.4.2 A scanning electron micrograph of a passivation layer cracked by hillock growth in an underlying interconnect	27
1.5.1 Sketches of the grain structure in a normal polycrystalline interconnect and bamboo structures interconnect.....	29
1.5.2 A comparison of the measured electromigration lifetime f a variety of aluminum-based conductor alloys tested under indetical conditions (Pramanik and Saxena 1983).....	33
2.3.1 Ordinary point motion along surface normal. a) Macro-structure, b) Micro-structure. ABC: interfacial layer and $\delta\eta$: virtual displacement of the ordinary point along surface normal.....	47
2.3.2 Structure of micro-composite system.....	54
3.1.1 The schematic representation of the hillock and edge void together.....	69
3.2.1 The segment turning angle, θ_i , at the node i	71
3.2.2 The unique circle that pass from the three successive void nodes.....	72
3.2.3 The unique circle that pass from the three successive void nodes.....	73
3.2.4 Notation for the FS of Laplace Equation.....	76

3.2.5 Satisfaction of boundary condition in the IBEM.....	77
3.2.6 Limit of integral over AB as Q' approaches Q	79
3.2.7 The connectivity matrix.....	85
3.2.8 Diffusion Anisotropy, $D_{\sigma}^0 = 1$, $A = 5$, $m = 1$ and $\theta = 0$	86
3.2.9 Diffusion Anisotropy, $D_{\sigma}^0 = 1$, $A = 5$, $m = 1$ and $\theta = \pi/3$	86
3.2.10 Diffusion Anisotropy, $D_{\sigma}^0 = 1$, $A = 5$, $m = 2$ and $\theta = 0$	87
3.2.11 Diffusion Anisotropy, $D_{\sigma}^0 = 1$, $A = 5$, $m = 2$ and $\theta = \pi/4$	87
3.2.12 Diffusion Anisotropy, a) $D_{\sigma}^0 = 1$, $A = 10$, $m = 3$ and $\theta = 0$	
b) $D_{\sigma}^0 = 1$, $A = 10$, $m = 3$ and $\theta = \pi/6$	87
3.2.13 Program flow chart	90
4.1 Experimental Setup that is simulated in this thesis.....	91
4.1.1 Initial System with edge void. $\bar{w} = 3$, $\bar{a} = 1$ and $\bar{L} = 20$	94
4.1.2 Surface morphology evolution for edge void. Slit like shape stretched to the windward direction and detachment of the void.....	96
4.1.3 Morphological evolution of the surface at high electron wind intensity (small internal void).....	96
4.1.4 Morphological evolution of edge void to defect free surface (healing effect).....	97
4.1.5 The formation of a Solitary Wave by the transformation of the Gaussian shape, and migration to cathode.....	99
4.1.6 Morphological evolution of the surface at high electron wind intensity (small internal void).....	99
4.1.7 Morphological evolution of edge void to a kink shape disturbance. At final stage fatal failure of interconnect is seen....	103
4.1.8 Morphological evolution of edge void to defect free surface (healing effect)....	104
4.1.9 Morphological evolution of edge void to kink shape.....	107
4.1.10 Formation of a step like surface morphology.....	108
4.1.11 The edge-void transforms into kink-shape morphology.....	110
4.2.1 Initial System with hillock. $\bar{w} = 3$, $\bar{a} = 1$ and $\bar{L} = 20$	112

4.2.2 Morphological evolution of Hillock to perfect flat surface.....	113
4.2.3 Morphological evolution of Hillock to perfect flat surface.....	114
4.2.4 Morphological evolution of Hillock to the bottle neck and detachment of piece of metal.....	115
4.2.5 Hillock morphological evolution to a sawtooth shape.....	118
4.2.6 Morphological evolution of Hillock to perfect flat surface.....	119
4.2.7 Morphological evolution of hillock to finger shape hillock.....	119
4.2.8 Morphological evolution of hillock to sawtooth morphology.....	120
4.2.9 Morphological evolution of hillock to sawtooth morphology.....	121
4.2.10 Formation of oscillatory waves from initial hillock.....	122
4.2.11 Morphological evolution of hillock to the kink-shapes and detachment of piece of metal.....	125
4.2.12 Morphological evolution of hillock to the negative kink-wave.....	126
4.2.13 Morphological evolution of hillock to the oscillatory waves.....	127

CHAPTER 1

LITERATURE SURVEY

Electromigration is the mass transport of metal atoms due to the momentum transfer that results from collision of conducting electrons and diffusing metal atoms. This momentum exchange produces a driving force for metal diffusion that is proportional to the current density.

Electromigration was discovered more than 100 years ago (Geradin, 1861), but it became a concern only when the relatively severe conditions necessary for operation of integrated circuits. Therefore, for at least 100 years, electromigration was an interesting problem only in solid state physics, but of no interests whatsoever commercially.

When electromigration was identified as a concern for the reliability of semiconductor devices, all of this changed (Blech, 1966). This discovery, coming as a surprise to the industry, threatened to stop integrated circuit development until solutions to problem become available. Since then a number of studies have been published and improvements have been reached both in the comprehension of the

physical phenomena involved in electromigration and in the technological solutions employed to limit its effects.

From the model of Black (Black, 1967), an empirical limit of a maximum current in the lines of 5×10^5 A/cm² was fixed in military standards and it helped in keeping the problem under control. However, by increasing the integrated circuits complexity at the end of the seventies, the need for narrower metal lines led to the discovery of the concurrent effect of mechanical stresses, a study started by Black and coworkers in 1976, and of the relationship between line width and grain structure (the so-called bamboo effect). But many of the finer details of these concepts and their interaction to produce reliability problems were not completely appreciated. In the two decades following, these concepts have been refined to the point where a reasonable understanding of what makes a circuits reliable and unreliable has been achieved.

In spite of the exhausting studies, many aspects of electromigration are not well understood. The inadequate theoretical understanding of phenomenon leads to the unsatisfactory results and the complexity of the phenomenon becoming more and more clear.

There are many approaches developed to study electromigration phenomenon. Among these, computer simulation is a powerful and efficient one due to many factors (grain structure, grain texture, interface structure, stresses, film composition, physics of void and hillock nucleation and growth, thermal and current density dependencies, etc.) that influence electromigration and to inability to isolate the effect of these factors experimentally. Also it is easier to consider multiple mechanisms involved in electromigration to enhance the accuracy of the

microscopic variables to reveal the insights of this phenomenon that may be experimentally impossible.

In Chapter 1, literature review for the electromigration and its affect on the surface morphologies are presented. Morphology and structures of surfaces and interfaces are examined by irreversible thermodynamic treatment in Chapter 2. A completely normalized and scaled partial differential equation obtained through this treatment which is useful for computer simulation studies. Numerical methods, used during the solving the partial differential equation, are presented in Chapter 3. Results of the simulation experiments are discussed in Chapter 4. And finally, Conclusion is presented in Chapter 5.

1.1. Overview

The VLSI (Very Large Scale Integration) technology today can make over 10^{10} micro devices on a single chip. The integrated circuits (IC) devices have sophisticated structures involving different materials: metals, semiconductors, ceramics, and polymers. Modern semiconducting chips include a dense array of narrow, thin film metallic conductors that serve to transport current between the devices. These metallic conductors are called as interconnect (Fig. 1.1.1).

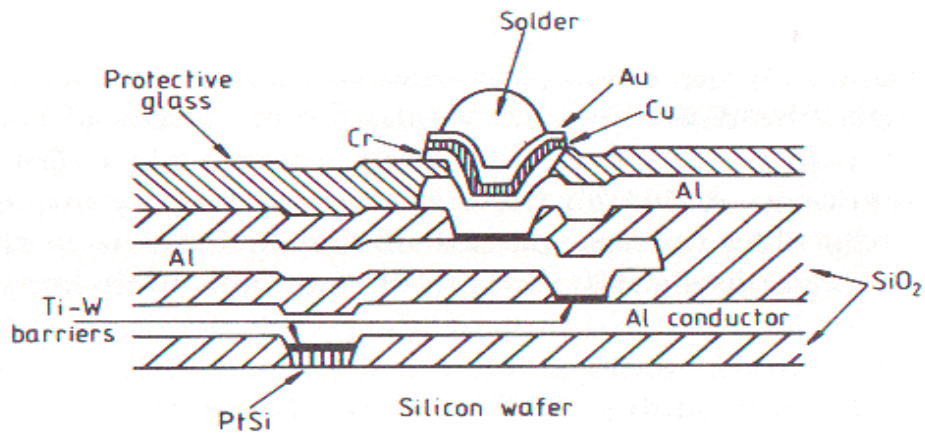


Figure 1.1.1: Cross-sectional view of the interconnect structure

There are large number of interconnects in a single device, and they are predominantly made by aluminum and copper alloys deposited on semiconductor

substrates and covered by passivation layers. The Interconnects generally have complex geometry and cross-section dimensions are on the order of microns or submicron.

The continuing trend towards miniaturization of microelectronic components causes growing demands on both the used materials and fabrication process. A decisive prerequisite to improve the reliability of interconnect lines is to clarify the connection between production conditions of materials and their microstructure on one side and their electrical and mechanical properties on the other side.

With the complexity of today's microelectronics, a phenomenal level of reliability must be maintained for instance, if probability of failure for a transistor is one in a million, and the integrated circuit contains a million transistors, failure is very near certainty. And today's modern integrated circuits can have more than thirty million circuit elements. Therefore, for any acceptable reliability on the chip level, today's circuit element must be among the most reliable things ever built in the world.

However, due to continuing miniaturization of VLSI circuits, thin-film metallic conductors or interconnects are subject to increasingly high current densities. Under these conditions, electromigration can lead to the electrical failure of interconnects in very short times by reducing the circuit lifetime to an unacceptable level (Mahadevan et al., 1996).

The current density carried in an interconnect can be very high indeed, up to $10^7 A/cm^2$ or higher without immediate damage (Wang *et al.*, 1996). It is impossible to pass such a high current density through most bulk conductors because joule heating would melt the material, because joule heating limits the allowable current to about $10^4 A/cm^2$. Because Si substrates on which interconnects are built are very good heat conductors and a thin film conductor is so closely connected to the substrate along whole of its length that joule heating is severe but not catastrophic, even at these very high current densities. On the other hand, in a device having a very dense integration of circuits, the heat management is a serious issue. Typically, a device is cooled by a fan or other means to maintain the operation temperature around 100 C° .

It is thus not surprising that electromigration is often an important phenomenon in metallization systems.

Electromigration causes several different kinds of failure in narrow interconnect. For example, the current density is $10^6 A/cm^2$. Such current density can cause Electromigration in the line at the device operation temperature 100 C° and lead to void formation at the cathode and extrusion at the anode (Fig. 1.1.2). These defects are most persistent and serious reliability failures in thin film integrated circuits. As device miniaturization demands smaller and smaller interconnects, the current density goes up, so does the probability of circuit failure induced by Electromigration.

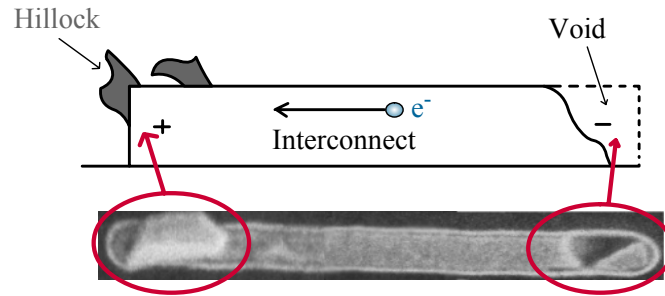


Figure 1.1.2: Hillock and Void formation sites.

We will consider these two modes of failure in interconnect. The first one is surface void failures along the length of the interconnect (called internal failures) and diffusive displacements at the terminals of the interconnect that destroy electrical contact. And the other is the regions of material accumulation in interconnects, leading to the growth of spikes or hillocks (Fig. 1.1.2). Recent research has shown that both of these failure modes are strongly affected by the microstructure of the interconnect and can therefore be delayed or overcome by metallurgical changes that alter the microstructure.

1.2. The Physics of Electromigration

Electromigration is forced atomic diffusion with the driving force due to an electric field and associated electric current in metals (Arzt and Nix, 1991). Electromigration is an important failure mechanism in integrated circuit metallization for two reasons. The first is that metal thin films can dissipate enormous power densities without melting and in turn can carry large current densities ($> 10 \text{ MA/cm}^2$ for aluminum). Thus, the driving force can be quite large.

Second, the ratio of grain boundary/interface area to film cross-sectional area is large, leading to fast diffusion paths and high average mobility. Thus, the diffusion process itself is faster in the interconnects which also enhance the effect.

In any transport process, the flux of material, J_e , can be described by the Nernst-Einstein diffusion relationship

$$J_e = \frac{N \cdot D \cdot F}{k \cdot T} \quad (1.2.1)$$

where N is the density of moving species, D is their mobility and F is the driving force for migration on each of these species. In electromigration, F is the force exerted on a metallic atom by the passage of an electron flux and this force is made up of two contributions. The ionic core of the metal atom experiences a force due to the potential gradient across the conductor. This force is proportional to the valence of the metal and is directed in the opposite direction to the electron flux. The second contribution to F comes from the rather mysterious “electron wind force”, which may be thought of as being due to collisions between the electrons and polarized vacancy-metal ion complexes. The momentum transfer between electron and ion usually results in a force directed in the same direction as the electron flux. In gold and aluminum the electron wind force is measured to be much greater than the field-ion force and so dominates the electromigration process (Fig. 1.2.1).

$$F_{total} = F_{direct} + F_{wind} \quad (1.2.2)$$

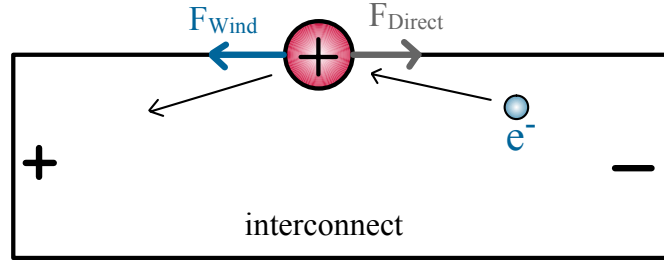


Figure 1.2.1: The driving force for electromigration.

The electron wind force per atom, F , is proportional to the applied electrostatic field:

$$F_{total} = Z^* eE \quad (1.2.3)$$

where the dimensionless number Z^* is known as the effective valance or the effective charge, e is the unit electrostatic charge and E is the electrostatic field.

The Value of Z^* has been expressed by Huntington and Grone 1961, as

$$Z^* = \frac{1}{2} \left(\frac{\rho_d N}{\rho N_d} \right) \frac{m^*}{|m^*|} \quad (1.2.4)$$

where N is the density of conduction electrons, ρ_d is the specific defect resistivity, N_d the defect density, ρ is the metal resistivity, and m^* is the effective

mass of the electrons near the Fermi surface taking part in the momentum exchange. This equation makes clear the close relationship between the fundamental process of electron scattering which contributes to electrical resistivity and the electronic scattering event that is the cause of the electron wind force. It is also clear that the vacancy-ion complex is important in electromigration just as it is in ordinary diffusion transport. Electromigration requires both a force on the metallic atom to encourage it to migrate and a mechanism for migration, in this case vacancy diffusion.

The effective charge Z^* characterizes the momentum transfer, its value which is not well understood, can be inferred from experimental data.

The Einstein - Nerst relation for diffusion in a potential field relates the drift velocity to the electron wind force, F :

$$v_{drift} = BF = \frac{D}{kT} F = \frac{DZ^* eE}{kT} = \frac{DZ^* e\rho j}{kT} \quad (1.2.5)$$

where $D = D_0 \exp\left(\frac{-Q}{kT}\right)$ is the diffusion coefficient, B is the mobility, k is Boltzman's constant, T is absolute temperature and j is the current density.

From Eq. (1.2.5) electromigration induced mass flow is seen to be directly proportional to the current density and the diffusion constant D . The drift velocity, v_{drift} , will be a function of the diffusion pathway and the temperature

dependence of v_{drift} will be characterized by the activation energy of the predominant diffusion mechanism, Q .

In the interconnect, atoms may diffuse along several paths: the surface of metal, the bulk crystal, and the grain boundaries. The schematic picture of these diffusion paths can be seen in figure 1.2.2.

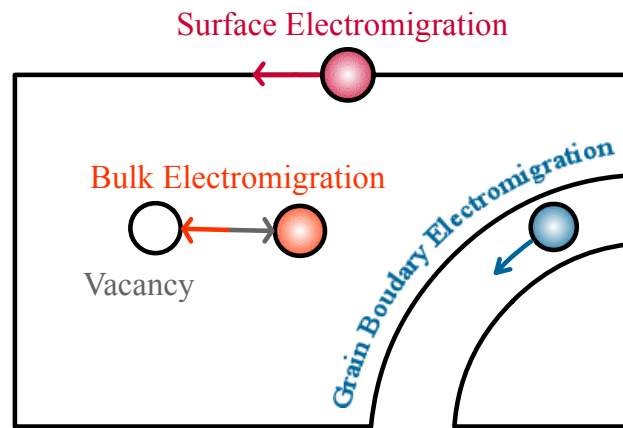


Figure 1.2.2: The diffusion paths of electromigration.

Since atoms are more loosely bonded at the grain boundaries than in the lattice, atoms migrate along grain boundaries more easily than through the grain bulk lattice. Therefore, the grain structure is a critical factor in electromigration. But the surface diffusion is the fastest one due to the easy movement of adatoms at the surface. According to Lloyd (1997), the activation energies, E , for the pathways are in general,

$$E_{surface} = \frac{3}{2} E_{grain\ boundary} = 3E_{bulk} \quad (1.2.6)$$

Mass transport on the surface of interconnects is the sum of the electron field force and capillary forces:

$$J = \frac{D\delta}{\Omega kT} \left(-eZ^* + \Omega\gamma \frac{d\kappa}{dl} \right) \quad (1.2.7)$$

where J is the surface flux of atoms (the number of atoms passing per unit length per time), D is the surface diffusivity, δ is the thickness of the surface layer taking part in the diffusion process Ω is the atomic volume, γ is the surface energy, κ is the curvature of the surface (positive for a rounded void), and l is the arc length.

The physical meaning of Eq. (1.2.7) is that atoms will diffuse in the direction of electron flow if the electric wind force dominates, but toward the position with large curvature if the capillary forces dominate.

From the above discussions it is clear that electromigration could not cause a failure unless there is a divergence in the flux somewhere in the interconnect that allows voids or hillocks to form. Flux divergence will occur whenever there are changes in F , the driving force for electromigration, or in D , the mobility of the diffusing species in the grain boundaries. F depends on Z^* and this parameter can vary both from grain boundary to grain boundary in a polycrystalline film and at contacts between two dissimilar metals. Therefore contact points of substrate and the interconnect, temperature gradient in the interconnect, grain structure, and

photolithography or etch defects are some examples to the source of flux divergence (Fig. 1.2.3).

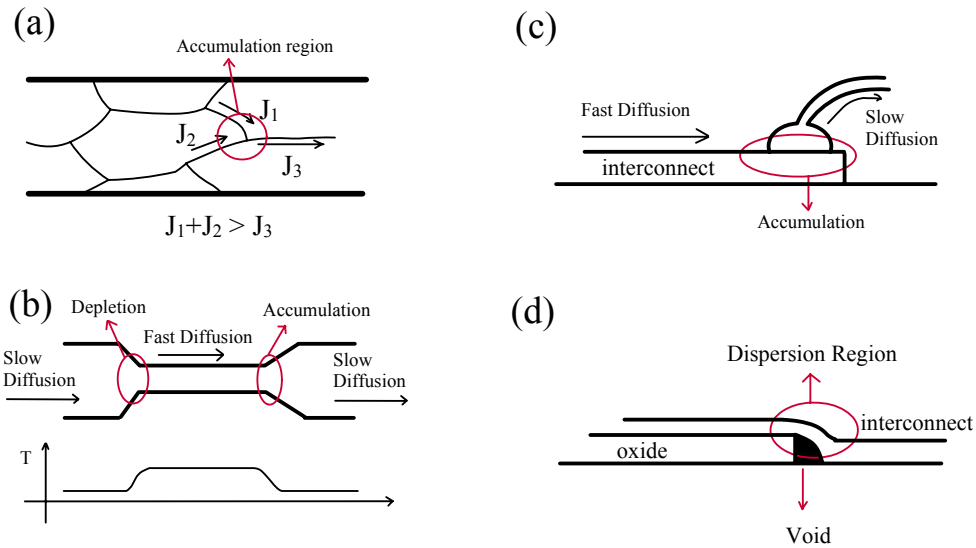


Figure 1.2.3: Schematic illustrations of several sites at which flux divergence is expected in metallization systems: (a) triple points in conductor layers; (b) regions where the conductor changes in width; (c) a gold wire/aluminum film contact; (d) at defects in an interconnect.

These “weak” sites lead to the nucleation of edge voids or hillocks. After the nucleation, growth and movement of the defect is highly dependent on the microstructure and applied electromigration stress.

By decreasing the interconnect width, electromigration failure depends on the grain structure is partially overcome, because interconnect width is strongly related to the grain structure. As the interconnect width decreases or the grain size increases, the grain structure changes from polycrystalline to a near-bamboo structure, and finally

bamboo structure (Fig. 1.2.4). In polycrystalline interconnect grain boundaries form a continuous network. And as discussed above diffusion on grain boundary is faster than diffusion in lattice so the latter is negligible (Wang and Suo, 1996). By contrast, a narrow interconnect has a bamboo-like grain structure, where grain boundaries are far apart and nearly perpendicular to the interconnect direction and hence do not aid in the diffusion process, thus in bamboo-like interconnects grain boundary diffusion becomes negligible. It is observed that the lifetime decreases to a minimum and then increases as the interconnect width decreases (Vaidya et al., 1980). This means that bamboo structured lines tend to show the greatest resistance to the electromigration induced damage.

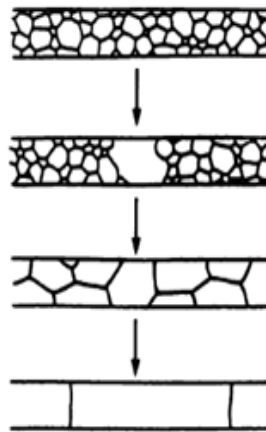


Figure 1.2.4: Increasing ratio of w/d

However, bamboo interconnects are not immortal yet. They still show various type failure modes. After the line is subject to an electric current, the void exhibit extraordinarily complex dynamics: they disappear, re-form, drift, change shape, coalescence, and break up (Marieb *et al.* 1995). A particular behavior has captured

much attention. A void sometimes takes the shape of a slit, lying inside a single grain, severing the interconnect (Sanchez et al., 1992; Rose, 1992). Arzt et al. (1994) reported that a void is round initially; it moves, grows, and then changes shape to become a slit.

Edge void or hillock migration may be understood in terms of surface diffusion. Atoms diffuse on the surface of the void or hillock from one portion to another, so that the void or hillock appears to translate in the grain.

It has been suggested that a rounded void is unstable: the electric current may amplify a small asymmetry in the void shape and cause the void to collapse to a slit (Wang *et al.*, 1996). There are two forces that compete to determine the void shape. Surface tension or “*capillary forces*” favors a rounded void, and electric current “*electron wind force*” favors the slit. That is under the electric current a void collapse to a slit.

Figure 1.2.5 illustrates an edge void and hillock, as atoms diffuse along the surface. For simplicity, it is assumed that the conductor has isotropic surface energy. Both electric field and surface energy drive diffusion:

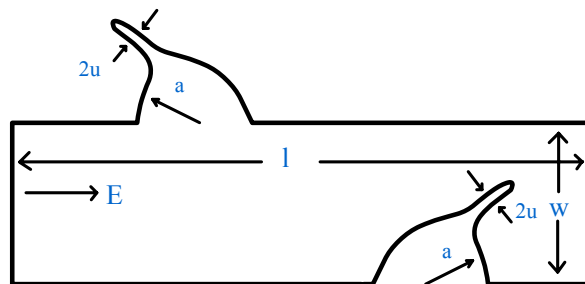


Figure 1.2.5: A narrow slit emanates from an edge void and hillock.

A dimensionless number emerges from Eq. (1.2.7) and this consideration:

$$\chi = \frac{eZ^* \rho J a^2}{\gamma \Omega} \quad (1.2.8)$$

where, a is the size of the void. When χ is small, the surface energy dominates, and the void will remain rounded. When χ is large, the electric field dominates, and the slit will form (Suo, *et al.*, 1994).

1.3 Experimental and Theoretical Observations in Literature

Since 1966, when I.A. Blech reported for the first time the failure of thin aluminum stripes on oxidized silicon due to electromigration, the reliability of the interconnects in integrated circuits has become a major concern for the microelectronics industry. With shrinking dimensions the grain structure of the interconnects have changed from fully polycrystalline to a bamboo structure. It was founded that the lifetime of such conductor lines is increased due to the reduced number of grain boundaries. Nevertheless, such lines do eventually fail due to electromigration, very often by the occurrence of slit-like transgranular voids. The theoretical description of such shape instabilities has since been the subject of several publications.

There are several possible explanations for the formation of the slits. If the void is on a grain boundary, slits may form due to stress induced grain diffusion. Slits may

also form due to electromigration induced surface diffusion. Suo et al. (1994) have pointed out that there are two driving forces for diffusion: electromigration tends to promote the formation of slits, while surface energy tends to favor rounded voids. They suggest that if the electric current density exceeds a critical value, a rounded void will collapse into slit. More detailed computations subsequently confirmed this hypothesis, but showed that if the surface diffusivity is isotropic, slits form parallel to the line and do not cause open circuits. Kraft and Arzt (1997) and Gungor and Maroudas (1998), however, pointed out that open circuits may form by this mechanism if the surface diffusivity is anisotropic. They showed that slit voids will only form in grains with certain crystallographic orientations.

Kraft and Arzt (1997) examined electromigration mechanism in unpassivated interconnects by both experimental and theoretical. Both theoretically and experimentally observed voids showed a typical asymmetric shape with respect to the direction of the electron flow. They conclude that shape of growing voids is largely determined by electromigration induced surface diffusion. Besides shape changes, the simulations also described void motion and growth.

Another typical observation was that bamboo interconnects failed by slit-like voids, which are frequently (but not always) transgranular.

And also their TEM and SEM observations showed that interconnects usually contain large number of voids, and that the behavior of voids is extremely complex. Voids continuously nucleate and heal during the life of the interconnect. Voids also

migrate along the interconnect in the direction of current flow, changing their shape as they do so (Kraft and Arzt, 1994).

During the theoretical studies, they applied finite difference and finite element formulations, and compared the results of numerical simulations with experimental studies. And they developed a model to predict lifetimes of interconnects and to describe the microscopic damage behavior, considering nucleation and growth of voids.

Oren and Ogurtan developed a mathematical model of the mass flow and accumulation on void surfaces under the action of applied electrostatic force field and capillary effects that follows from the conservation laws, and from fundamental postulates of linear irreversible thermodynamics, accounting for the effects of applied electric field and thermal stress.

Numerical simulations were run with and without the surface diffusion anisotropy, with the initial void shape critical asymmetric with respect to the direction of electron flow. These numerical experiments show that the two fold asymmetry in the anisotropic diffusion coefficient becomes a main factor in the development of a straight advancing slit, which accelerates the early open circuit failure due to a sharp slit hitting the upper edge of the interconnect.

Gungor and Maroudas studied the complex problem of linear and non-linear dynamics of transgranular voids in thin films with bamboo grain structure. They simulated the formation of various morphological features: void faceting, formation

of wedge-shaped voids, propagation of slit like and soliton like features. They presented the effects of anisotropy of void surface diffusivity on the stability of the interconnects. They show that morphological instabilities caused by simultaneous action of applied mechanical stress and electric field on transgranular dynamics of voids, and propagation of slits (Gungor and Maroudas, 1998).

Schimschak and Krug (1996) proposed a continuum description of the surface evolution that takes into account electromigration and capillary driven diffusion. For numerical simulations they applied a one dimensional model of interface dynamics, which can be parameterized by a height function. The one dimensional geometry is convenient and relevant to the modeling of shape changes at the edge of an effectively two dimensional conductor line, but becomes inappropriate if the dynamics create overhangs. They studied numerically the motion and the shape evolution of an infinitely extended, isotropic, and homogeneous two dimensional current carrying conductors.

The electromigration induced shape evolution of cylindrical voids was numerically examined in their work at 1998 with the same theoretical background in the previous work. They observed two main routes. If the initial deformation is an elongation in the current direction, protrusion develops at the leading end of the void, and forms a separate daughter void. Since daughter is smaller, it moves rapidly and runs ahead of the mother void. If, on the other hand, the void is initially elongated perpendicular to the current, invagination develops which eventually splits the void horizontally.

Schimschak and Krug add crystal anisotropy to their calculations in the work at 2000 and they simulate edge voids in addition to the voids in the interconnects. In this study, they allow the entire upper edge to evolve, and periodic boundary conditions are imposed along the current direction. And they observe that edge instability can lead to the formation of overhangs which subsequently pinch off and release voids into the interior of the strip.

Their calculations showed that most important parameter effecting void stability and evolution was to be founded to be the ratio of the void size to the characteristic length scale. Also crystalline anisotropy has a decisive influence both on the formation of voids at the edge of the line and on the evolution of fatal slits out of large edge voids.

Mahadevan et al. (1999) studied edge instability in single crystal metal lines, applying a numerical phase field technique. They defined the critical value of the applied current when the edge perturbation grows to become a slit shaped void that spans the wire and leads to electrical failure, reducing the circuit lifetime to an unacceptable level.

Mahadevan and Bradley (1998) used a phase field method to simulate the time evolution of perturbation to the edge of a current carrying single crystal metal line, accounting for electromigration, surface diffusion, and current crowding. They provided a fabrication criterion that ensured the wire will not fail through formation of voids.

Fridline and Bower (1999) studied the effect of anisotropy of the surface diffusivity on the formation and growth of slit like voids, considering an interconnect as a two-dimensional electrically conducting strip that contains an initial semi-circular void. They applied a finite element model to predict the evolution of the void after an electric field was applied to the strip. Their later work accounts for several kinetic processes involved in interconnect failures, including surface diffusion, interface and grain boundary diffusion, and sliding on grain boundaries and the interface between line and elastic passivation.

They categorized the void behavior into three: stable void migration, void collapse, and line severing. Stable void migration was observed at low χ values. For low values of χ the electromigration driving force is weak compared to the surface energy driving force. Therefore these two forces compete and the void adopts a stable equilibrium shape. For the low values of χ void remain stable regardless of the magnitude of the anisotropy in the surface. The symmetry in the surface diffusivity plays a significant role in determining the equilibrium shape of the void. Once the equilibrium reached void migrate in the interconnect. For moderate values of χ and low anisotropy, the electromigration driving force exceeds the stabilizing effect of the surface energy and void tends to collapse, form a slit with alignment between 0° and 45° to the line direction, or break up into smaller voids. For certain values of m , χ , and θ , void may change its shape so as to sever the lines. As the degree of anisotropy is increased, the slit tend to form faster. This causes the void to reach the sides of the interconnect and severing the interconnect.

Suo (1998) considered aluminum interconnects in the presence of insulator and shunts, subjected to temperature change and a direct electric current. He studied the evolution of interconnects into a stable state with a segment of aluminum depleted near the cathode, a linear distribution of pressure in the rest of the line, and no further mass diffusion, and estimated time scale for the interconnect to evolve to the stable state. He described the mechanisms for diffusive processes in solid structures of small feature sizes, between a few to hundreds of nanometers (Suo, 2000). Considering microelectronic and photonic devices, he applied the concept of free energy. The change of free energy defines a thermodynamic force which, in its turn drives the configurational change of the structure. He gave a physical description of forces of diverse origin that occur in thin films of interconnect lines, including elasticity, electrostatics, capillary, electric current. Yu and Suo derived a finite element formulation to model the dynamics of a single pore on moving grain boundary, assuming that the surface diffusion is the dominant process for a small pore to adjust its shape and position.

Sun et al. (1997) considered the evolution of grains in a polycrystalline fiber, and applied a variational approach to microstructure development, which incorporates thermodynamic forces and mass transport mechanisms. The free energy includes the interfacial, elastic, electrostatic and chemical components. The rate process included diffusion, creep, grain boundary motion, and surface or interface reactions. In a later work, sun et al. modeled the dynamics of two grain thin film on a substrate (Suo, Sun and Yang, 1997). They developed a finite element formulation that accounted for surface tension anisotropy, bulk phase free energy density, and finite junction mobility. The authors formulated the laws for the motion of grain

void interfaces and grain boundaries. The large shape changes of solid due to matter diffusion on its surface were studied by Sub and Suo. In addition to surface diffusion, evaporation and condensation were accounted for, and finite element approach was applied to analyze the thermal grooving on polycrystalline surface.

Liniger et al. (2002) studied the kinetics of void growth in unpassivated, electroplated copper lines. The experimental investigation with the scanning electron microscope aimed to study the effect of sample temperature and line-width on the rate of void growth. Voids are observed to grow by consuming grains in a stepwise fashion, either by thinning out from the top down, or through a simple edge displacement mechanism. In all cases, surface diffusion was the primary diffusion path for void growth. In the case of polycrystalline lines, grain boundaries provided a secondary path for copper diffusion. Hillock formation was observed to the anode end of the lines. Over time, hillock formation spread over the entire length of the line with the exception being the area just around the cathode end of the test structure. Voiding was observed to initiate at the cathode end of the line, and to grow along an apparent grain boundary. After some time, the void grew across the entire width of the line, leaving behind a small island of copper.

Experimental and theoretical observations of the failure development during electromigration indicate that electromigration failure is the result of complicated competition between growth, shape change and motion of voids (Arzt *et al.*, 1994). The interaction between these mechanisms is not well understood, although several important attempts have been made to model such events. Void motion has been treated, for example by Ho (1970), with the result that small voids migrate more

rapidly. More recently, Nix and Arzt (1992) have suggested that a critical void size exists for which void motion is minimum; the consequence could be that larger voids catch up with smaller ones, moving more rapidly as they do so and resulting in a catastrophic mechanism of void growth and failure. As described by Børgesen *et al.*, (1991) grain boundaries can trap voids until they reach a critical size.

First, voids are not static but rather show motion, usually in the direction opposing the electron wind. This has been confirmed by several in situ scanning electron microscopy (SEM) on unpassivated Al lines, and field-emission SEM or scanning transmission electron microscopy (STEM), imaging back-scattered electrons, on passivated Al lines. It was also observed that voids can “heal” by breaking up into smaller fragments or grow by coalescing with other voids.

Second, besides “classical” grain boundary diffusion, surface and interface diffusion can contribute to the damage development. This is suggested by in situ transmission electron microscopy (TEM) studies on large grained Al stripes and films revealing voids inside the grains. These voids had grown in the direction of current flow lines, sometimes without apparently interacting with grain boundaries. Thinning of large regions within a single grain in an Al film during electromigration testing was observed. Both observations cannot be explained if the grain boundaries are the only diffusion paths.

Third, voids do not grow in a self-similar manner, but can show significant shape changes. This point has been especially emphasized as a result of electromigration tests that were interrupted several times for damage characterization in an SEM

(Kraft, *et al.*, 1993). A typical void shape has been identified which appears to be necessary for the development of a failure site. The resulting fatal void often has a slit-like morphology, which gives the appearance of a crack perpendicular to the line. Following detailed experimental observations states that these slits frequently do not follow grain boundaries, as might be expected, but are transgranular. Again these observations indicate the necessity to consider mass transport mechanisms other than the grain boundary diffusion.

1.4. Electromigration Failure

In this section we shall consider the two most important modes of failure in metallization systems. The character and density of grain boundaries in the conductors often dictate the manner in which the electromigration failure occurs. We have already seen that local depletion of material during electromigration can result in the formation of voids in interconnects. When grain boundary diffusion is the only significant transport mechanism, these voids will form along the boundaries themselves. Agglomeration of several of these voids can create a crack that extends all the way across the conductor, i.e. an open circuit. While all grain boundary triple points are possible sites for flux divergence in the manner mentioned above, the ones which actually suffer local material depletion depend in a complex manner on the grain boundary geometry and the values of D_{gb} and Z^* in the intersecting boundaries. We can certainly say that void formation is statistically likely to occur somewhere along a interconnect carrying a high current density, but predicting the triple points at which the first crack will appear is difficult. D'Heurle (1971) has

shown some elegant micrographs of crack formation at grain boundaries in current-stressed aluminum interconnects, which emphasize the essentially random nature of the crack-forming process.

Any morphological in-homogeneity in the interconnect will act as a site for flux divergence and will be an exceptionally favored site for crack formation. The thinner regions of interconnects at steps are obvious sites for void nucleation and crack formation. Local variations in grain size will also be likely to provide sites for material depletion. The bimodal grain structure characteristic of zone T is a perfect example of an inhomogeneous grain structure, and films with this grain morphology might be expected to be particularly prone to rapid electromigration failure at the triple points around the large grains. Observations on the formation of cracks at the grain boundaries in thin film conductors suggest that equiaxed large-grained polycrystalline films should be less susceptible to open-circuit failure than fine-grained ones.

Much of the work on electromigration failure has concentrated on crack formation at regions of material depletion. However, there are also regions of material accumulation in metallization structures, leading to the growth of spikes or hillocks. Figure 1.4.1 shows an example of a very large aluminum spike produced by electromigration. Protuberances of this kind can easily grow to form a short-circuit path between adjacent interconnects, and this is the second important mode of electromigration failure. These adjacent interconnects can be vertically above one another in the metallization structure (separated by an

insulating layer of course), or lying in the same plane. Hillock and spike growth can also crack passivation layers, exposing the sensitive aluminum conductors to corrosive attack by the free atmosphere. An example of a passivation layer cracked by hillock growth in the underlying interconnect is shown in figure 1.4.2.

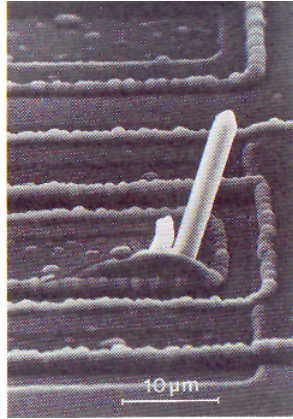


Figure 1.4.1: A scanning electron micrograph of a large metal protrusion created in an accumulation region of an interconnect during electromigration.



Figure 1.4.2: A scanning electron micrograph of a passivation layer cracked by hillock growth in an underlying interconnect.

These micrographs illustrate that electromigration is a very real practical problem in microelectronic metallization, causing both short-circuit and open-circuit failures. We should remember that Joule heating will increase the temperature of the interconnect well above room temperature in many systems, and pure aluminum interconnects typically fail after only a few hours at 250 °C when passing a current of 10^6 A/cm². It has thus proved very important to discover methods by which the resistance of the conductors to electromigration failure can be increased.

1.5 Electromigration Resistance

The simplest method for increasing the resistance of thin film conductors is to remove the principal transport paths, the grain boundaries. Increasing the grain size of thin films by a heat treatment after deposition can reduce the density of grain boundaries and has been found to increase the electromigration lifetimes of interconnects. Single-crystal aluminum films have been shown to have lifetimes as long as 36000 hours at 175 °C while passing $2 \times 10^6 \text{ A cm}^2$, while tests in unusually large-grained aluminum alloy films have also shown very long lifetimes before electromigration failure (Gangulee and D'Heurle 1973). This result is not surprising, as once the rapid diffusion paths are removed the electromigration process can only proceed by lattice diffusion, which is very slow at the low temperatures at which these tests are performed. However, it is difficult to deposit single-crystal metallic films on amorphous substrates like silica. It is also hard to induce grain growth to proceed sufficiently far in a metal thin film to give grains larger than about 10 times the film thickness, even with extended annealing. Some workers have found methods of increasing the grain size of thin films, usually involving the addition of a solute element to the conductor material which increases the grain boundary mobility in the polycrystalline film. These methods are interesting from the point of view of understanding exactly what the interaction is between solute and grain boundaries, but are generally rather hard to use effectively when a complete metallization scheme is being fabricated.

The most elegant way of producing a thin film conductor with a grain structure that will resist electromigration failure is to grow interconnects with the 'bamboo' structure illustrated in figure 1.5.1. Here narrow conductors are deposited and annealed such that almost all the grain boundaries run perpendicular to the long direction of the interconnect. The boundaries will tend to migrate into this configuration to minimize their surface area. Boundaries running across the interconnect cannot contribute to electromigration along the conductor, and by this very simple change in the film morphology the electromigration resistance can be improved hugely. The preparation of conductors with the bamboo structure is usually only possible if the interconnects are rather narrow, but since this is the trend in modern integrated circuit.

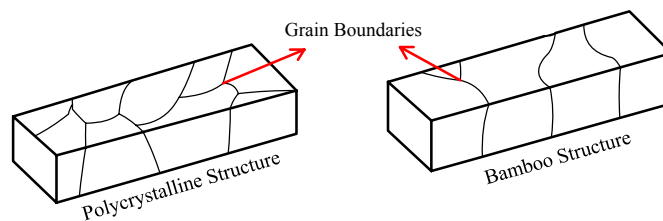


Figure 1.5.1: Sketches of the grain structure in a normal polycrystalline-interconnect and bamboo structured interconnect.

A second method for reducing the rate of electromigration depends on the reduction of grain boundary diffusivity by the addition of a solute element to the conductor material. A small concentration of tantalum in a gold film increases the average activation energy for grain boundary diffusion quite markedly. Additions of copper, magnesium and nickel have a very similar effect in aluminum, reducing the grain boundary diffusion coefficient of aluminum in the boundaries by as much as

two orders of magnitude. Rosenberg et al (1972) have suggested that any solute species which segregates strongly to the grain boundaries in a conductor film will reduce boundary diffusion rates by filling most of the sites in the boundary along which diffusive transport occurs. This is equivalent to saying that the solute segregates to 'vacancy' sites in the structural units at the boundary core where diffusive jumps will be relatively easy. Whether this is correct or not, it is certainly observed that the electromigration lifetime of aluminum interconnects can be increased from about 30 h for pure aluminum to tens of thousands of hours at 175 °C and 2×10^6 A cm² by additions of 4 at.% of copper or 2 at.% of magnesium (D'Heurle and Ho 1978). Hillock formation in aluminum films under compressive stress is also substantially reduced by the same solute additions.

Silicon is added to aluminum metallization to stop spiking under the contact. It is now expedient to add other alloying elements to increase the electromigration resistance. A particularly popular alloy for integrated circuit conductors is aluminum with about 1.5 % silicon and 4 % copper. The silicon can have a small beneficial effect in reducing the grain boundary diffusion rate as well. This composition is very similar to a range of well known age-hardening alloys, and some of the properties of the thin film conductor films can be understood by consideration of phase transformations in alloys of this kind. From the phase diagram and an understanding of the phenomenon of heterogeneous nucleation in poly-crystalline materials, we can predict that the equilibrium structure of aluminum 4 at.% copper thin films should, after annealing at about 150° C, consist of large CuAl₂ precipitates distributed primarily along the grain boundaries in a matrix which is

locally depleted in copper. The regions from which the copper has been depleted will be much more prone to electromigration failure than those which preserve the full 4% copper level. This is because once the copper atoms are no longer segregated to the grain boundaries, the rate of electromigration will immediately increase and cracks will start to nucleate at any flux divergence site. Thus the equilibrium structure of Al-Cu alloy films does not have the optimum distribution of copper for resistance to electro-migration failure.

However, evaporation from Al-Cu alloy sources does not result in homogeneous films because the copper has a higher vapor pressure than the aluminum. The thin film will have most of the copper concentrated close to the substrate and at the top will be severely depleted in this protective element. In addition, the evaporated films will certainly not have the equilibrium structure which we have predicted above. It has been shown that Al-Cu films contain some metastable precipitates immediately after evaporation, but a considerable fraction of the copper remains in solid solution in the aluminum matrix. The nucleation of the CuAl_2 phase in evaporated alloy films has been studied by Vavra and Luby (1980) and Thomas et al (1986) and shown to occur in a very inhomogeneous fashion because of the variations in composition already present in the film and the tendency of this phase to nucleate on the surface of the film and significantly roughen the conductor. These reactions will be greatly accelerated if the films are heated at any temperature below the solvus in the phase diagram. The copper will itself electromigrate away along the grain boundaries, resulting in eventual

depletion of this protective element. The diffusion of copper in grain boundaries in aluminum is quite rapid. Thus, while these alloy interconnects do indeed have improved electromigration resistance by virtue of decreased grain boundary self-diffusion rates, this resistance is eventually degraded by phase transformations, inhomogeneous film structures and electromigration away of the protective element.

We can see that these alloy conductor films are thermodynamically and kinetically extremely unstable, but they do have very good electromigration resistance for the period of time that the copper remains in solid solution, or as a distribution of fine-scale precipitates on the grain boundaries. Al-Si-Cu alloys are very widely used for interconnects in integrated circuit metallization, and the improvement in electromigration resistance which they offer, compared with that of pure aluminum films, is shown in figure 1.5.2. Sputtering techniques are normally used to deposit these alloys because of the improved homogeneity of the films compared with those that are evaporated. We should remember that the alloying element concentration is very high in these alloys and so we might expect their bulk resistivities to be significantly greater than that of pure aluminum. Fortunately, the increase in resistivity is only about 10%, from $2.86\mu\Omega\text{ cm}$ for pure aluminum to $3\mu\Omega\text{ cm}$ for Al-4%Cu-1.5%Si for instance. This level of increased resistivity does not cause any problems in conventional circuit design. However, the dry etching of Al-Cu alloys is significantly more difficult than of pure aluminum and the increased hardness of the films makes wire-bond joints less reliable as well.

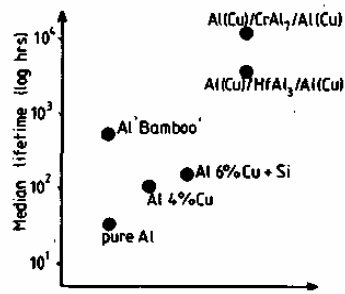


Figure 1.5.2: A comparison of the measured electromigration lifetime of a variety of aluminum-based conductor alloys tested under identical

conditions (Pramanik and Saxena 1983).

Two other methods for increasing the electromigration resistance of aluminum conductors deserve a brief mention: glassing and refractory layer additions. Howard *et al* (1977) have shown that if three-layer interconnects are deposited, Al-4%Cu/Hf/Al-4%Cu for instance, then the electromigration lifetime of the interconnects is longer than for single-layer Al-4%Cu interconnects. These three-layer structures react to form intermetallic phases like HfAl₃ or CrAl₇ at the centre of the conductors, so that there is a refractory alloy layer separating two aluminum alloy films. The improvement in the electromigration lifetime of these interconnects is quite simply because with two parallel conductors the chance of producing an open circuit is much reduced. The refractory layer acts to block void propagation from one conductor to the other and a crack in one of the aluminum layers does not damage the electrical integrity of the conductor as a whole. Electromigration in the intermetallic phases at the centre of the interconnect is very slow and so the possibility of crack formation at the grain boundaries in these layers during electromigration is small. However, Grabe and Schreiber (1983), amongst others, have shown that Al/TiAl₃/Al composite interconnects are particularly prone to the formation of large spikes like those illustrated in figure

1.5.2. These extrusions can cause short circuits between adjacent conductors even when the conductors themselves shown no sign of failing by any electromigration mechanism. In the case of Al-Cu/refractory metal/Al-Cu conductor structures, it has been shown that the presence of the copper in the aluminum films increases the activation energy for formation of the intermetallic compounds at the centre of the interconnect. This effect will increase the stability of the multilayered conductors in service, and it is suggested that the copper decreases the rate of grain boundary diffusion in the aluminum because of the second-phase precipitates blocking these diffusion paths.

Simply adding an adherent, chemically stable and refractory layer to the conventional thin film conductors increases the average electro-migration lifetime by at least a factor of 10. Some typical data on the lifetimes of a range of aluminum-based interconnects are shown in figure 1.5.1, illustrating how both the structure and chemistry of the films have been modified to develop the very stable interconnection systems that are being tested for use in the next generation of integrated circuits.

Finally, let us consider the effect of passivating glass layers on interconnects in which electromigration is occurring. Blech and Herring (1976) have shown that a significant stress gradient exists along an aluminum film in which electromigration is occurring. Aluminum films on a silicon substrate will always be under compression when at elevated temperatures because the thermal expansion coefficient of the metal is much larger than that of silicon. An electromigration

flux of metal ions towards the anode will gradually relieve the stress at the cathode by the depletion of material from this end of the conductor. The stress will not be relieved at the anode, which results in the development of the stress gradient along the conductor. Aluminum will tend to back diffuse along the interconnect under the driving force of this pressure gradient, and this flux will eventually balance the electromigration flux. When this occurs, damage to the interconnect due to electromigration flux divergence will be very much reduced. A glassy passivation layer over the top of the interconnect will also stop the anode end of the conductor plastically deforming by grain boundary sliding and hillock formation under the high local stress. This will increase the stress gradient which is set up along the conductor and the electromigration flux will cease at an earlier stage of the process of material transport. Typical stress levels generated in the soft aluminum are about 10^3 MPa, far in excess of the yield stress. However, when the metal is encapsulated in a relatively 'stiff glass layer, deformation of the aluminum cannot occur. Eventually sufficient stress is generated to crack the passivation layer, and short-circuit failure and atmospheric corrosion of the interconnect can then occur. Lloyd and Smith (1983) have demonstrated that the electromigration resistance of passivated Al-4%Cu conductors depends on the thickness of the glassy layers, and that increases in lifetime of between 5 and 10 times are readily achieved by using sufficiently thick passivation to contain even the highest stresses generated in the metal films. Thus the glass layer which is frequently used to protect aluminum alloys from corrosion has the fortuitous additional advantage of increasing the electromigration lifetime of integrated circuit conductors.

CHAPTER 2

MORPHOLOGY AND STRUCTURE OF SURFACES & INTERFACES: IRREVERSIBLE THERMOKINETIC THEORY OF SURFACES & INTERFACES

2.1. Introduction

To begin with, it will be useful to give a brief definition of the terms morphology and structure. The term morphology is associated with a macroscopic property of solids. The word originates from the Greek $\mu\omicron\rho\phi\eta$, which means form or shape, and here it will be used to refer to the macroscopic form or shape of a surface or interface. Structure, on the other hand, is associated more with a microscopic, atomistic picture and will be used to denote; the detailed geometrical arrangement of atoms and their relative positions in space.

The most general macroscopic approach to a problem in the physics of matter is that of thermodynamics. The specific features associated with a thermodynamic description of an interface are illustrated. This chapter focuses on the irreversible or non-equilibrium thermodynamic treatment of the morphological evolution dynamics of surfaces and interfaces composed of ordinary points (Ogurtani and

Oren, 2001-a). By relying only on the fundamental postulates of linear irreversible thermodynamics as advocated by Prigogine (1961) for the bulk phases, Ogurtani (2000) has obtained a compact and rigorous analytical theory of a network of interfaces by utilizing the more realistic monolayer model of Verschaffelt (1936) and Guggenheim (1959) for the description of interfaces and surfaces. A brief summary of Ogurtani theory is reported recently by Oren and Ogurtani (2002) in connection with their computer simulation studies on the effect of various combinations of grain textures on the life time and the failure mechanisms of thin film interconnects.

2.2. Irreversible Thermo-kinetics of Micro-Discrete Open Composite Systems with Interfaces

The term microscopic region refers to any small two or three-dimensional region containing a number of molecules sufficiently large not only for microscopic fluctuations to be negligible but also all of the intensive properties are homogeneous in space. The composite system, considered here, has at least two physico-chemically distinct domains (or phases in most general sense) separated by thin layers of interfaces, that are not only mutually interacting by the exchange of matter and energy but they are also completely open to the surroundings through the moving or immobile boundaries.

In this theory, the general view points of Guggenheim (1957), Van Der Waals and Bakker (1928) are adopted as far as the interface between any two phases or

domains is concerned. Namely, the interface is autonomous, finite but a thin layer across which the physical properties and/or the structures vary continuously from those of the interior of one phase to those of the interior of the other. Since the interfacial layer is a material system with well-defined volume and material content, its thermodynamic properties do not require any special definition. One may speak of its temperature, entropy, free energy, and composition and so on just as for a homogeneous bulk phase. The only functions that call for special comment are the pressure and the interfacial (surface) tension.

The total reversible work, $\delta\Delta\omega$, done on a flat surface phase with micro-extent, indicated in terms of Δ space-scaling operator, by variations of its volume $d\Delta V_\sigma$, and area $d\Delta A_\sigma$ (keeping its material content unaltered, but stretching) is given by the following well known expression, assuming that the component of the stress tensor along the surface normal P is quasi-homogeneous in the layer and other transverse two components denoted by $[P-Q]$ are equal (rotational symmetry) but heterogeneous (in the absence of electrostatic and other non-mechanical force fields),

$$\delta\Delta\omega = -\bar{P}d\Delta V_\sigma + \gamma d\Delta A_\sigma \quad (2.2.1)$$

where, \bar{P} is the mean isotropic pressure in the layer, and γ is called the surface tension, whose value and the location of the surface in which it acts can be uniquely determined by the knowledge of the transverse component of the stress tensor as demonstrated by Buff (1955). Its value may be given roughly by

$$\gamma = \int_0^{h_\sigma} Q dz, \quad (2.2.2)$$

where, Q is the deviatoric part of the stress tensor and h_σ is the thickness of the surface layer and the integration is performed along the surface normal. The above given expression for the reversible work becomes $-\bar{P}d\Delta V_\alpha$ for a homogeneous bulk phase in the formulation of the first law of thermodynamics. In the conventional theory of irreversible processes (Prigogine, 1961 and Glansdorff and Prigogine, 1971), it has been postulated that the Gibbs formula, which is derived for the reversible changes, is also valid for irreversible processes. However in the present formulation, it is tacitly postulated that the differential form of the Helmholtz free energy in equilibrium thermodynamics has the same validity for irreversible changes. Mathematically this assumption is exactly equivalent to the Gibbs formula used extensively in standard treatment.

The local anisotropic properties of the medium are now automatically embedded in the intensive variables, which are characterized by second order tensors or dyadics. Hence the Helmholtz free energy for an open surface phase of a micro-extent may be written as,

$$d\Delta F_\sigma = -\Delta S_\sigma dT_\sigma - P_\sigma d\Delta V_\sigma + \gamma d\Delta A_\sigma + \sum_i \mu_\sigma^i d\Delta n_\sigma^i - \sum_j \Delta A_\sigma^j d\xi_\sigma^j \quad (2.2.3)$$

where, ΔS_σ denotes the entropy, μ_σ^i denotes the chemical potential, Δn_σ^i is the number of i^{th} chemical species in the micro-element, $d\xi_\sigma^j$ is the extent of the homogeneous j^{th} chemical reaction taking place in the phase under consideration, and ΔA_σ^j is the affinity of the homogeneous j^{th} chemical reaction and is related to the chemical potentials and the stoichiometric numbers as defined by Th. De Donder *et al.* (1936).

In above relationship, it is assumed that, in a single phase only the homogeneous chemical reactions take place and the phase transitions occurring at the mobile boundaries are not considered in the last term. The Helmholtz free energy change due to the passage of the substance i from the phase to the surroundings is accounted by the fourth term in above expression (frozen chemical reactions). Therefore, in the case of a close system, one should subtract only the term given by $\sum_i \mu_\sigma^i d\Delta n_\sigma^i$, which is closely related to the direct exchange of matter with the surroundings.

For the bulk phase, b , (α or β), one may rewrite very similar expression namely,

$$d\Delta F_b = -\Delta S_b dT_b - P_b d\Delta V_b + \sum_i \mu_b^i d\Delta n_b^i - \sum_j \Delta A_b^j d\xi_b^j \quad (2.2.4)$$

In the case of a composite system as defined previously, the total Helmholtz free energy differential can be immediately written down from Eqs. (2.2.3 and 2.2.4) by

using the fact that the extensive thermodynamic quantities are additive. If there would be thermal, hydrostatic and physico-chemical equilibrium in the multi-phase system with plane interfaces there is no need to add subscripts to T, P and μ^i ; there must have values uniform throughout the various phases (bulk and surface) present in the system. For the present non-equilibrium case, first it will be assumed that no such restrictions on the system, but later a system at thermal equilibrium will be treated. For the present problem the system is an open composite system, and it is composed of two bulk phases and two surface phases (the interface between void and interconnect, or interconnect and its surrounding).

The entropy of the system is an extensive property; therefore if the system consists of several parts, the total entropy of the system is equal to the sum of the entropies of each part.

The entropy of any system whether it is close or open can change in two distinct ways, namely by the flow of entropy due to the external interactions, $d\Delta S_{ex}$, and by the internal entropy production due to the changes inside the system, $d\Delta S_{in}$.

Symbolically, one may write this as,

$$d\Delta S = d\Delta S_{in} + d\Delta S_{ex} \quad (2.2.5)$$

The entropy increase $d\Delta S_{in}$ due to changes taking place inside the system is positive for all natural or irreversible changes, is zero for all reversible changes and is never negative.

For a close system external entropy contribution has a very simple definition, and it is given by $d\Delta S_{ex} = \delta q / T$ where δq is the heat received by the system from its surroundings. Now, let us generalize the first law of thermodynamics for any infinitesimal change associated with an open system. For an open system, in which not only the energy but also the matter exchange takes place between the system and its surroundings, the conservation of energy becomes,

$$\delta\Delta\Phi = d\Delta U - \delta\Delta\omega = d[\Delta F + T\Delta S] - \delta\Delta\omega \quad (2.2.6)$$

where, $\delta\Delta\Phi$ is the energy received by the system, in terms of heat and matter transfer processes from the surroundings, $d\Delta U$ is the internal energy change, and $\delta\Delta\omega$ is the reversible work done on the system by the external agents, and this work is equal to $-Pd\Delta V$ or $-[Pd\Delta V - \gamma d\Delta A]$ depending upon whether one deals with the bulk phase or the surface phase, respectively.

Eq. (2.2.6) and Eq. (2.2.3 or 2.2.4) results the following formula in regards to the total differential of the total entropy for the phase, k (surface or bulk phases);

$$d\Delta S = \frac{\delta\Delta\Phi}{T_k} - \sum_i \frac{\mu_k^i}{T_k} d\Delta n_k^i + \sum_j \frac{\Delta A_k^j}{T_k} d\xi_k^j \quad (\text{Total Entropy Change}) \quad (2.2.7)$$

where the summations with respect to i and j indicate summation over different chemical species and over different reactions taking place simultaneously in the same phase, respectively.

The Eq. (2.2.7) can be divided into two parts, similar to the Prigogine (1961), who applied such a splitting procedure to the systems consist of two open phases but the system is closed as a whole:

The first two terms of Eq. (2.2.7), correspond to the rate of external entropy flow term (REF): namely,

$$\frac{d\Delta S_{ex}}{dt} = \frac{1}{T_k} \frac{\delta\Delta\Phi}{dt} - \sum_i \frac{\mu_k^i}{T_k} \frac{d\Delta n_k^i}{dt} \quad (\text{Rate of Entropy Flow (REF)}) \quad (2.2.8)$$

And the last term of Eq. (2.2.7), on the other hand constitutes to the internal entropy production term (IEP): namely,

$$\frac{d\Delta S_{in}}{dt} = \sum_j \frac{\Delta A_k^j}{T_k} \frac{d\xi_k^j}{dt} \geq 0 \quad (\text{Internal Entropy Production (IEP)}) \quad (2.2.9)$$

As one might expect that, the IEP in a single phase directly related to the chemical reactions taking place in the region whether it is closed or open. Only the REF is affected from the matter flow through the open boundary (Ogurtani, 2000).

One may also write down the power dissipation, ΔP , for natural changes, which is a very useful function, which is also known as Helmholtz dissipation function (Haase, 1969), for the treatment of the isothermal processes taking place in multi-

phase systems with uniform and continuous temperature distribution, and it is given by the following expression.

$$\Delta P = T \frac{d\Delta S_{in}}{dt} = \sum_i \Delta A^i \frac{d\xi^i}{dt} \geq 0 \quad (2.2.10)$$

Inequalities given by Eqs. (2.2.9 and 2.2.10) are valid for any natural change, taking place in any phase whether it is bulk or surface. Only difference between these two expressions is that the first one is valid for any type of natural changes taking place in the system but the second one is restricted only for the isothermal natural processes.

For a global composite system having discontinuous (heterogeneous) phases, there are two additional IEP terms, one is due to the internal entropy flow associated with the transfer of chemical species from one subdomain to another subdomain; and the other one is due to the energy transfer between the subdomains of the composite system.

This second IEP term for a composite system immediately drops out if the subdomains have identical temperatures. The total differential of the entropy for such a system is;

$$d\Delta S = \left\{ \begin{array}{l} -\sum_{i,k} \frac{\mu_k^i}{T_k} d\Delta n_{k\leftrightarrow s}^i + \sum_k \frac{\delta\Delta\Omega_{k\leftrightarrow s}}{T_k} \\ -\sum_{i,k} \frac{\mu_k^i}{T_k} d\Delta n_k^i + \sum_k \frac{\delta\Delta\Omega_k}{T_k} + \sum_{j,k} \frac{\Delta A_k^j}{T_k} d\xi_k^j \end{array} \right\} \quad (\text{Total Entropy Change}) \quad (2.2.11)$$

where the double summations with respect to k and i or j indicate summation over various phases (bulk or surface) and over different chemical species or reactions taking place simultaneously in the same phase, respectively. $\delta\Delta\Omega_k$ is the amount of energy transported to the individual phase from the other phases present in the global system due to heat or matter exchange. In Eq (2.2.11), the subscript $k\leftrightarrow s$ indicates that the matter and energy exchange takes place between the phases of the system, k , and the surrounding, s .

By performing the splitting procedure to the Eq. (2.2.11) similar to the single-phase systems: The REF from the surrounding to an open composite system may be written as,

$$\frac{d\Delta S_{ex}}{\delta t} = -\sum_{i,k} \frac{\mu_k^i}{T_k} \frac{d\Delta n_{k\leftrightarrow s}^i}{\delta t} + \sum_k \frac{1}{T_k} \frac{\delta\Delta\Omega_{k\leftrightarrow s}}{\delta t} \quad (\text{REF}) \quad (2.2.12)$$

and the IEP due to the irreversible processes:

$$\frac{d\Delta S_{in}}{\delta t} = -\sum_{i,k} \frac{\mu_k^i}{T_k} \frac{d\Delta n_k^i}{\delta t} + \sum_k \frac{1}{T_k} \frac{\delta\Delta\Omega_k}{\delta t} + \sum_{j,k} \frac{\Delta A_k^j}{T_k} \frac{d\xi_k^j}{\delta t} \quad (\text{IEP}) \quad (2.2.13)$$

On the other hand the first term contributes to IEP of a composite system as long as one has chemical potential differences between respective sub-domains regardless the transfer process isothermal or not.

A comparison of the IEP expressions, for the single-phase system, Eq. (2.2.9), and the composite system, Eq. (2.2.13), immediately shows us that the internal entropy production IEP is not an additive property of a thermodynamic system composed of interacting open sub-systems unless the whole system is in complete physico-chemical equilibrium state (uniform temperature and chemical potential distributions).

At the onset, it should be clearly stated that in the case of an open composite system having only homogeneous chemical reactions with inactive external boundaries (no chemical reaction or phase transition occurring there) any ordinary exchange of matter and/or energy with its surroundings only contributes to the total entropy flow term, and it is noting to do with the IEP.

2.3. Ordinary Point Motion along the Surface Normal

During the derivation of the formula for the global IEP associated with the arbitrary virtual displacement, $d\eta$, of the interfacial loop of a finite thickness, which separates the second phase, denoted by β , from the interconnect, denoted by b , having multi-components, one has to integrate the rate of local entropy density

change along the curved interface in order to obtain desired connection between generalized forces and conjugate fluxes. The rate of local entropy density change is the only quantity, which has the additive property that allows to be integrated. Therefore, not only the local internal entropy production (source term), but also the external entropy flow term should be evaluated for the virtual displacement.

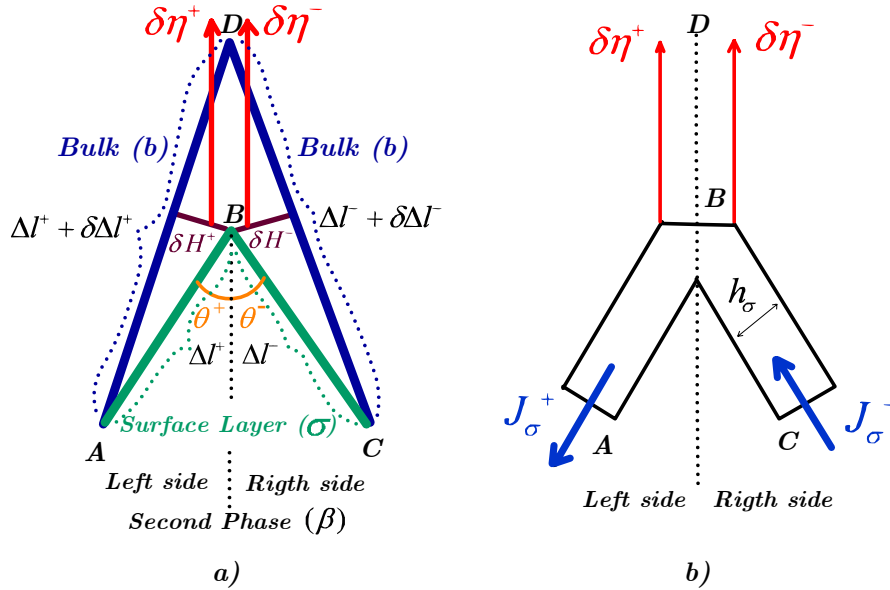


Figure 2.3.1: Ordinary point motion along surface normal. **a)** Macro-structure, **b)** Micro-structure. ABC : interfacial layer and $\delta\eta$: virtual displacement of the ordinary point along surface normal.

i. Internal Entropy Production

The IEP of an open composite system is given by the Eq. (2.2.13). As far as the second phase – interconnect surface layer is concerned, it is assumed that the whole system is in thermal equilibrium, T , and there is no insitu chemical reactions is

taking place. These assumptions drop out the second and the third terms of Eq. (2.2.13), as discussed before. Then the only non-vanishing term of IEP, which represents an additional contribution in the composite system due to internal entropy flow associated with the transfer of chemical species from one sub-domain to another sub-domain, is given by,

$$\frac{\delta\Delta S_{in}}{\delta t} = -\frac{1}{T} \sum_{i,j} \mu_j^i \frac{\delta\Delta n_j^i}{\delta t} \quad (2.3.1)$$

Double summations with respect to i and j indicate summations over different chemical species and over various phases (b, β and σ), respectively.

Now, let us calculate the internal entropy variation for the left hand side sub-system when the ordinary point moves along the surface normal with a distance $\delta\eta^+$. From figure 2.3.1, one immediately finds the following variational relationships among various quantities by assuming that: $\Delta\ell^+ \gg \delta\eta^+$ and $\Delta\ell^- \gg \delta\eta^-$;

$$\delta\Delta\ell^+ = \delta\eta^+ \cos\theta^+ \quad \text{and} \quad \delta H^+ = \delta\eta^+ \sin\theta^+ \quad (2.3.2)$$

$$\delta\Delta n_b^+ = -\frac{1}{2\Omega_b} \Delta\ell^+ \sin\theta^+ \delta\eta^+ \quad (2.3.3)$$

$$\delta\Delta n_f^+ = \frac{1}{2\Omega_v} \Delta\ell^+ \sin\theta^+ \delta\eta^+ \quad (2.3.4)$$

$$\delta\Delta n_\sigma^+ = \frac{h_\sigma}{\Omega_\sigma} \cos\theta^+ \delta\eta^+ \quad (2.3.5)$$

where Ω_σ , Ω_b and Ω_β are the mean atomic specific volumes, associated with the surface layer, bulk and second phases, respectively. $\Delta\ell^+$ and $\Delta\ell^-$ denote segment lengths of the surface layer just next to the ordinary point right and left hand sides, respectively. h_σ is the thickness of the surface layer and assumed to be invariant. $\delta\Delta n_\beta^+$ and $\delta\Delta n_b^+$ are the number of atoms gain in the reaction zones associated with the second phase – interfacial layer and the bulk – interfacial layer respectively, while the transformation processes are taking place there during the virtual displacement of the interfacial layer. $\delta\Delta n_\sigma^+$ is equal to the net atomic gain by the interfacial layer denoted by σ due to enlargement (extension without stretching) of that layer during the displacement operation. δ and Δ are variational and micro-discretization operators, respectively.

One can obtain exactly similar expressions for the other side of the ordinary point, which will be identified by a negative sign as superscript in the following formulas:

$$\delta\Delta\ell^- = \delta\eta^- \cos\theta^- \quad \text{and} \quad \delta H^- = \delta\eta^- \sin\theta^- \quad (2.3.6)$$

$$\delta\Delta n_b^- = -\frac{1}{2\Omega_b} \Delta\ell^- \sin\theta^- \delta\eta^- \quad (2.3.7)$$

$$\delta\Delta n_\beta^- = \frac{1}{2\Omega_\beta} \Delta\ell^- \sin\theta^- \delta\eta^- \quad (2.3.8)$$

$$\delta\Delta n_\sigma^- = \frac{h_\sigma}{\Omega_\sigma} \cos\theta^- \delta\eta^- \quad (2.3.9)$$

Also, one should recall that in the case of multi-component system, the variations in the number of atomic species could be easily obtained by simply multiplying the total atomic number variations by the respective atomic fractions denoted by x_j^i . As an example, the number of chemical species involved in the left and right hand side bulk phases due to the virtual displacement may be given by

$$\delta\Delta n_j^{i+} = x_j^i \delta\Delta n_j^+ \quad (2.3.10)$$

and

$$\delta\Delta n_j^{i-} = x_j^i \delta\Delta n_j^- \quad (2.3.11)$$

Then, one can write down the rate of entropy production due to ordinary point virtual displacement along the surface normal for the left as well as for the right hand side domains;

$$\frac{\delta\Delta S_{in}^+}{\delta t} = \frac{1}{T} \left\{ \left[\sum_i \left(\frac{x_b^{i+}}{\Omega_b} \mu_b^{i+} - \frac{x_\beta^{i+}}{\Omega_\beta} \mu_\beta^{i+} \right) \right] \frac{1}{2} \Delta \ell^+ \sin \theta^+ \right. \\ \left. - \Gamma_\sigma \cos \theta^+ \sum_i x_\sigma^{i+} \mu_\sigma^{i+} \right\} \frac{\delta \eta^+}{\delta t} \quad (2.3.12)$$

and

$$\frac{\delta\Delta S_{in}^-}{\delta t} = \frac{1}{T} \left\{ \left[\sum_i \left(\frac{x_b^{i-}}{\Omega_b} \mu_b^{i-} - \frac{x_\beta^{i-}}{\Omega_\beta} \mu_\beta^{i-} \right) \right] \frac{1}{2} \Delta \ell^- \sin \theta^- \right. \\ \left. - \Gamma_\sigma \cos \theta^- \sum_i x_\sigma^{i-} \mu_\sigma^{i-} \right\} \frac{\delta \eta^-}{\delta t} \quad (2.3.13)$$

where, $\Gamma_\sigma = h_\sigma / \Omega_\sigma$ corresponds to the specific mean atomic density associated with the surface layer.

In above relationship, the special superscript $^+$ or $^-$ has been employed above the atomic fractions as well as the chemical potentials in order to indicate explicitly that those quantities may depend upon the orientation of the local surface normal. One should also recall that for the multi-component surface phases, $\sum \Gamma_\sigma^i \mu_\sigma^i$ is exactly equal to the specific Gibbs free energy density associated with the interfacial layer. This may be denoted by g_σ . Here, $\Gamma_\sigma^i = \Gamma_\sigma x_\sigma^i$, is by definition known as the specific surface concentration of chemical species in surface layer.

The terms appearing in the first group on the right side of Eq. (2.3.1.12) and (2.3.13) such as, $\sum_i \chi_b^i \mu_b^i / \Omega_b$ and $\sum_i \chi_\beta^i \mu_\beta^i / \Omega_\beta$ are the volumetric Gibbs free energy densities. These quantities are denoted by \check{g}_b and \check{g}_β , and associated with the bulk phase and void region having their own instantaneous compositions just next to the hypothetical geometric boundaries of the interfacial layer (reaction fronts or zones). Furthermore, these quantities are related to the specific Gibbs free energy densities by the relationship: $g_\sigma = h_\sigma \check{g}_\sigma$. By using these definitions the following equations are obtained,

$$\frac{\delta \Delta S_m^+}{\delta t} = \frac{1}{T} \left\{ \left(\check{g}_b^+ - \check{g}_\beta^+ \right) \frac{1}{2} \Delta \ell^+ \sin \theta^+ - g_\sigma^+ \cos \theta^+ \right\} \frac{\delta \eta^+}{\delta t} \quad (2.3.14)$$

and

$$\frac{\delta \Delta S_{in}^-}{\delta t} = \frac{1}{T} \left\{ (\tilde{g}_b^- - \tilde{g}_\beta^-) \frac{1}{2} \Delta \ell^- \sin \theta^- - \tilde{g}_\sigma^- \cos \theta^- \right\} \frac{\delta \eta^-}{\delta t} \quad (2.3.15)$$

The total internal entropy production is:

$$\begin{aligned} \frac{\delta \Delta S_{in}}{\delta t} &= \frac{\delta \Delta S_{in}^+}{\delta t} + \frac{\delta \Delta S_{in}^-}{\delta t} \\ &= \frac{1}{T} \left\{ -\frac{\Delta \ell}{2} (\tilde{g}_{\beta b}^+ \sin \theta^+ + \tilde{g}_{\beta b}^- \sin \theta^-) \right. \\ &\quad \left. - (\tilde{g}_\sigma^+ \cos \theta^+ + \tilde{g}_\sigma^- \cos \theta^-) \right\} \frac{\delta \eta}{\delta t} \end{aligned} \quad (2.3.16)$$

where $\tilde{g}_{\beta b} = (\tilde{g}_f - \tilde{g}_b)$, and it corresponds by definition to the volumetric density of Gibbs Free Energy of Transformation (GFET) (negative of the affinity of an interfacial reaction such as condensation or adsorption, $\tilde{g}_{\beta b} > 0$) associated with the transformation of the bulk phase into the realistic second phase, which contains chemical species even though they are present in a trace amount. In the case of thermostatic equilibrium between a second phase and an adjacent bulk phase, GFET becomes identically equal to zero, if the reaction front would be a flat interface. There is a very simple connection between this quantity GFET and the Specific Gibbs Free Energy of transformation between the parent phase and the second phase that may be given by $\tilde{g}_{\beta b} = \tilde{g}_{\beta b} h_\sigma$. By dividing both sides of the Eq. (2.3.16) by $\Delta \ell$, it is obtained that,

$$\frac{\delta \Delta S_{in} / \Delta \ell}{\delta t} = -\frac{1}{2T} \left\{ \begin{array}{l} \left(\tilde{g}_{\beta b}^+ \sin \theta^+ + \tilde{g}_{\beta b}^- \sin \theta^- \right) \\ + \left(g_{\sigma}^+ \frac{\cos \theta^+}{\Delta \ell / 2} + g_{\sigma}^- \frac{\cos \theta^-}{\Delta \ell / 2} \right) \end{array} \right\} \frac{\delta \eta}{\delta t} \quad (2.3.17)$$

Now if one applies the limiting procedures such as; first with respect to $\delta t \rightarrow 0$, and then $\Delta \ell \rightarrow 0$, and recalls the definition of the local radius of curvature, κ , which is given by;

$$\kappa = \lim_{\Delta \ell \rightarrow 0} \left(\frac{\cos \theta}{\Delta \ell / 2} \right) \quad (2.3.18)$$

and also keeps in mind that $\lim_{\Delta \ell \rightarrow 0} \theta^{\pm} = \frac{\pi}{2}$, $\tilde{g}_{\beta b}^+ = \tilde{g}_{\beta b}^- = \tilde{g}_{\beta b}$ and $g_{\sigma}^+ = g_{\sigma}^- = g_{\sigma}$, one

immediately obtains the following continuum relationship for the IEP,

$$\frac{d \Delta \hat{S}_{in}}{dt} = -\frac{1}{T} (\tilde{g}_{\beta b} + g_{\sigma} \kappa) \frac{d \eta}{dt} \quad (\text{erg}^{\circ} \text{K} / \text{cm} / \text{sec}) \quad (2.3.19)$$

where $d \Delta \hat{S}_{in} / dt$ is the surface density of IEP associated with ordinary points.

ii. Rate of Entropy Flow

Similarly, the external entropy accumulation in the surface phase due to flow of chemical species, i , along the surface layer, J_{σ}^i , and the perpendicular incoming

flux intensities from the bulk, \hat{J}_b^i , and the void, \hat{J}_β^i , phases, can be calculated by using the law of conservation of entropy without the source term or IEP.

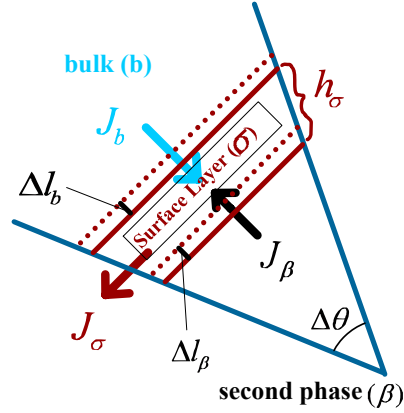


Figure 2.3.2: Structure of micro-composite system.

From figure 2.3.2 it can be written as,

$$\begin{aligned}
 \frac{d\Delta\hat{S}_{ex}}{dt} &= -\frac{\partial}{\partial\ell} J_\sigma + \hat{J}_b + \hat{J}_\beta \\
 &= -\sum_i \frac{\partial}{\partial\ell} \left(\frac{\mu_\sigma^i}{T_\sigma} J_\sigma^i \right) + \sum_i \frac{\mu_b^i}{T_b} \hat{J}_b^i + \sum_i \frac{\mu_\beta^i}{T_\beta} \hat{J}_\beta^i \\
 &= -\sum_i \frac{\partial}{\partial\ell} \left(\frac{\mu_\sigma^i}{T_\sigma} x_\sigma^i J_\sigma \right) + \sum_i \frac{\mu_b^i}{T_b} x_b^i \hat{J}_b + \sum_i \frac{\mu_\beta^i}{T_\beta} x_\beta^i \hat{J}_\beta
 \end{aligned} \tag{2.3.20}$$

where, \hat{J}_v and \hat{J}_b are the total atomic flux intensities in such directions that they are perpendicular and oriented towards the interfacial layer, just at the reaction fronts between the second phase and the interfacial layer and the bulk phase and the interfacial layer, respectively.

By remembering the definitions of the volumetric Gibbs free energy densities, \tilde{g}_k , given by $\sum_i x_k^i \mu_k^i / \Omega_k$, where k represents the different phases, and keeping in mind that the global system is in thermal equilibrium, Eq. (2.3.20) can be rewritten as:

$$\frac{d\Delta\hat{S}_{ex}}{dt} = -\frac{\Omega_\sigma}{T} \left[\frac{\partial}{\partial \ell} (\tilde{g}_\sigma J_\sigma) + \tilde{g}_\sigma (\hat{J}_b + \hat{J}_\beta) \right] \quad (2.3.21)$$

where $d\Delta\hat{S}_{ex}/dt$ is the surface density of REF associated with ordinary points.

In this formula it is also assumed that the mean atomic specific volumes of the bulk and the second phases are nearly equal to that of the interfacial layer.

iii. The Local Rate of Change in the Entropy Density

The total entropy production has to be calculated since only this term has the additive property that will be used to calculate the total entropy production of the whole surface layer under isothermal condition by a path integration procedure. By using Eqs. (2.3.19 and 2.3.21);

$$\begin{aligned} \frac{d\Delta\hat{S}}{dt} &= \frac{d\Delta\hat{S}_{in}}{dt} + \frac{d\Delta\hat{S}_{ex}}{dt} \\ &= -\frac{1}{T} \left\{ (\tilde{g}_{\beta b} + g_\sigma \kappa) \frac{d\eta}{dt} + \Omega_\sigma \left[\frac{\partial}{\partial \ell} (\tilde{g}_\sigma J_\sigma) + \tilde{g}_\sigma (\hat{J}_b + \hat{J}_\beta) \right] \right\} \end{aligned} \quad (2.3.22)$$

In order to calculate the global rate of entropy change of the whole curved interfacial layer, which is between the second phase region and the bulk phase, let first take the line integral of Eq. (2.3.22) all along the closed curved interface, represented by C which may be situated at a point denoted by the open interval $(-\varepsilon, +\varepsilon)$, where $\varepsilon \rightarrow 0$. This interface is represented by C^o and equal to $C - (-\varepsilon, +\varepsilon)$.

$$\oint_{C^o} d\ell \frac{d\Delta\hat{S}}{dt} = \lim_{\varepsilon \rightarrow 0} \int_{+\varepsilon}^{-\varepsilon} d\ell \frac{d\Delta\hat{S}}{dt} \quad (2.3.23)$$

$$= -\frac{1}{T} \lim_{\varepsilon \rightarrow 0} \int_{+\varepsilon}^{-\varepsilon} d\ell \left\{ \begin{aligned} & \left(\tilde{g}_{\beta b} + g_{\sigma} \kappa \right) \frac{d\eta}{dt} \\ & + \Omega_{\sigma} \left[\frac{\partial}{\partial \ell} (\tilde{g}_{\sigma} J_{\sigma}) + \tilde{g}_{\sigma} (\hat{J}_b + \hat{J}_{\beta}) \right] \end{aligned} \right\}$$

In the absence of the particle source and sink terms, the atomic flux divergence is proportional with the amount of mass accumulated or depleted on an interfacial layer, which causes the interface to move in a local normal direction. However in this formulation a more general situation, namely, the additional entropy source terms associated with the normal components of the atomic flows coming from the bulk phase, and the void region due to condensation or evaporation processes that may be summarized by, $\hat{J}_{b\beta} = \hat{J}_b + \hat{J}_{\beta}$, is considered. Hence, the following expression can be written for the conservation of atomic species during the virtual displacement of curved interface having no stretching and thickness variations:

$$\left[(c_b - c_\beta) - h_\sigma \bar{\kappa} c_\sigma \right] \frac{d\eta}{dt} = \sum_i \frac{\partial J_\sigma^i}{\partial \ell} - \sum_i (\hat{J}_b^i + \hat{J}_\beta^i) = \frac{\partial J_\sigma}{\partial \ell} - \hat{J}_{b\beta} \quad (2.3.24)$$

where, c_b , c_β and c_σ are the atomic volumetric concentrations associated with the bulk, second phase and surface phases, respectively. Now if one considers the following plausible and highly accurate approximations for second phase, which may be treated as polyatomic dilute gas, such as: $c_\beta = 0$ and $h_\sigma \bar{\kappa} = 0$. One would get the following results using the fact that $\Omega_b = c_b^{-1}$, which is mostly adapted in the literature (Guggenheim, 1959 and Ogurtani and Oren, 2001-a):

$$\frac{d\eta}{dt} = \bar{n} \cdot \frac{d\bar{r}}{dt} = \Omega_b \left(\frac{\partial J_\sigma}{\partial \ell} - \hat{J}_{b\beta} \right) \quad (2.3.25)$$

where, \bar{n} and \bar{r} are the surface normal and the position vectors, respectively.

Now, let us substitute above identity into Eq. (2.3.23), and also remember that it is assumed that the mean atomic specific volume of the bulk phase is nearly equal to that of the interfacial layer.

$$\oint_{c^0} d\ell \frac{d\Delta\hat{S}}{dt} = -\frac{\Omega_\sigma}{T} \lim_{\varepsilon \rightarrow 0} \int_{+\varepsilon}^{-\varepsilon} d\ell \left\{ \begin{array}{l} \left(\bar{g}_{\beta b} + g_\sigma \kappa \right) \left(\frac{\partial J_\sigma}{\partial \ell} - \hat{J}_{b\beta} \right) \\ + \left[\frac{\partial}{\partial \ell} (\bar{g}_\sigma J_\sigma) + \bar{g}_\sigma \hat{J}_{b\beta} \right] \end{array} \right\} \quad (2.3.26)$$

In order to apply the integration by parts let us write Eq. (2.3.26) in the following form,

$$\oint_{C^0} d\ell \frac{d\Delta\hat{S}}{dt} = -\frac{\Omega_\sigma}{T} \lim_{\varepsilon \rightarrow 0} \left\{ \begin{aligned} & \int_{+\varepsilon}^{-\varepsilon} d\ell \left[(\tilde{g}_{\beta b} + g_{\sigma\kappa}) \frac{\partial J_\sigma}{\partial \ell} \right] \\ & - \int_{+\varepsilon}^{-\varepsilon} d\ell \left[(\tilde{g}_{\beta b} + g_{\sigma\kappa}) \hat{J}_{b\beta} \right] \\ & + \int_{+\varepsilon}^{-\varepsilon} d\ell \frac{\partial}{\partial \ell} (\tilde{g}_\sigma J_\sigma) + \int_{+\varepsilon}^{-\varepsilon} d\ell (\tilde{g}_\sigma \hat{J}_{b\beta}) \end{aligned} \right\} \quad (2.3.27)$$

The first group of terms on the right side of the Eq. (2.3.27) can be integrated by parts, as shown below; In order to save the space the left side of the equation are not shown in the following two equations.

$$= -\frac{\Omega_\sigma}{T} \lim_{\varepsilon \rightarrow 0} \left\{ \begin{aligned} & \int_{+\varepsilon}^{-\varepsilon} d\ell \frac{\partial}{\partial \ell} \left[(\tilde{g}_{\beta b} + g_{\sigma\kappa}) J_\sigma \right] - \int_{+\varepsilon}^{-\varepsilon} d\ell \left[J_\sigma \frac{\partial}{\partial \ell} (\tilde{g}_{\beta b} + g_{\sigma\kappa}) \right] \\ & - \int_{+\varepsilon}^{-\varepsilon} d\ell \left[(\tilde{g}_{\beta b} + g_{\sigma\kappa}) \hat{J}_{bf} \right] \\ & + \int_{+\varepsilon}^{-\varepsilon} d\ell \frac{\partial}{\partial \ell} (\tilde{g}_\sigma J_\sigma) + \int_{+\varepsilon}^{-\varepsilon} d\ell (\tilde{g}_\sigma \hat{J}_{b\beta}) \end{aligned} \right\} \quad (2.3.28)$$

After some manipulations and rearrangements,

$$= \frac{\Omega_\sigma}{T} \lim_{\varepsilon \rightarrow 0} \left\{ \begin{aligned} & \int_{+\varepsilon}^{-\varepsilon} d\ell \left[J_\sigma \frac{\partial}{\partial \ell} (\tilde{g}_{\beta b} + g_{\sigma\kappa}) \right] - \left[(\tilde{g}_{\beta b} + g_{\sigma\kappa}) J_\sigma \right]_{+\varepsilon}^{-\varepsilon} \\ & + \int_{+\varepsilon}^{-\varepsilon} d\ell \left[(\tilde{g}_{\beta b} + g_{\sigma\kappa}) \hat{J}_{b\beta} \right] - \left[\tilde{g}_\sigma J_\sigma \right]_{+\varepsilon}^{-\varepsilon} - \int_{+\varepsilon}^{-\varepsilon} d\ell (\tilde{g}_\sigma \hat{J}_{b\beta}) \end{aligned} \right\} \quad (2.3.29)$$

At the final step after the integration by parts procedure, one should carefully split the global rate of entropy change into two parts, namely the REF term and the IEP term by carefully inspecting the individual contributions in Eq. (2.3.29).

$$\frac{d}{dt} S_{REF} = \frac{\Omega_\sigma}{T} \lim_{\varepsilon \rightarrow 0} \left\{ - \int_{+\varepsilon}^{-\varepsilon} d\ell \left(\tilde{g}_\sigma \hat{J}_{b\beta} \right) - [\tilde{g}_\sigma J_\sigma]_{-\varepsilon} + [\tilde{g}_\sigma J_\sigma]_{+\varepsilon} \right\} \quad (2.3.30)$$

where, the first term is the integrated entropy flow to the interfacial layer from the embedding parent phases through the incoming matter flux, $\hat{J}_{b\beta}$.

The remaining terms of Eq. (2.3.29) are related to the IEP and given by,

$$\frac{d}{dt} S_{IEP} = \frac{\Omega_\sigma}{T} \lim_{\varepsilon \rightarrow 0} \left\{ \int_{+\varepsilon}^{-\varepsilon} d\ell \left[J_\sigma \frac{\partial}{\partial \ell} (\tilde{g}_{\beta b} + g_\sigma \kappa) \right] + \int_{+\varepsilon}^{-\varepsilon} d\ell \left[(\tilde{g}_{\beta b} + g_\sigma \kappa) \hat{J}_{b\beta} \right] \right\} \quad (2.3.31)$$

$$\left. \begin{aligned} & - [(\tilde{g}_{\beta b} + g_\sigma \kappa) J_\sigma]_{-\varepsilon} + [(\tilde{g}_{\beta b} + g_\sigma \kappa) J_\sigma]_{+\varepsilon} \end{aligned} \right\}$$

This original result clearly confirms that the bulk flow of particles or substances for nonviscous systems appears to be a reversible phenomenon as first discovered by Prigogine (1961), in another content using the velocity of the centre of gravity as a reference system in the calculation of the possible singularity. In the absence of this singularity, the last two terms of Eqs. (2.3.30 and 2.3.31), become identically zero and drop out completely.

Here it should be clearly stated that the singularities have to be treated individually as a special case, where the discrete formulation of irreversible thermodynamics as suggested and developed by Ogurtani (2000), may be a very powerful tool to handle this problem successfully, as it will be shown in the next section.

After these mentioned drop outs, the following formula obtained for the IEP

$$\frac{d}{dt} S_{IEP} = \frac{\Omega_\sigma}{T} \lim_{\varepsilon \rightarrow 0} \left\{ \int_{+\varepsilon}^{-\varepsilon} d\ell \left[J_\sigma \frac{\partial}{\partial \ell} (\tilde{g}_{\beta b} + g_\sigma \kappa) \right] + \int_{+\varepsilon}^{-\varepsilon} d\ell \left[(\tilde{g}_{\beta b} + g_\sigma \kappa) \hat{J}_{b\beta} \right] \right\} \quad (2.3.32)$$

Before proceeding further, let us turn back to postulates of irreversible thermodynamics: As shown by Prigogine (1961), the internal entropy production of the irreversible processes can be written as a sum of the products of generalized forces or affinities and the corresponding rates or generalized fluxes,

$$\frac{d}{dt} S_{IEP} = \sum_k J_k F_k \geq 0 \quad (2.3.33)$$

By utilizing this postulate, which means by comparing the Eqs. (2.3.32 and 2.3.33), one obtains the following forces from the integrated IEP expression (2.3.32), which is valid for any arbitrary closed loop.

$$F_\sigma = \frac{\Omega_\sigma}{T} \frac{\partial}{\partial \ell} (\tilde{g}_{\beta b} + g_\sigma \kappa) \quad (2.3.34)$$

and

$$F_{\beta b} = \frac{\Omega_\sigma}{T} (\check{g}_{\beta b} + g_\sigma \kappa) \quad (2.3.35)$$

where, F_σ and $F_{\beta b}$ denote longitudinal and transverse generalized forces that are acting on the interfacial layer respectively.

If one considers the additional contributions due to external forces, denoted by \vec{F}_{ext} ,

$$F_\sigma = \Omega_\sigma \left[\frac{1}{T} \frac{\partial}{\partial \ell} (\check{g}_{\beta b} + g_\sigma \kappa) + \vec{t} \cdot \vec{F}_{ext} \right] \quad (2.3.36)$$

and

$$F_{\beta b} = \Omega_\sigma \left[\frac{1}{T} (\check{g}_{\beta b} + g_\sigma \kappa) + \vec{n} \cdot \vec{F}_{ext} \right] \quad (2.3.37)$$

Here \vec{t} and \vec{n} denote unit tangent and normal vectors at the surface. The external forces were discussed by Ogurtani and Oren (2001-a) in Appendix B of that reference for various kind of external forces, such as electrostatic, and magnetic in nature.

Here only the electrostatic external forces will be discussed. The external generalized forces per particle, i , associated with electromigration is given by,

$$\vec{F}_{em}^i = -\frac{eZ^i}{T} \nabla \mathcal{G} \quad (2.3.38)$$

Where, \mathcal{G} is the electrostatic potential and eZ^i is the effective charge of the particle i . The external generalized total force density (per unit volume) associated with electromigration and acting on particles may have the following form for a multi-component system whether it is a bulk phase or an interfacial layer,

$$\vec{F}_{ext} = \vec{F}_{em} = -\frac{1}{T\Omega_\sigma} \left(\sum_i x^i eZ^i \right) \nabla \mathcal{G} = -\frac{1}{T\Omega_\sigma} eZ^* \nabla \mathcal{G} \quad (2.3.39)$$

where, eZ^* is the effective charge in multi-component systems.

The last contribution in Eq. (2.3.37), $\vec{n} \cdot \vec{F}_{ext}$, becomes identically zero since the normal component of the electric field intensity vanish at the surface.

Then, according to the Onsager theory (de Groot, 1951 and Prigogine 1961), which connects generalized forces and conjugate fluxes through generalized mobilities, the conjugate fluxes associated with the above forces can immediately be written down, by neglecting the cross-coupling terms between generalized forces and fluxes, as:

$$J_\sigma = \frac{M_\sigma}{kT} \Omega_\sigma \frac{\partial}{\partial \ell} \left[\left(\tilde{g}_{\beta\beta} + g_\sigma \kappa \right) - \langle eZ^* \rangle \frac{\mathcal{G}}{\Omega_\sigma} \right] \quad (\text{Surface Flux}) \quad (2.3.40)$$

and

$$\hat{J}_{\beta\beta} = \frac{M_{\beta\beta}}{kT} \Omega_\sigma \left(\tilde{g}_{\beta\beta} + g_\sigma \kappa \right) \quad (\text{Incoming net lateral flux density}) \quad (2.3.41)$$

where, M_σ/k and $M_{\rho b}/k$ are the generalized phenomenological mobilities associated with the respective conjugated forces and fluxes, $\langle eZ^* \rangle$ is the mean value of the effective electromigration charge associated with the interacting species and k is the Boltzman's constant.

For multi-component systems, where one is interested only in the net atomic (mass) transport regardless to the contributions of individual chemical species, the first generalized-mobility, M_σ , may not be easily connected to any combination of the intrinsic surface diffusivities of individual chemical species in the interfacial layer or in the bulk phase. However, for one component system having minor amount of doping elements or impurities, the situation is rather simple where one can easily identify the existence of the following relationship between generalized mobility and the surface self-diffusivity of host matter denoted by \tilde{D}_σ ,

$$\hat{M}_\sigma = \frac{M_\sigma}{kT} = \frac{\tilde{D}_\sigma}{kT} \frac{h_\sigma}{\Omega_\sigma} = \frac{\tilde{D}_\sigma}{kT} \Gamma_\sigma, \quad (2.3.42)$$

Hence, for the future discussions, the following compact form will be used, which is more suitable to take other driving forces such as the electromigration drift motion of surface atoms into considerations:

$$J_\sigma = \hat{M}_\sigma \frac{\partial}{\partial \ell} \left[\Omega_\sigma (\tilde{g}_{\rho b} + g_\sigma \kappa) - \langle eZ^* \rangle \mathcal{G} \right] \text{ (Surface Flux)} \quad (2.3.43)$$

Where \hat{M}_σ may be called surface atomic mobility, and it has the dimension given by $(erg.sec)^{-1}$.

The generalized mobility, $M_{\beta b}$ (cm^2/sec), associated with the incoming bulk diffusion flux is related to the transformation rate of chemical species from bulk phase to the interfacial layer or vice versa over the activation energy barrier denoted by $\Delta G_{\beta b}^*$. Hence, it can be defined according to the transition rate theory of chemical kinetics advocated by Eyring (Yeremin, 1979), as:

$$M_{\beta b} = \frac{kT}{h} \exp\left(-\frac{\Delta G_{\beta b}^*}{kT}\right) \quad (2.3.44)$$

In the future formula one will use rather normalized mobility, which may be defined by $\hat{M}_{\beta b} = M_{\beta b} / kT$, which has the following dimension $cm^2 (erg.sec)^{-1}$.

2.4. Mathematical Model for the Evolution Dynamics of the Surface of interconnect

The present model developed in this chapter considers not only the drift-diffusion of chemical species on the realistic surface but also the direct transfer of chemical species between bulk phase and the second phase through the interfacial layer as a dominant transport mechanisms.

The time and the scale variables t and ℓ are normalized in the following manner, first of all an atomic mobility associated with the mass flow at the surface layer is defined as it has been already done in section 2.3.1 by the Eq. (2.3.42). And then a new time scale is introduced by;

$$\tau_o = \frac{r_o^4}{\Omega_\sigma^2 \hat{M}_\sigma g_\sigma} \quad (2.4.1)$$

where r_o is the mean initial radius of void or hillock which can be obtained directly from $r_o = \sqrt{A_o / \pi}$, using the fact that the initial cross sectional area is A_o . Similarly r_o is used as a length scale. In the following formulas the bars over the symbols indicates the normalized and scaled quantities.

The curvilinear coordinate along the surface (arc length), ℓ , the interconnect with w , and the local curvature, κ , that represents the capillary effect are normalized with respect to length scale and the system time, t , is normalized with respect to time scale as shown below:

$$\bar{\ell} = \ell / r_o, \quad \bar{w} = w / r_o, \quad \bar{\kappa} = \kappa r_o \quad \text{and} \quad \bar{t} = t / \tau_o, \quad (2.4.2)$$

The volumetric Gibbs free energy difference between the bulk phase and the second phase can be normalized by using the specific Gibbs free energy of the interfacial layer, denoted by g_σ ,

$$\bar{g}_{\beta b} = \frac{\tilde{g}_{\beta b} r_o}{g_\sigma} \quad (2.4.3)$$

The electrostatic potential generated at the surface may be normalized with respect to the remote applied electric field denoted by E_0 and it is given by

$$\bar{g} = \frac{\mathcal{G}}{E_0 r_o} \quad (2.4.4)$$

The relative importance of electromigration with respect to capillary forces can be easily represented by a single variable, χ , and that may be called as the *electron wind intensity*, as it will be shown later this is a very important experimental parameter in the simulations.

$$\chi = \frac{e|\hat{Z}|E_0 r_o^2}{\Omega_\sigma g_\sigma} \quad (2.4.5)$$

and similarly one may normalize the generalized mobility $\hat{M}_{\beta b}$ associated with the interfacial displacement reaction taking place during the growth process, with respect to the mobility of the surface diffusion denoted by \hat{M}_σ ,

$$\bar{M}_{\beta b} = \frac{\hat{M}_{\beta b} r_o^2}{\hat{M}_\sigma} \quad (2.4.6)$$

After these normalizations, the normal displacement velocity for the ordinary points can be obtained by using the surface flux, given by Eq. (2.3.40), and the incoming net lateral flux density, given by Eq. (2.3.41):

$$\bar{v}_{ord} = \frac{\partial}{\partial \ell} \left[D''(\vartheta, \theta) \frac{\partial}{\partial \ell} (\bar{g}_{\beta b} + \chi \bar{\vartheta} + \bar{\kappa}) \right] - \bar{M}_{\beta b} (\bar{g}_{\beta b} + \bar{\kappa}) \quad (2.4.7)$$

Where, the angular dependent post factor $D''(\vartheta, \theta)$ denotes that the surface drift-diffusion is anisotropic.

The first group of terms in above partial differential equation (2.4.7) represents a rather conventional approach and closely related to the mass accumulation due to surface diffusion along the void interfacial layer. The second group of terms is due to the mass flow associated with the chemical species transfer between bulk phase and the second phase having curved advancing boundary as a reaction front. This additional contribution to the void displacement process is a natural and rigorous out come of the novel application of the irreversible thermodynamics by Ogurtani (2000) to the curved interfaces using a rather realistic concept of surface phases with finite extent as originally proposed by Guggenheim (1959) and Van Der Waals and Baker (1928), rather than the hypothetical Gibbs (1948) description.

CHAPTER 3

MATHEMATICAL MODEL & NUMERICAL PROCEDURES

3.1. Introduction

After the normalization procedures, the normal displacement velocity for the ordinary points was obtained as

$$\bar{v}_{ord} = \frac{\partial}{\partial \ell} \left[D''(\mathcal{G}, \theta) \frac{\partial}{\partial \ell} (\bar{g}_{\beta b} + \chi \bar{g} + \bar{\kappa}) \right] - \bar{M}_{\beta b} (\bar{g}_{\beta b} + \bar{\kappa}) \quad (3.1.1)$$

According to the extensive experimental studies performed by Blech (1976) and his coworkers (Kinsbron *et al.* 1977), at the end of the incubation period the steady state concentration profile established in the sample and over-all drift-diffusion phenomenon is controlled by the interface transfer reactions at the cathode and the anode ends. These observations give very strong indication that the vacancy

concentration stays invariant at the advancing surface layer. Therefore, under any circumstances for gross computer simulations, it is a reasonable approximation to assume that the normalized Gibbs free energy of interfacial reaction stays constant of time and space (isotropic), namely $\nabla \bar{g}_{\beta b} = 0$. Then Eq. (3.1.1) becomes,

$$\bar{v}_{ord} = \bar{n} \cdot \frac{\partial \bar{r}}{\partial \bar{t}} = \frac{\partial}{\partial \bar{\ell}} \left[D''(\vartheta, \theta) \frac{\partial}{\partial \bar{\ell}} (\chi \bar{g} + \bar{\kappa}) \right] - \bar{M}_{\beta b} (\bar{g}_{\beta b} + \bar{\kappa}) \quad (3.1.2)$$

In the present model, a constant electric field E_o is imposed far away from the surface, which generates an electrical field denoted by E , having zero normal components at the second phase – interconnect interfacial layer. In this model it is also assumed that the vacancy concentration is kept constant at the upper and lower boundaries of interconnect.

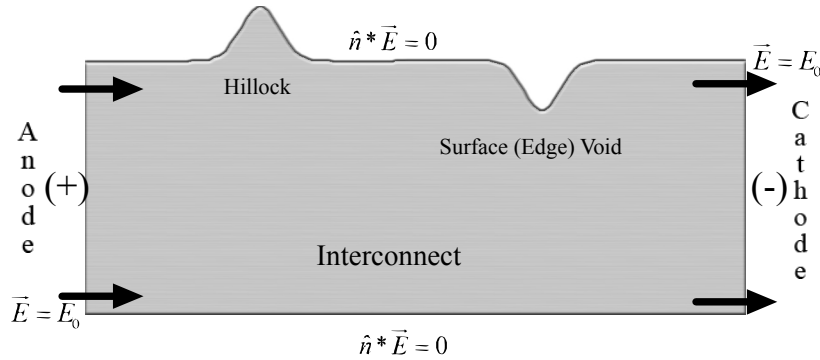


Figure 3.1.1: The schematic representation of the hillock and edge void together.

3.2. Numerical Methods

In the following subsections the numerical methods are discussed as in the order as the computer program, which is a *C++ code*.

i. Initial System

At the initial state, system composed of the interconnect surface which is simulated by a finite number of nodes using predetermined segment lengths. The positions of the nodes are defined by reference to the cartesian coordinates and represented by

the three dimensional vectors, described as $\vec{r}^{(i)} = \begin{pmatrix} x \\ y \\ 0 \end{pmatrix}$, for taking the advantage of

vector algebra.

After knowing the node position vectors, it is straight forward to calculate the segment lengths, s , and the centroid position vectors, \vec{r}_c , such as:

$$s_i = \left| \Delta \vec{r}^{(i)} \right| \quad \text{where} \quad \Delta \vec{r}^{(i)} = \vec{r}^{(i+1)} - \vec{r}^{(i)} \quad (3.2.1)$$

and

$$\vec{r}_c^{(i)} = \frac{\vec{r}^{(i+1)} + \vec{r}^{(i)}}{2} \quad (3.2.2)$$

ii. Calculation of the Turning Angles at the Nodes

The turning angles at the nodes are calculated by using the definitions of the vector and the dot products of the two vectors and the figure 3.2.2.

$$\theta_i = \left\{ \begin{array}{ll} \arcsin \left(\frac{\Delta \vec{r}^{(i-1)} \times \Delta \vec{r}^{(i)}}{|\Delta \vec{r}^{(i-1)}| |\Delta \vec{r}^{(i)}|} \right) & \text{if } \Delta \vec{r}^{(i-1)} \cdot \Delta \vec{r}^{(i)} \geq 0 \\ \pi - \arcsin \left(\frac{\Delta \vec{r}^{(i-1)} \times \Delta \vec{r}^{(i)}}{|\Delta \vec{r}^{(i-1)}| |\Delta \vec{r}^{(i)}|} \right) & \text{otherwise} \end{array} \right. \quad (3.2.3)$$

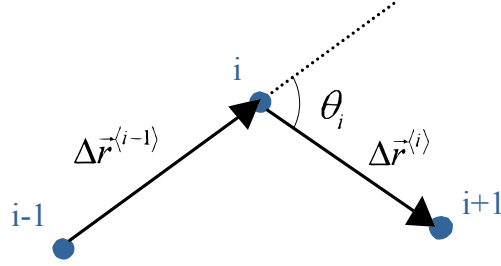


Figure 3.2.1: The segment turning angle, θ_i , at the node i .

iii. Calculation of Node Curvatures

The curvatures at the nodes can be evaluated at each node by using a discrete geometric relationship in connection with the fundamental definition of radius of curvature and the normal vector.

Let us define some geometric relationships; first of all the curvature of a circle with radius ρ_i (radius of curvature) is $1/\rho_i$ and furthermore three points in the plane define a unique circle whose circumference pass from all of these three points. Figure 3.2.2 shows such a circle that passes from the three successive surface nodes $i-1$, i , at which the local curvature is wanted to calculate, and $i+1$ by using the known values of the segment lengths, s_i , and the segment turning angle θ_i .

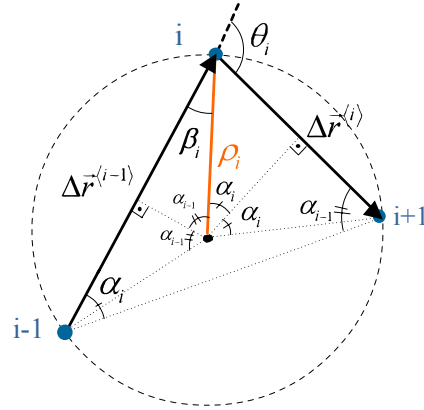


Figure 3.2.2: The unique circle that pass from the three successive void nodes.

From figure 3.2.2 one can immediately write down the following identities.

$$\rho_i = \frac{s_i}{2 \sin(\alpha_i)} \quad (3.2.4)$$

and

$$\kappa_i = \frac{1}{\rho_i} = \frac{2 \sin(\alpha_i)}{s_i} \quad (3.2.5)$$

The tangent of the angle α_i can be formulated as follows:

$$\tan(\alpha_i) = \frac{\sin(\theta_i)}{\frac{s_{i-1}}{s_i} + \cos(\theta_i)} \quad (3.2.6)$$

Using the Eq. (3.2.5) and (3.2.6), the local curvature is given by

$$\kappa_i = \frac{2 \sin \left(\operatorname{atan} \left(\frac{\sin(\theta_i)}{\frac{s_{i-1}}{s_i} + \cos(\theta_i)} \right) \right)}{s_i} \quad (3.2.7)$$

iv. Calculation of the Local Line Normal Vectors

In order to calculate the normal vectors at the nodes, one can easily write that $\beta_i = (\pi/2) - \alpha_{i-1}$. Then first multiply $\Delta\vec{r}^{(i-1)}$, which is the vector that connects the successive nodes by the clockwise rotation matrix in order to obtain a vector along the local line normal vector as shown below,

$$\vec{n}^{(i)} = \begin{vmatrix} \cos(-\beta_i) & -\sin(-\beta_i) & 0 \\ \sin(-\beta_i) & \cos(-\beta_i) & 0 \\ 0 & 0 & 1 \end{vmatrix} \cdot \Delta\vec{r}^{(i-1)} \quad (3.2.8)$$

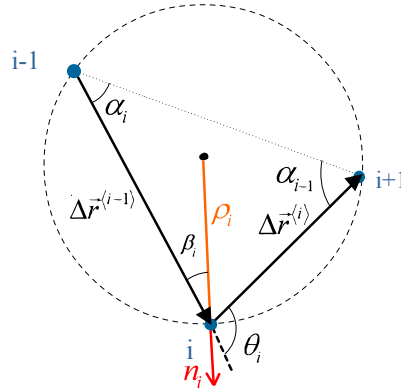


Figure 3.2.3: The unique circle that pass from the three successive void nodes.

After that it is straightforward to calculate the local line normal vector namely,

$$\hat{n}^{(i)} = \vec{n}^{(i)} / |\vec{n}^{(i)}|.$$

v. Calculation of the Electrostatic Potentials by using the Indirect Boundary Element Method solution of the Laplace's Equation

At this point before proceeding further, a brief description of the indirect boundary element method (IBEM) is given, and then by using this method the electrostatic potentials at the surface is calculated.

An initial restriction of the BEM was that the fundamental solution (FS) to the original partial differential equation was required in order to obtain an equivalent boundary integral equation.

In IBEM the solution is again obtained by the superposition of FS's but instead of the sources being located at a finite number of points outside the domain they are distributed continuously over its boundary. The intensity of the distribution is usually known as the density function (DF). The partial differential equation is automatically satisfied at every interior point of the domain, and the only thing that is required is to satisfy the boundary conditions by the suitable choice of the DF. Once the DF has been solved, physically meaningful results at boundary and interior points of the domain are computed by integration over the boundary.

In this problem one is seeking the solution of a Laplace equation in a two dimensional domain that is given by the following equation

$$\nabla^2 g(r) = 0 \tag{3.2.9}$$

With the following boundary conditions, namely Neumann boundary conditions,

$$\hat{n} \cdot \nabla \mathcal{G}(r) = \hat{n} \cdot \frac{\partial \mathcal{G}(r)}{\partial r} \hat{r} = 0 \quad (3.2.10)$$

Where the scalar function $\mathcal{G}(r)$ is the electrostatic potential at the boundaries.

For a two dimensional problem, the source is assumed to be distributed along a line of infinite length from $z = -\infty$ to $z = \infty$ and the fundamental solution $U(P, Q)$, which satisfies the Laplace equation and represents the field generated by a concentrated unit charge at P (*source point*) acting at a point Q (*field or observation point*), is given by (Paris and Canas, 1997):

$$U(P, Q) = \frac{1}{2\pi} \ln \frac{1}{r} \quad (3.2.11)$$

where r is the distance from source point to field point.

By using the FS, given in Eq. (3.2.11), the directional derivative of the FS, which satisfy Laplace equation, can be obtained as,

$$\begin{aligned}
T(P,Q) &= \hat{n} \cdot \nabla U(P,Q) = \hat{n} \cdot \frac{\partial U(P,Q)}{\partial r} \hat{r} = \hat{n} \cdot \frac{\partial U(P,Q)}{\partial r} \frac{\vec{r}}{|\vec{r}|} \\
&= -\frac{1}{2\pi|\vec{r}|} \hat{n} \cdot \frac{\vec{r}}{|\vec{r}|} = -\frac{1}{2\pi} \frac{|\hat{n}||\vec{r}|\cos(\theta)}{|\vec{r}|^2} \\
&= -\frac{1}{2\pi} \frac{\cos(\theta)}{|\vec{r}|}
\end{aligned} \tag{3.2.12}$$

Where θ is the angle between the line QP and the outward normal \hat{n} as shown in figure 3.2.4. Figure 3.2.5 shows the variation of the directional derivative of FS where the flow is in the x direction.

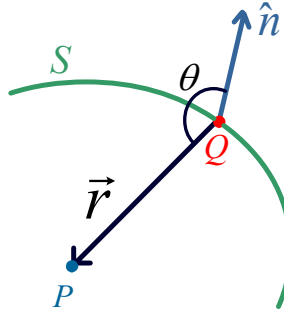


Figure 3.2.4: Notation for the FS of Laplace Equation.

In the IBEM, one seeks a solution in the form of

$$u(Q) = \int_S U(P,Q) \mu(P) dS_P \tag{3.2.13}$$

Where the density function $\mu(P)$ is the intensity of sources, which are continuously distributed over the boundary S of the domain. In two-dimensional problems, dS means with respect to arc length. The subscript P means that in the integration the point moves over the boundary whilst the point Q stays still. Since $U(P,Q)$

satisfies the governing partial differential equation everywhere except at P , $u(Q)$ as defined by Eq. (3.2.13) satisfies the differential equation at all interior points of the domain, but not on its surface S . Eq. (3.2.13) is referred to as the integral representation.

At this point the only thing that must be satisfied is the boundary conditions. When considering how to do this, it should be borne in mind that the solution must satisfy the governing partial differential equation at all points inside the domain and also on the surface S . The integral representation does not do this, and it follows that for the Neumann boundary conditions it is necessary to equate the limiting values as Q on S is approached from inside the domain of $u(Q)$ and $\hat{n} \cdot \nabla u(Q)$ as defined by Eq. (3.2.13) to the given boundary data.

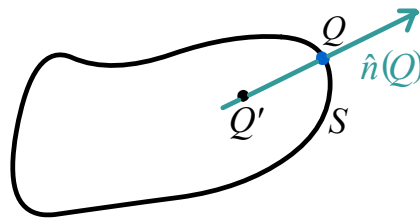


Figure 3.2.5: Satisfaction of boundary condition in the IBEM

For the Neumann condition, one must set the limiting value as Q' approaches Q (Figure 3.2.5) of the derivative in the direction $n(Q)$ of $u(Q')$ as defined by Eq. (3.2.13) to its given value $\bar{t}(Q)$. The function $U(P, Q')$ is bounded and so it is permissible to differentiate under the integral sign:

$$\begin{aligned}
\hat{n} \cdot \nabla u(Q) &= \int_S \hat{n} \cdot U(P, Q) \mu(P) dS_P \\
&= \int_S T(P, Q) \mu(P) dS_P
\end{aligned}
\tag{3.2.14}$$

Where $T(P, Q')$ is given by Eq. (3.2.12)

One may now write

$$\lim_{Q' \rightarrow Q} \frac{\partial u}{\partial n}(Q') = \bar{t}(Q)
\tag{3.2.15}$$

To illustrate the behavior of the function $\partial u / \partial n(Q')$ as Q' approaches and passes through S at Q let us take Q to be on a straight part of the boundary of a two-dimensional domain, and let us suppose that over this straight part of the boundary $\mu(P)$ is constant and therefore equal to $\mu(Q)$. $S(Q, n)$ denotes the straight part AB of the boundary as shown in figure 3.2.8, where ε denotes the distance QQ' .

$$\frac{\partial u}{\partial n}(Q') = I_1(Q') + I_2(Q')
\tag{3.2.16}$$

where

$$I_1(Q') = \int_{S(Q, n)} T(P, Q') \mu(P) dS_P
\tag{3.2.17}$$

and

$$I_2(Q') = \int_{S-S(Q,n)} T(P, Q') \mu(P) dS_P \quad (3.2.18)$$

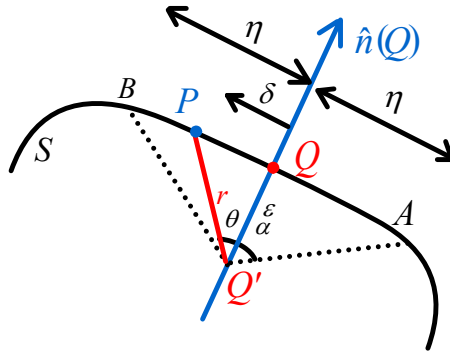


Figure 3.2.6: Limit of integral over AB as Q' approaches Q

The function $I_2(Q')$ varies continuously as Q' approaches and passes through S .

When Q' is inside the domain as shown in figure 3.2.6,

$$I_1(Q') = \int_{-n}^n \frac{\cos \theta}{2\pi r} \mu(P) ds = \mu(Q) \int_{-\alpha}^{\alpha} \frac{1}{2\pi r} d\theta \quad (3.2.19)$$

where $\alpha = \tan^{-1} \frac{n}{\epsilon}$. By integrating and substituting limits one finds that

$$I_1(Q') = \mu(Q) \frac{\alpha}{\pi} \quad (3.2.20)$$

and so since α tends to $\pi/2$ as Q' approaches Q ,

$$\lim_{Q' \rightarrow Q} I_1(Q') = \frac{1}{2} \mu(Q) \quad (3.2.21)$$

When Q' is at Q , $T(P, Q') = 0$ for all P in $S(Q, n)$, and so $I_1(Q) = 0$. Therefore,

$$\lim_{Q' \rightarrow Q} \frac{\partial u}{\partial n}(Q') = \int_S T(P, Q) \mu(P) dS_P + \frac{1}{2} \mu(Q) \quad (3.2.22)$$

Substituting this result into Eq.3.2.15 gives

$$\frac{1}{2} \mu(Q) + \int_S T(P, Q) \mu(P) dS_P = \bar{t}(Q) \quad (3.2.23)$$

which is the integral equation for the Neumann boundary condition.

For the purpose of numerical analysis there is a significant restriction that is the point Q can not be located at an edge or corner, or at any point at which $\bar{t}(Q)$ is discontinuous. Edges and discontinuous $\bar{t}(Q)$ occur frequently in engineering analysis. As the point P on S approaches Q , for two-dimensional case it remains bounded. It should be borne in mind however that in the analysis leading to this conclusion it is supposed that $\mu(Q)$ is bounded and indeed continuous, whereas analogy with the distribution of electrical charge over a conducting surface suggest that edges, corners and discontinuities of $\bar{t}(Q)$. The generality of the method may therefore be greater than that suggested by existing mathematical analysis.

In the simplest implementation of the IBEM of solution of Laplace's equation, the boundary S is represented by straight-line elements in two dimensions, and it is supposed that over each of these elements $\mu(Q)$ is constant. Simultaneous equations for the value of $\mu(Q)$ are obtained by taking point Q in Eq. (3.2.13) to be located at the centroid of each of these elements in turn. Let there be N elements S_1, S_2, \dots, S_N , then for the present problem, the simultaneous equations are

$$\frac{1}{2}\mu(Q_i) + \sum_{j=1}^N \Delta T_{ij} \mu(Q_j) = \bar{t} \mu(Q_i), \quad i = 1, 2, \dots, N \quad (3.2.24)$$

where

$$\Delta T_{ij} = \int_{S_j} T(P_j, Q_i) dS_{p_j} \quad (3.2.25)$$

Since in Eq. (3.2.24) the point Q_i is at the centroid of an element, the surface smoothness condition for validity of that equation is always satisfied.

For a finite domain, the matrix of equation coefficients is singular in the limit as the number of elements tends to infinity and it is necessary for example to take $u(Q)$ to be zero at one of the elemental centroids; Eq. (3.2.24) is then written at that centroid and at all the others. For an infinite domain, the integral representation can model at infinity $u(Q) = \ln \frac{1}{r_o} \int_S \mu(P) dS_p$ where r_o is distance from an arbitrary chosen

reference point in two dimensions, but not a non-zero constant value. Therefore, the

solution of the Neumann boundary value problem, and the matrix of equation coefficients are not singular in the limit as the number of elements tends to infinity.

It is possible to evaluate analytically the integral ΔT_{ij} : note that since the elements are straight, $T(P_i, Q_i) = 0$ everywhere on the element S_i and so in Eq. (3.2.14), $\Delta T_{ii} = 0$ and leading diagonal coefficients all equal $\frac{1}{2}$. The matrix coefficients of Eq. (3.2.24) are dimensionless in the sense that they have the same numerical values regardless of the choice of the unit of distance.

Here let us turn back to the problem at which the direction of the applied electric field is in the positive x direction.

Now let us seek a solution as the sum of two parts, these being the electrostatic potential due to applied electric field that would exist if the void were not there, and a perturbation of that solution chosen so that the sum of the two parts satisfies the boundary conditions.

$$\mathcal{G}(r) = \mathcal{G}^I(r) + \mathcal{G}^{II}(r) \quad (3.2.26)$$

The boundary condition given by Eq. (3.2.10) indicates that the electric field at the boundary along the boundary normal direction is zero.

$$\begin{aligned} E(Q) &= -\text{grad}(\mathcal{G}(Q)) \\ &= -\text{grad}(\mathcal{G}^I(Q)) - \text{grad}(\mathcal{G}^{II}(Q)) = E^I(Q) + E^{II}(Q) = 0 \end{aligned} \quad (3.2.27)$$

For the present problem; if there is no void inside the interconnect the electrostatic potential that corresponds the electrostatic applied voltage along the negative x direction according to the coordinate system shown in figure 3.2.9, is given by

$$\mathcal{G}^I(Q) = -E_o x = -E_o \vec{r} \cdot \begin{pmatrix} 1 \\ 0 \\ 0 \end{pmatrix} = -E_o r \cos(\phi) \quad (3.2.28)$$

From the solution in Eq. (3.2.27), the normal component of the electric field on the boundaries may be calculated as

$$E^I(Q) = -grad(\mathcal{G}^I(Q)) = -\hat{n} \cdot \nabla \mathcal{G}^I(Q) = -E_o \cos(\phi) \quad (3.2.29)$$

By comparing the Neumann boundary conditions given in Eq. (3.2.27) and the Eq. (3.2.29) it is found that the normal component of the electric field due to the fictitious charges distributed along the boundaries have to be given by

$$E^{II}(Q) = -E^I(Q) = E_o \cos(\phi) \quad (3.2.30)$$

Now the problem is to adjust the magnitude of the fictitious charges, denoted by μ_i , such that to satisfy the Eq. (3.2.30) in order to satisfy the boundary conditions. Noting that the normal derivative of the FS is $T(P,Q)$, the boundary condition at the point Q_i can be satisfied by using the Eq. (3.2.24).

$$\frac{1}{2} \mu(Q_i) + \sum_{j=1}^N \Delta T_{ij} \mu(Q_j) = E^I(Q_i), \quad (3.2.31)$$

where N is the number of charges and $\Delta T_{ij} = \Delta T(P_i, Q_j)$. After finding the charge distribution that satisfy the boundary conditions the $g^{II}(Q)$ can be calculated as

$$g^{II}(Q_i) = \sum_{j=1}^N \Delta U_{ij} \mu(Q_j), \quad (3.2.32)$$

where $\Delta U_{ij} = \Delta U(P_i, Q_j)$ and it may be calculated by using the following integral

$$\Delta U_{ij} = \int_{S_j} U(P_j, Q_i) dS_{p_j} \quad (3.2.33)$$

These integrals can be calculated numerically by using the trapezoidal rule. By assuming that the charge density function at a given segment distributed uniformly.

Then one obtains the following system of simultaneous equations, which can be solved for the unknown fictitious charges μ_i .

$$\Delta T_{i,j} \cdot \mu_i = E_i^I \quad (3.2.34)$$

The nodes described in this problem contain three different set at each of which the centroids are continuous. These are the upper interconnect edge, the lower

interconnect edge and the void circumference, whose number of centroids are denoted by n_u , n_l and n_v , respectively. Then the connectivity matrix is given in the figure 3.2.7, where if inner void enter the grain $mm = n_u + n_l + n_v$, otherwise $mm = n_u + n_l$.

$$\underbrace{\begin{bmatrix} 0.5 & \Delta T_{0,1} & \cdot & \cdot & & \cdot & \cdot & \Delta T_{0,mm} \\ \Delta T_{1,0} & 0.5 & & & & & & \cdot \\ \cdot & & 0.5 & & & & & \cdot \\ & & & 0.5 & & & & \\ & & & & 0.5 & & & \\ & & & & & 0.5 & & \\ \cdot & & & & & & 0.5 & \cdot \\ \cdot & & & & & & & \Delta T_{mm-1,mm} \\ \Delta T_{mm,0} & \cdot & \cdot & & \cdot & \cdot & \Delta T_{mm,mm-1} & 0.5 \end{bmatrix}}_{\Delta T} \underbrace{\begin{bmatrix} \mu_0 \\ \cdot \\ \cdot \\ \cdot \\ \cdot \\ \cdot \\ \cdot \\ \mu_{mm} \end{bmatrix}}_{\mu} = \underbrace{\begin{bmatrix} E_0^I \\ \cdot \\ \cdot \\ \cdot \\ \cdot \\ \cdot \\ \cdot \\ E_{mm}^I \end{bmatrix}}_{EI}$$

Figure 3.2.7: The connectivity matrix

For the solution of above linear system, Gaussian elimination with back substitution method is performed. Also in this method a pivoting strategy is applied for the error reduction.

vi. Anisotropic Surface Diffusivity

The anisotropic diffusivity of surface atoms is incorporated into the numerical procedure by adapting the following relationship,

$$\tilde{D}_\sigma(\theta, \phi) = D_\sigma^0 \left\{ 1 + A \cos^2 [m(\theta - \phi)] \right\} \quad (3.2.35)$$

where D_{σ}^0 is the minimum surface diffusivity corresponding to a specific surface orientation, θ is the angle formed by the local tangent to the surface and the direction of the applied electric field. A , m , and ϕ are dimensionless parameters that determine the strength of the anisotropy, the grain symmetry through the number of crystallographic directions that corresponds to fast diffusion paths, and the orientation of the symmetry direction with respect to the direction of the applied electric field E_o , respectively. For brevity this angular dependent part of the diffusivity in above equations is denoted by $D''(\vartheta, \theta)$. Where $N = 2m$ corresponds to the rotational degree of symmetry or fold-number.

The following figures are obtained by using Eq. (3.2.35), in which the minimum surface diffusivity is taken as unity namely $D_{\sigma}^0 = 1$.

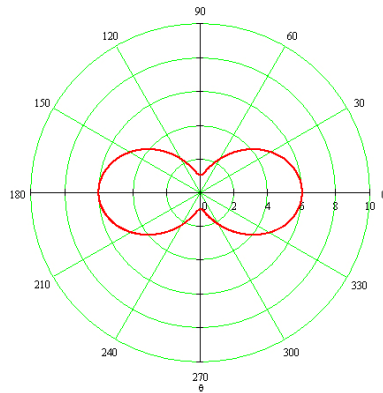


Figure 3.2.8: Diffusion Anisotropy,

$$D_{\sigma}^0 = 1, A = 5, m = 1 \text{ and } \theta = 0$$

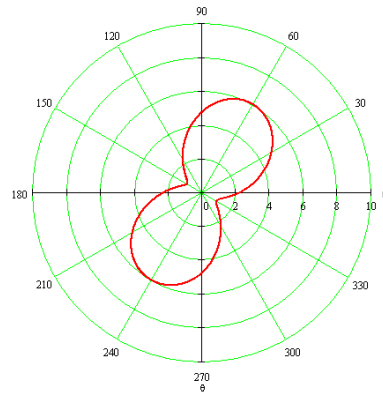


Figure 3.2.9: Diffusion Anisotropy,

$$D_{\sigma}^0 = 1, A = 5, m = 1 \text{ and } \theta = \pi/3$$

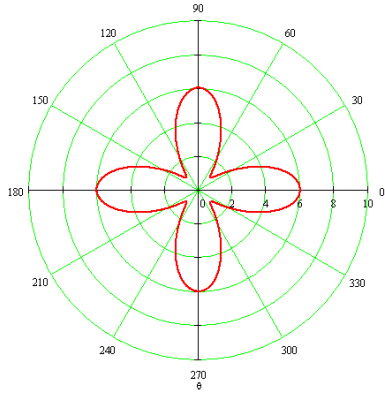


Figure 3.2.10: Diffusion Anisotropy,

$$D_{\sigma}^0 = 1, A = 5, m = 2 \text{ and } \theta = 0$$

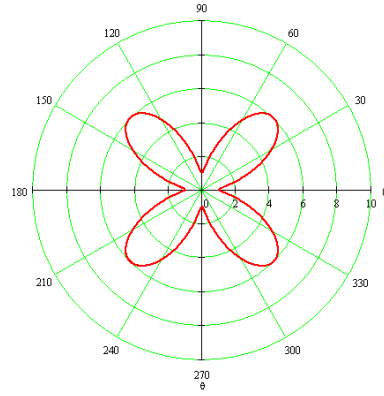
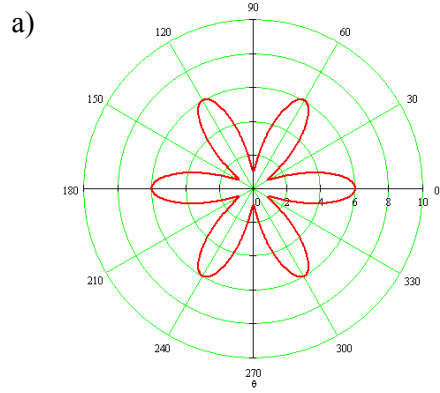


Figure 3.2.11: Diffusion Anisotropy,

$$D_{\sigma}^0 = 1, A = 5, m = 2 \text{ and } \theta = \pi/4$$



a) $D_{\sigma}^0 = 1, A = 10, m = 3 \text{ and } \theta = 0$

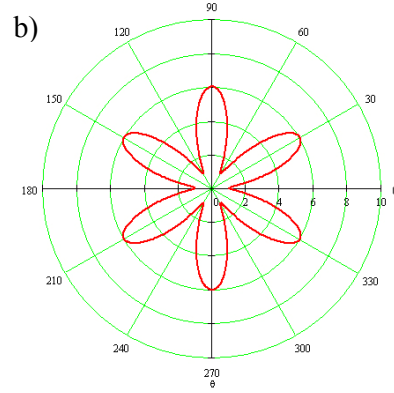


Figure 3.2.12: Diffusion Anisotropy,

b) $D_{\sigma}^0 = 1, A = 10, m = 3 \text{ and } \theta = \pi/6$

vii. Explicit Euler's Method

Explicit Euler's method (Mathews, 1992) is used to perform the time integration of Eq. (3.1.2) for the surface evolution. The time step is determined from the maximum surface velocity and minimum segment length such that the displacement increment is kept constant for all time step increments. This so-called adapted time step auto-control mechanism combined with the self-recovery effect associated with the capillary term guarantees the long time numerical stability and the accuracy of the explicit algorithm even after performing several hundred to several millions steps.

viii. Remeshing

In the present study the numerical methods require that the segment lengths must not be exceeded a critical value in order to keep the accuracy in an acceptable level. And also as the number of nodes increase the computation time is also increases. These two statements require that the segment lengths must be keep in a range between the minimum and the maximum segment lengths, $[s_{\min}, s_{\max}]$, in terms of a prescribed percentage of the mean distance.

If the distance between any two neighboring nodes becomes longer than s_{\max} , then the mid-point is converted into a node. Similarly, if the distance between any two

neighboring nodes becomes shorter than s_{\min} , then the further node is removed from the mesh and the new segment is formed.

ix. The Flowchart of the Program

After explaining the numerical methods used in the program, let us define the all program as a flowchart, which can be seen in Figure 3.2.13.

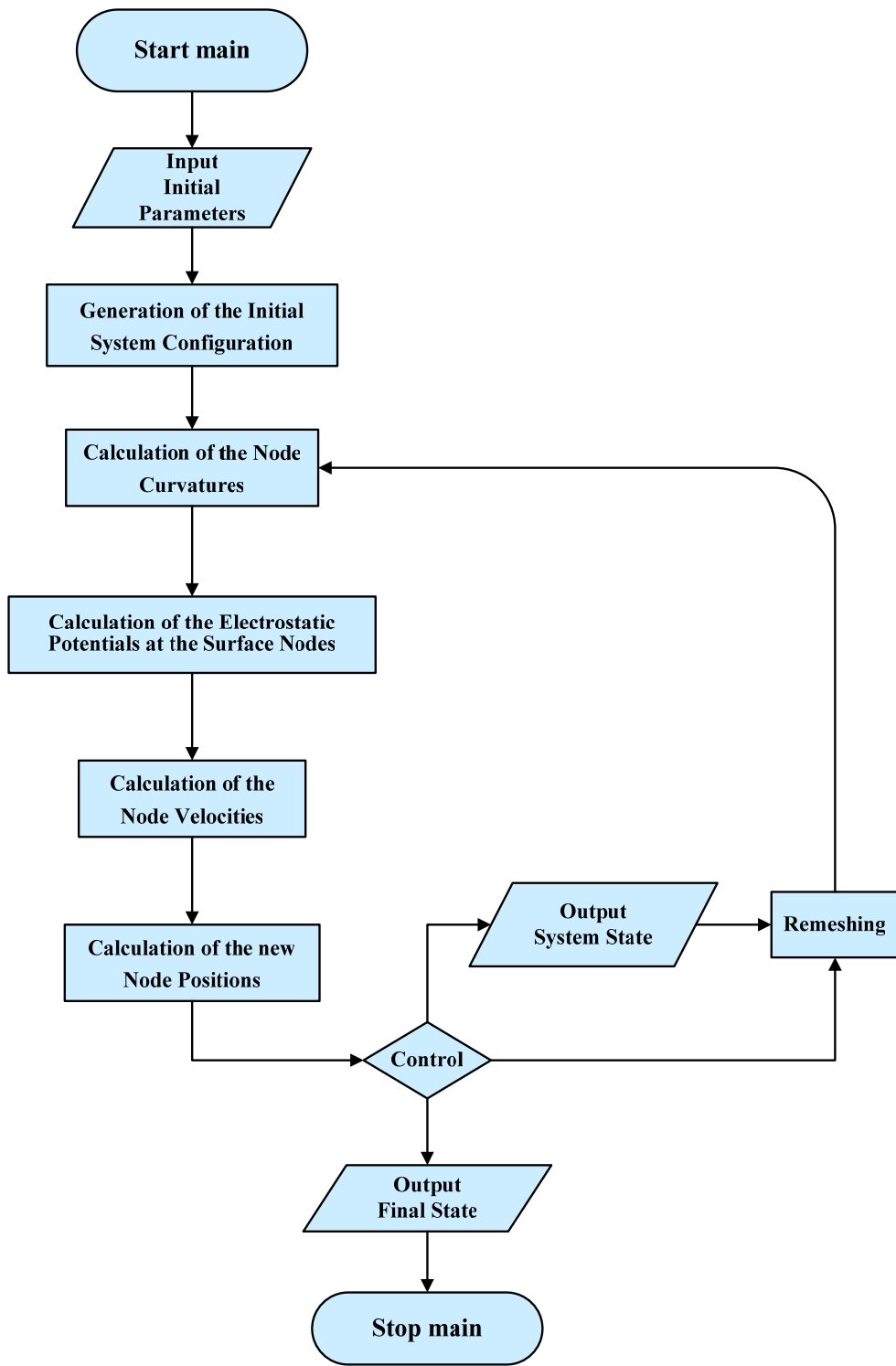


Figure 3.2.13: Program flow chart.

CHAPTER 4

RESULTS & DISCUSSION

In these simulation studies, the kinetics of voids and hillocks evolutions, on unpassivated and conducting metal single crystal lines, typical of modern sub-micron interconnects, made of thin metal strips attached to the substrates is investigated by computer simulations. The effect of the surface drift-diffusion anisotropy on the surface morphological variations under the action of the electromigration and capillary forces are fully explored, using variety of tilt angles and surface textures in face centered cubic crystals.

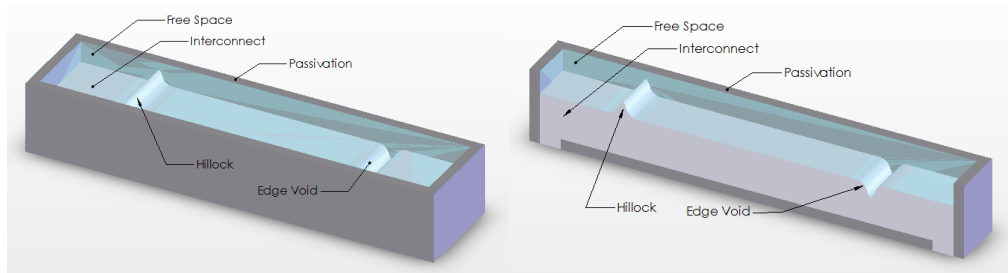


Figure 4.1: Experimental Setup that is simulated in this thesis.

The first time in the literature, the formation and the penetration of the electromigration (EM) induced voids into the bulk region, under variety of the surface textures and tilt angles are observed in the present simulated studies. Depending upon the tilt angle and the degree of symmetry, and finally the intensity

of the electron wind, these EM induced voids may have very different morphologies such as wedge, slit and almost spherical in shapes. The slit and wedge shapes EM voids after having short dragging times may reach the interface between interconnect and the substrate creating fatal circuit break down. The rounded EM voids which occurs mostly under the high electron wind intensities $\chi \geq 25$, show steady drift towards the cathode end without changing their shapes.

The edge void lying on the low symmetry surfaces having large tilt angles ($\theta=135$) with respect to the direction of the electron wind develops oscillatory undulations on the surface, which separates only along the windward but also along the leeward. In certain surface textures and electron wind combinations the edge void may be dispersed completely without leaving any trace on the surface.

In some case the edge Hillock may create a solitary wave moving steadily towards the anode end of the interconnect line. In certain combinations, a small piece of material may be detached from the Hillock, and taking almost perfect spherical shape moving towards the anode due to the shunt effect of the underlayer.

All together 192 different combinations of the surface textures, drift-diffusion anisotropy coefficients, and electron wind intensity parameters are subjected to this simulation work. We have employed four different electron wind intensity parameters, ($\chi = 5, 10, 25$ and 50), which covers from the moderate up to the high current densities ($j = 10^9 - 10^{12}$ A/m²) that are mostly utilized in normal and accelerated laboratory test studies. As an initial state for the surface topology, a

Gaussian shape void or hillock is introduced on top of the otherwise perfectly smooth plane surface. We have also adapted large aspect ratios, $\beta = 20$ with reference to the width of the void or hillock present at the surface, and utilized quasi-infinite boundary conditions such as that the surface curvature and their higher derivatives are all equal to zero at the anode and cathode edges. The constant and uniform electric field is applied to the specimen, which insures that there is steady flow of atomic species from the cathode end to the anode edge of the specimen. The induced electric field due to surface defects and internal voids are calculated by indirect boundary element method (IBEM), using modified Neumann boundary conditions, which leaves the cathode and anode edges completely open for the current flow, and closes the upper and lower surfaces, and avoids any current penetration to the internal voids. We also assumed that the lower surface is rigidly attached to the substrate, and system is complete free from internal stresses.

In subsequent sections we will present our findings very systematic fashion for the edge voids and the hillocks separately, and discuss their evolution kinetics in terms of electron wind intensity parameter and the surface texture morphologies. We will also introduce some analytical expression for the incubation times for the formation of EM voids and the decay relaxation time for hillock and edge voids. The dragging kinetics of EM voids is also examined limited extent, which doesn't permit to produce any analytical expression yet.

4.1. Surface Void Configuration:

The morphology of an initially perfectly flat surface having a perturbation in the shape of Gaussian edge-void is demonstrated in Fig. 4.1.1., where the positive direction of electric field is from the left (anode) to the right (cathode). The scaled interconnect width is denoted as \bar{w} and the void depth and the specimen length are given by \bar{a} and \bar{L} , respectively. These are all scaled with respect to the arbitrary length denoted by ℓ_o . Three different crystal planes in a FCC structure, $\{110\}$, $\{100\}$ and $\{111\}$ are considered, which may be characterized by two, four and six fold symmetry axes, respectively.

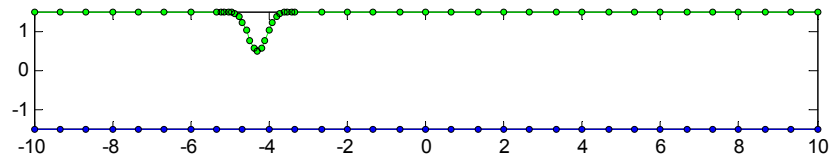


Figure 4.1.1: Initial System with edge void. $\bar{w} = 3$, $\bar{a} = 1$ and $\bar{L} = 20$.

i. Two Fold Crystal Symmetry, $\{110\}$ Planes in FCC:

The interconnect having two fold symmetry with zero degree tilt angle $\theta = 0$ with respect to the electric field direction tends to transform the Gaussian shape edge-void into the slit like shape stretched to the windward direction. Eventually, the tip of this slit type void breaks down and generates an internal void having various different in forms. The actual form of this newly created void is strongly affected by

the intensity of the electron wind. At low electron wind intensities $\chi \leq 10$ as can be seen from Fig. (4.1.2), at first a large size slit shape internal void forms, which migrates slowly towards the lower surface attached to the substrate. Finally it hits the lower interface of the sample creating fatal and deep crack there. This process doesn't stop there, and rather repeats itself till the complete electrical breakdown takes place. On the other hand, at moderate and high electric wind intensities, $\chi = 25 - 50$, the almost cylindrical in shape and small in size internal void forms, which slowly drifts towards the cathode end of the sample as illustrated in Fig. (4.1.3). The size of these internal voids seems to be inversely proportional with the electron wind intensities. There is also strong tendency for the formation of multiple voids popping out from the same source, namely from the edge void, which may act as an continuous source up to certain extent. The incubation times for the creation of EM voids strongly depend on the applied electric field. At high electric fields, such as $X=50$, the small size void forms with relatively short incubation time. For the moderate electron wind intensities, the incubation time for the void creation becomes longer. At low electron wind intensities, a close observation shows that during long the incubation period, the slit like void embryo grows steadily, and finally detached from the mother edge-void, reaches the lower surface of the interconnect and causes fatal failure.

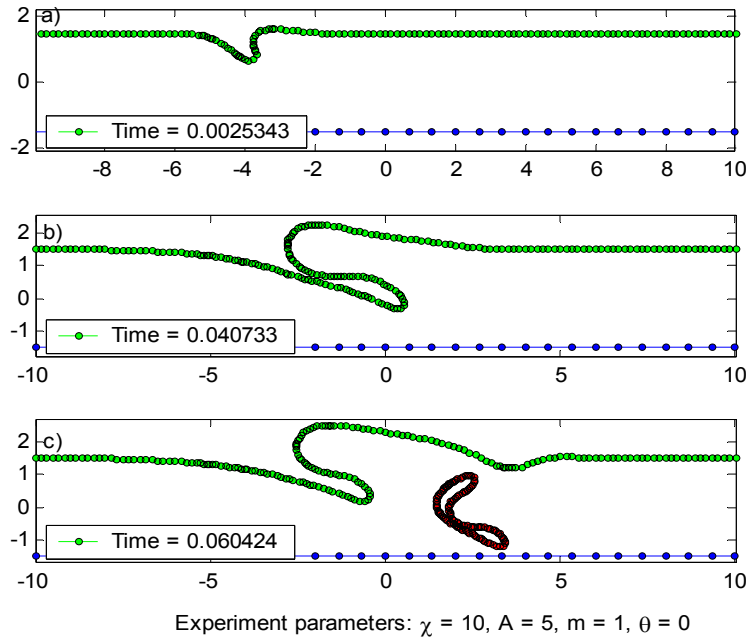


Figure 4.1.2: Surface morphology evolution for edge void. Slit like shape stretched to the windward direction and detachment of the void.

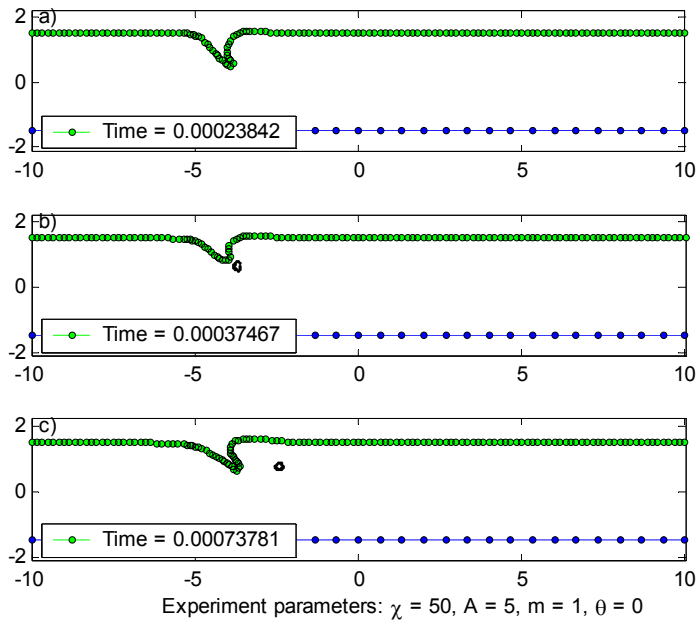


Figure 4.1.3: Morphological evolution of the surface at high electron wind intensity (small internal void).

As can be seen from Fig. (4.1.4), in the case of $\theta = 45$ degrees tilt angle, the edge-void, which is initially established on the flat surface starts to disappear after turning on the applied electric field, at low and moderate electron wind intensities $\chi \leq 25$ without leaving any trace. The intensity the applied electric field and the degree of diffusion anisotropy affect only the total decay time of the edge-void. At very high electron wind intensities $\chi \geq 50$, interconnects having 45° tilt orientation show EM induced voiding having extremely short life time. In this high EM regime, the edge-void perturbation is completely disappearing from the surface after popping up few, small and short leaving EM voids.

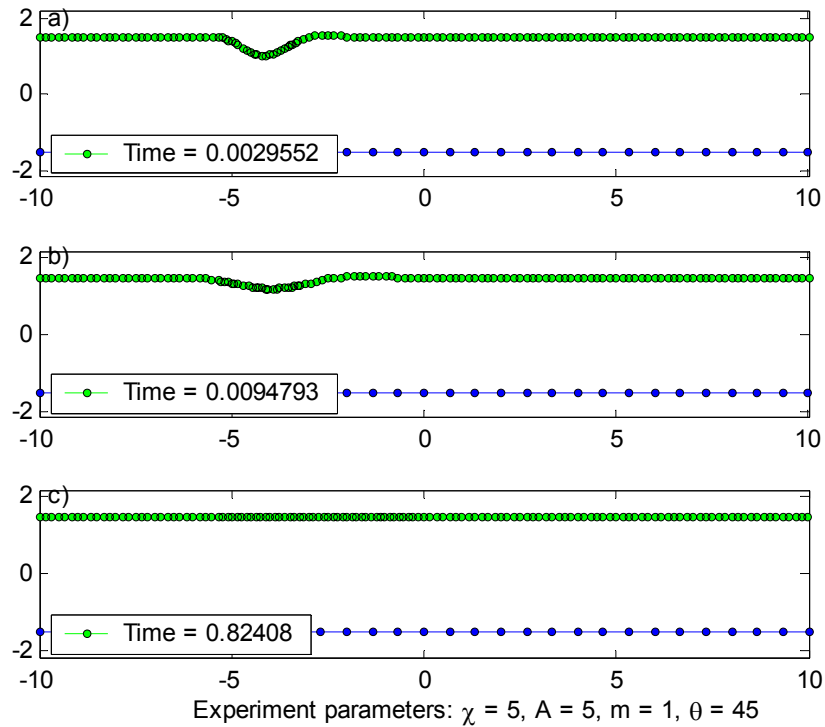


Figure 4.1.4: Morphological evolution of edge void to defect free surface (healing effect).

When the tilt angle changed to 90° , the edge-void changes its morphological evolution behavior totally, especially at low and moderate electron wind intensities. This is a typical and very unique regime as can be seen in Fig. (4.1.5) at which one observes the formation of a Solitary Wave by the transformation of the Gaussian shape into the wedge shape having sharp drop on leeward side. This Solitary Wave, which is first time detected by us in computer simulation experiments, migrates towards the cathode edge with constant velocity without showing any indication of dispersion and dissipation of energy. At very high electron wind intensity regime, the morphological evolution of the edge-void becomes extremely interesting, namely: the edge void changes its shape into the wedge form similar to the case mentioned above. But now! It starts to emanate very small and rounded shape void from its leeward side. This EM induced tiny void, as seen clearly in Fig. (4.1.6), starts to drift towards windward side, and passes its slowly dragging mother, and then continues in traveling in the direction of the cathode edge while tracing rather straight path. The rate of the overall processes is almost linearly depending on the diffusion anisotropy coefficient denoted by A in Ogurtani's formula.

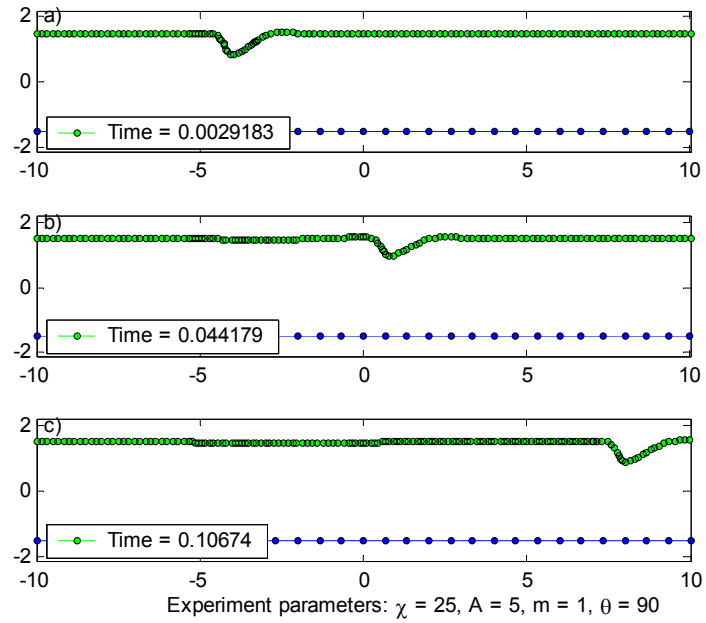


Figure 4.1.5: The formation of a Solitary Wave by the transformation of the Gaussian shape, and migration to cathode.

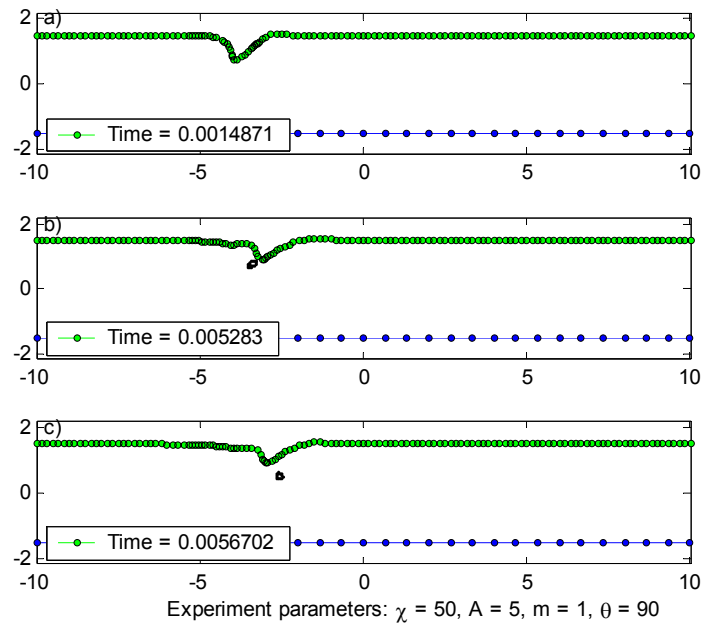


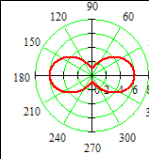
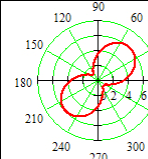
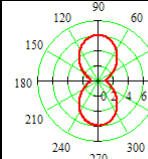
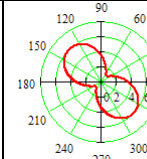
Figure 4.1.6: Morphological evolution of the surface at high electron wind intensity (small internal void).

$\theta = 135^\circ$ orientation of the tilt angle with respect to the direction of the electron wind is very critical for the development of the surface topography. The preset edge-void perturbation on the surface becomes unstable immediately after turning on the electric field. At first the Gaussian shape edge-void transform into a wedge having sharp edge on the windward side, and later the formation of oscillatory wave on the lee and windward sides appears with decreasing in amplitude in space. The wedge shape edge-void finally ejects a small but rounded internal void to the bulk region, and it disappears completely at the background oscillatory waves. These surface undulations continue to spread all along the surface in both directions. This phenomenon occurs regardless the intensity of the electron wind as long as $\chi \geq 1$, below which it may be stabilized because of the predominating effect of the capillary forces over the electron winds.

Geometrical behavior of edge void evolution for two fold crystal symmetry is summarized in Table 4.1 in this table failure, decay, and incubation times are also given. Abbreviations for the table are as follows:

- D – Decay
- G – Grow
- S – Solitary wave
- ST – Step like shape
- OS – Oscillatory wave
- I – Instability
- F – Rapture
- V – Void formation
- t_v – Void incubation time
- t_d – Void or Hillock decay time
- t_f – Failure time
- t_s – Starting time

Table 4.1.1: Summary of edge void evolution for two fold crystal symmetry.

VOID	θ	0	45	90	135
X	D m				
5	5	D $t_d = 0.5441$	D $t_d = 0.1417$	D $t_d = 0.83$	OS $t = 0.04585$ V $t_v = 0.3419$ F $t_f = 0.3675$
	10	V $t_v = 0.1474$ (slit like edge void grow)	D $t_d = 0.08177$	S G	OS $t_s = 0.026$ F $t_f = 0.1793$
10	5	V $t_v = 0.04168$	D $t_d = 0.09878$	S (with little grow)	OS $t_s = 0.01528$ V $t_v = 0.0709$
	10	V $t_v = .02011$	D $t_d = 0.03143$	S G $t_s = 0.00725$	OS $t_s = 0.00628$
25	5	V $t_v = 0.003014$	D $t_d = 0.0142$	S $t_s = 0.00245$ (without growth & shape change)	OS $t_s = 0.00295$ V $t_v = 0.00844$
	10	V $t_v = .00175$	D $t_d = 0.00323$	S $t_s = 0.00106$	OS $t_s = 0.00141$ V $t_v = 0.00598$
50	5	V $t_v = 0.000325$	V $t_v = 0.000616$	V $t_v = 0.00527$	OS $t_s = 0.001$ V $t_v = 0.0026$
	10	V $t_v = 0.0002$	V $t_v = 0.000362$	V $t_v = 0.00183$	OS $t_s = 0.00053$ V $t_v = 0.00236$

ii. Four Fold Crystal Symmetry, $\{100\}$ planes in FCC:

In Fig. (4.1.7), the effect of the low electron wind intensity $\chi \leq 10$ on the surface topology of an interconnect line with FCC structure having four fold crystal symmetry, and oriented with a tilt angle $\theta = 0$ degrees is illustrated. The originally Gaussian in shape edge-void on the surface starts to evolve into a kink shape disturbance, which shows continuous growth in size while drifting towards the cathode end of the interconnect line. At the moderate wind intensities $\chi \approx 25$, the kink shape surface disturbance breaks down and creates very large wedge shape internal void, while becoming very close to the opposite sidewall of the interconnect. On the other hand, at e. the extremely high electron wind intensities $\chi \geq 50$, the lower edge of the kinked shape surface void grows so much that eventually hits the opposite sidewall before having enough time to break down into internal daughter voids. Therefore this type textures are very critical and cause an open circuit failure by reaching the other edge. The failure time depends on the degree of anisotropy in diffusion coefficient and the electron wind intensity.

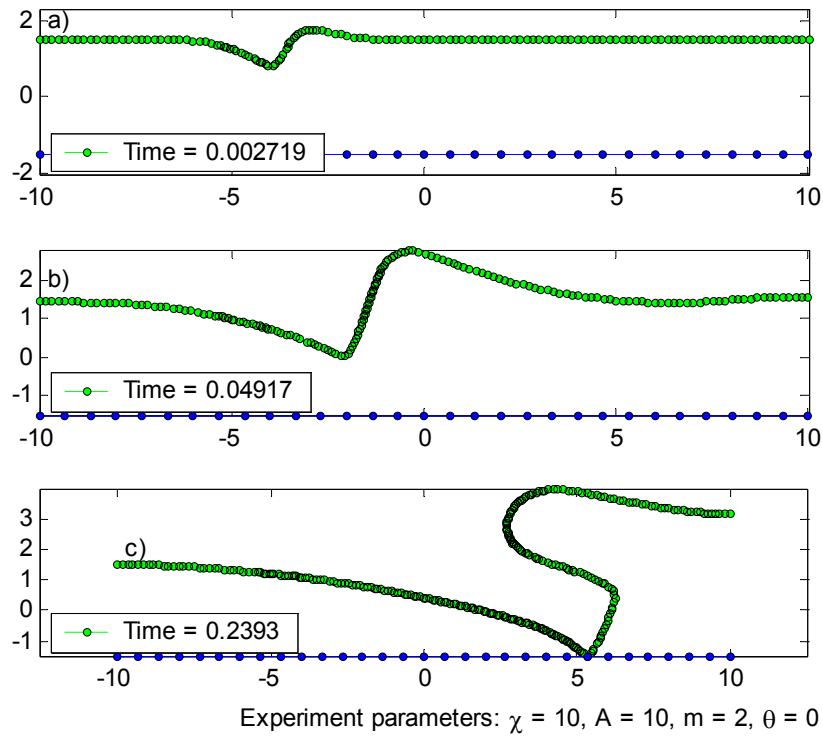


Figure 4.1.7: Morphological evolution of edge void to a kink shape disturbance. At final stage fatal failure of interconnect is seen.

We also investigated the case where the tilt angle is $\theta = 30$ degrees, and the general evolution behavior is demonstrated in Fig. (4.1.8) for low and moderate electron wind intensities $\chi = 5-10$. The void shows some shape variations while decaying and disappearing completely without leaving any trace on the otherwise flat surface. However, at very high electron winds $\chi \geq 50$ a round shape daughter void may be created, which migrates towards the cathode edge. There may be multiple daughter void emanating from the same source at later times.

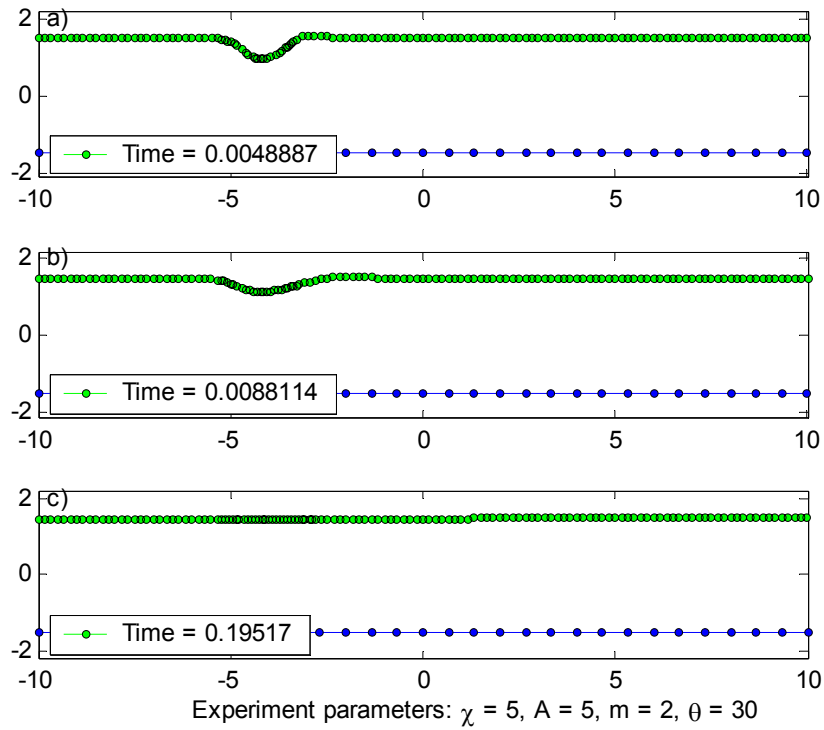


Figure 4.1.8: Morphological evolution of edge void to defect free surface (healing effect).

The effects of 45° tilt on the edge surface topology may be studied at two different categories, namely; the low electron wind intensity, $\chi \leq 10$, and high and moderate electron wind intensity, $\chi \geq 25$ regimes. The low current density regime disappears completely without leaving any trace on its back. In the case of moderate and current density domain, the edge-void changes its Gaussian shape by transforming into the slat-like configuration, and then emanates an internal void, which has almost perfect wedge form, pointing towards the windward direction. This wedge shape inner void migrates along the interconnect line towards the cathode end following a straight path. The mother edge-void after releasing the daughter void

slowly transforms into sawtooth type surface undulations. This highly localized the package of few sawtooth undulations starts to separate by adding more waves by keeping the original wave form invariant but increasing the number. This wave package drags towards the windward direction while keeping close track with motion of the drifting daughter void.

When the tilt angle is changed to 60° , the edge-void starts to decrease by generating surface undulations in all directions. The amplitudes of these waves become more pronounce and their wave form becomes sawtooth-like shape having relative steep windward edge. It seems that there is steady translational motion of this wave package towards the cathode end with constant growth in amplitudes.

Table 4.1.2: Summary of edge void evolution for four fold crystal symmetry.

VOID	θ	0	30	45	60
X	m				
	D				
5	5	K	D $t_d = 0.10695$	S (with growth)	OS $t_s = 0.01448$
	10	K F $t_f = 0.4706$	D $t_d = 0.06198$	S (with growth)	OS $t_s = 0.00851$
10	5	K	D $t_d = 0.1427$	S (with growth)	OS $t_s = 0.00553$
	10	K F $t_f = 0.2393$	D $t_d = 0.08804$	S (with growth)	OS $t_s = 0.00213$
25	5	K V $t_v = 0.10695$	D $t_d = 0.0367$	V $t_v = 0.0113$ (move to cathode)	OS $t_s = 0.00127$
	10	K F $t_f = 0.10695$	D $t_d = 0.02805$	V $t_v = 0.01672$ (move to cathode)	OS $t_s = 0.00053$
50	5	K	V $t_v = 0.00406$	V $t_v = 0.00306$	OS $t_s = 0.00042$
	10	K F $t_f = 0.10695$	V $t_v = 0.002223$	V $t_v = 0.0033$	OS $t_s = 0.00022$

iii. Six Fold Crystal Symmetry, $\{111\}$ planes in FCC:

The $\{111\}$ planes they have the highest symmetries compared to all other crystal planes in FCC structure. The orientation of the surface with zero tilt angle with respect to the electron wind direction at low current densities doesn't create very much trouble. As may be seen in Fig. (4.1.9) the edge-void while dragging towards the cathode end, with increasing in intensity, changes its form into a kink-shape, which is somewhat tilted towards the windward side. This form may cause an open

circuit failure by reaching the other edge but the failure time becomes very long relative to the interconnects having surfaces with other crystalline textures (symmetries). At moderate and high electron wind intensities, the tip of the kink-shape edge-void extends to much to the interior and a bottle neck forms. This bottle neck region finally breaks down, and creates very large internal void in wedge shape, which touches the opposite edge causes fatal circuit shut down.

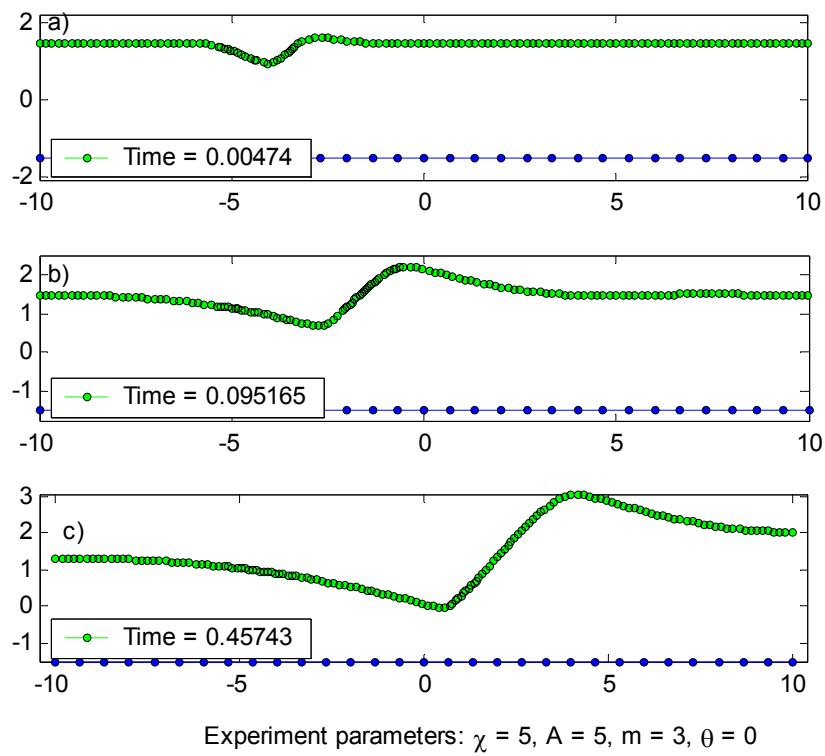


Figure 4.1.9: Morphological evolution of edge void to kink shape.

For 15° tilt angle, the edge-void regardless the intensity of the electron wind transform its shape into an inclined kink-form and migrates towards the cathode end with increasing in amplitude. The wave front becomes more and more steep on the leeward side, as can be seen in Fig. (4.1.10), during the traveling. At the end, it may

generate a step like surface morphology. After the step formed it may move towards cathode or stays stable. The situation may be more critical at very high current densities $\chi \geq 50$, and low aspect ratios, because of this steady increase intensity combining with steeping of the lee side, may cause substantial decrease in the cross section of the interconnect line and eventually circuit break down takes place by local joule heating.

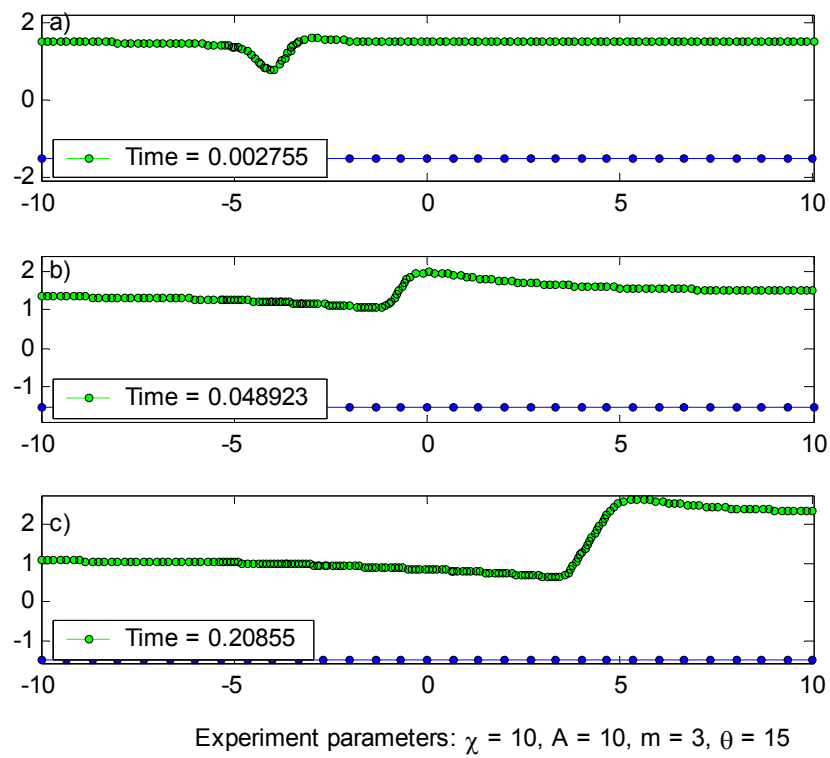


Figure 4.1.10: Formation of a step like surface morphology.

For 15° tilt angle, the edge-void regardless the intensity of the electron wind transform its shape into an inclined kink-form and migrates towards the cathode end with increasing in amplitude. The wave front becomes steeper on the leeward side, as can be seen in Fig. (4.1.10), during the traveling. At the end, it may generate a

step like surface morphology. After the step formed it may move towards cathode or stays stable. The situation may be more critical at very high current densities $\chi \geq 50$, and low aspect ratios, because of this steady increase intensity combining with steeping of the lee side, may cause substantial decrease in the cross section of the interconnect line and eventually circuit break down takes place by local joule heating.

When the orientation angle becomes 30° , as can be seen from Fig. (4.1.11) at low electron wind intensities, the edge-void transforms into a kink-shape step at the surface -having a steep edge on the windward side- which may multiply on the windward side while the wave package all together drifting towards the cathode end. At moderate and high electron wind intensities, a hip or hillock forms in front of traveling edge-void, which eventually over hangs and traps the edge-void as such that the edge void becomes an interior void. This very unusual process is more pronounce and fast when the diffusion anisotropy coefficient is low, about $A \leq 5$. This self-trapped void becomes wedge shape and drags towards the cathode end. During the traveling period, it may or may not touch the opposite edge of the interconnect dependence upon the aspect ratio and the size of the initial Gaussian edge void with respect to the line width.

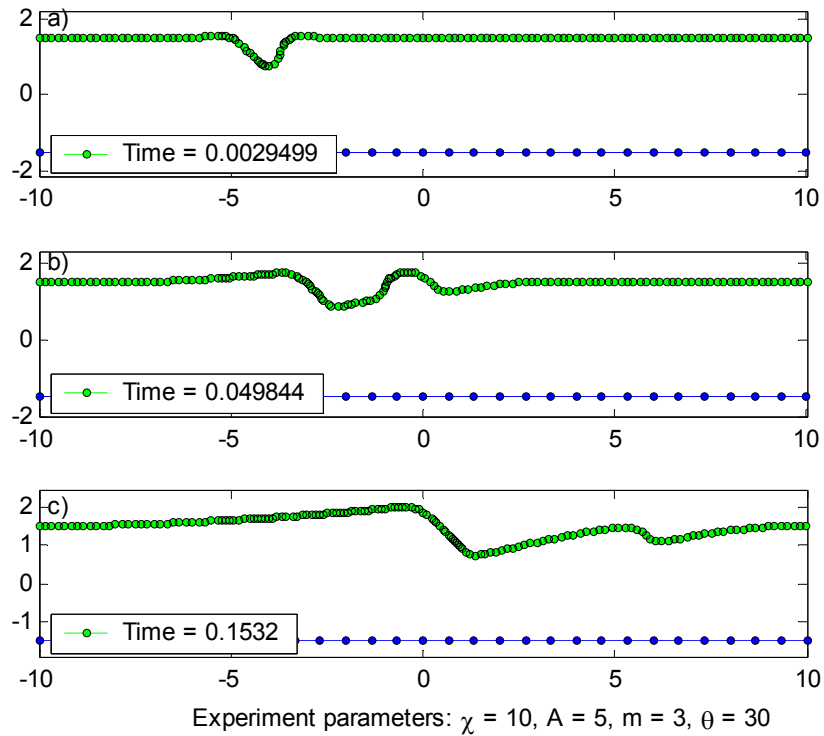
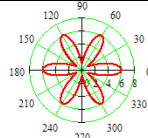
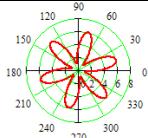
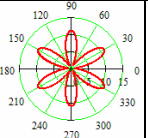
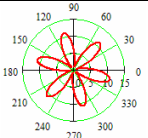
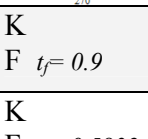
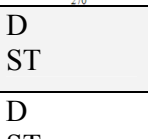
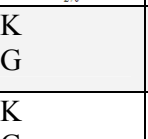
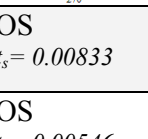


Figure 4.1.11: The edge-void transforms into kink-shape morphology.

The tilt angle 45° in six fold symmetry, transform the Gaussian edge-void into oscillatory waves. These waves start to appear with small amplitudes and they spread in all directions while enhancing their strength. The meanwhile, the distorted edge-void with decreasing in strength drags towards the cathode end carrying the all package of subsidiary oscillations. This resembles the light source making translational motion while constantly emanating light waves in all directions. There is one difference, the source strength for the present case increases with time. This is a good example for the behavior of a completely regenerative nonlinear system, where the source even appealingly decaying in size itself (better to say the broadening in space), still it soaks constant energy from the blowing electron winds.

Table 4.1.3: Summary of edge void evolution for six fold crystal symmetry.

VOID	θ	0	15	30	45
X	m				
	D				
5	5	K F $t_f=0.9$	D ST	K G	OS $t_s=0.00833$
	10	K F $t_f=0.5832$	D ST	K G	OS $t_s=0.00546$
10	5	K	D ST	K	OS $t_s=0.00397$
	10	K F $t_f=0.135$	D ST	K	OS $t_s=0.001907$
25	5	V $t_v=0.07426$ (huge)	D ST	V $t_v=0.079332$	OS $t_s=0.000839$
	10	F $t_f=0.06993$	D ST	K	OS $t_s=0.000457$
50	5	V $t_v=0.0018$ (move to cathode)	D ST	V $t_v=0.02618$	OS $t_s=0.000268$ V $t_v=0.00093$
	10	V $t_v=0.02415$	D ST	K	OS $t_s=0.000150$

4.2. Edge Hillock Configuration

During the examination of the evolution behavior of the edge- hillock morphologies under the action of the capillary and electrostatic fields, the following sample geometry is taken under consideration as in Fig. 4.1.1. As stated earlier the electric field is applied to the interconnect line from left to right direction. The scaled interconnect width and length is given by \bar{w} and \bar{L} , respectively. The height of the Gaussian shape Hillock is denoted as \bar{a} .

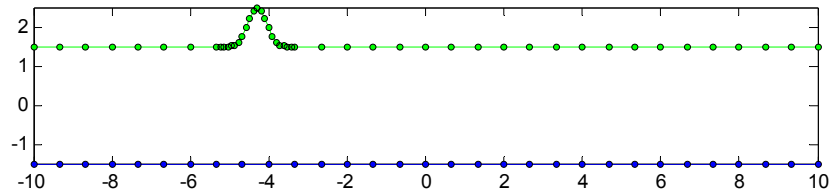


Fig. 4.2.1: Initial System with hillock. $\bar{w} = 3$, $\bar{a}=1$ and $\bar{L}=20$.

i. Two Fold Crystal Symmetry, $\{110\}$ plane in FCC:

The interconnect line with zero degree tilt angle and having a Gaussian shape of edge- Hillock shows two different types evolution behavior depending upon the applied electron wind intensity. As can be seen in Fig. (4.2.2), at very low current densities $\chi \leq 5$, the Hillock due time completely disappears leaving behind almost perfect flat surface. At low to high current densities, the situation is completely different. The top of the Hillock starts to over hangs on the leeward side. On the other hand, the lee side of the Hillock becomes more and more protruding deep into the bulk region, creating a bottle neck. The finally, the intruding part of the Hillock breaks down from the bottle neck portion becomes an interior wedge void. This newly created inner void, the size of which is somehow smaller higher the applied electron wind intensity, drifts towards the cathode end. The remaining part of the Hillock has still very long intrusion, which may act as a source for the multiple inner void generations by breaking-up.

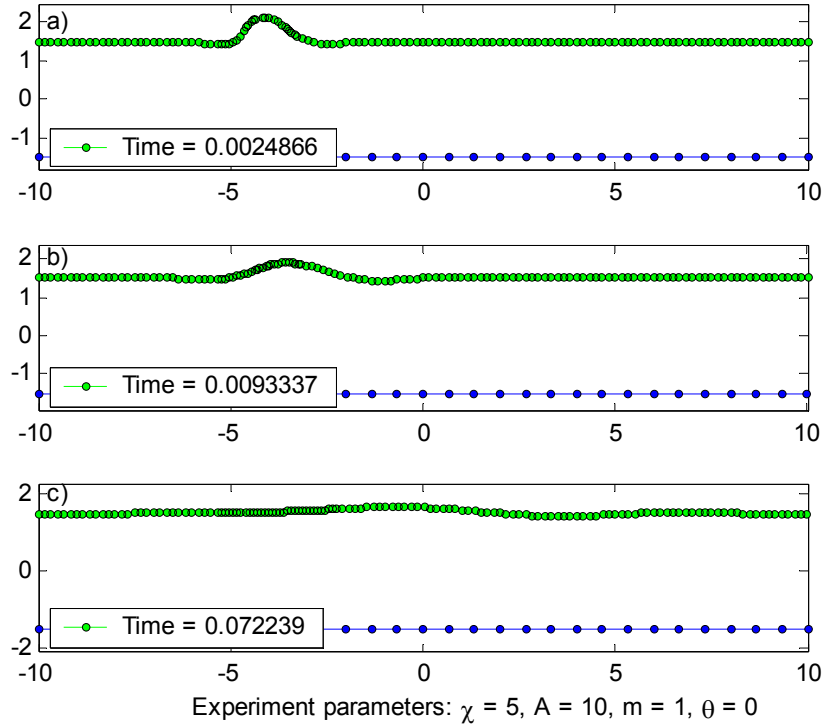


Figure 4.2.2: Morphological evolution of Hillock to perfect flat surface.

We also investigated the tilt angle 45° in our simulation studies, and the typical results obtained are illustrated in Fig. (4.2.3) and Fig. (4.2.4). There are two distinct regimes for this tilt angle, depending upon the applied electron wind intensities. For low and moderate electron wind forces $\chi = 5 - 25$, the edge-Hillock without changing its general form slowly broadens and finally disappears completely without leaving any trace behind. The decay time depends upon the electric field intensity inversely and the diffusion anisotropy linearly as can be seen in Table (4.2.1). For high electron wind intensities $\chi \geq 50$, very interesting topological evolution occurs, which first time is observed by the computer simulation in the literature. Namely, the edge Hillock because of very high wind starts to bend over

the leaside with certain degree of extrusion. Subsequently, this extruded part breaks up from the bottle neck portion, and becomes completely independent peach of object. In order to study the further behavior of this broken peace of metal, we allow it to be exposed to the electric applied electric field utilizing the fact that underlayer can act as shunt. The result as shown in Fig. (4.2.4) indicates that the broken peace takes the perfect circular shape and slowly drags towards the anode side of the interconnect line. The surface after the ejection of this peace of material becomes almost flat without any trace of perturbations.

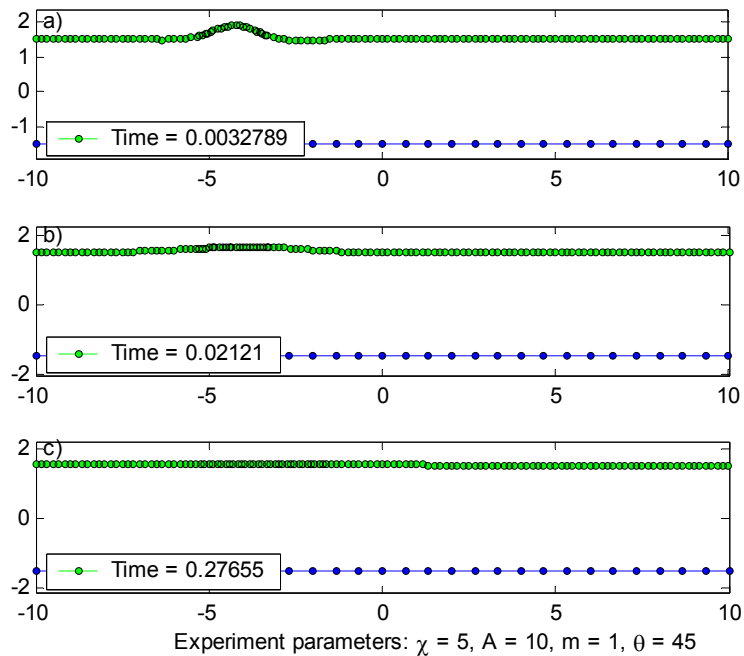


Figure 4.2.3: Morphological evolution of Hillock to perfect flat surface.

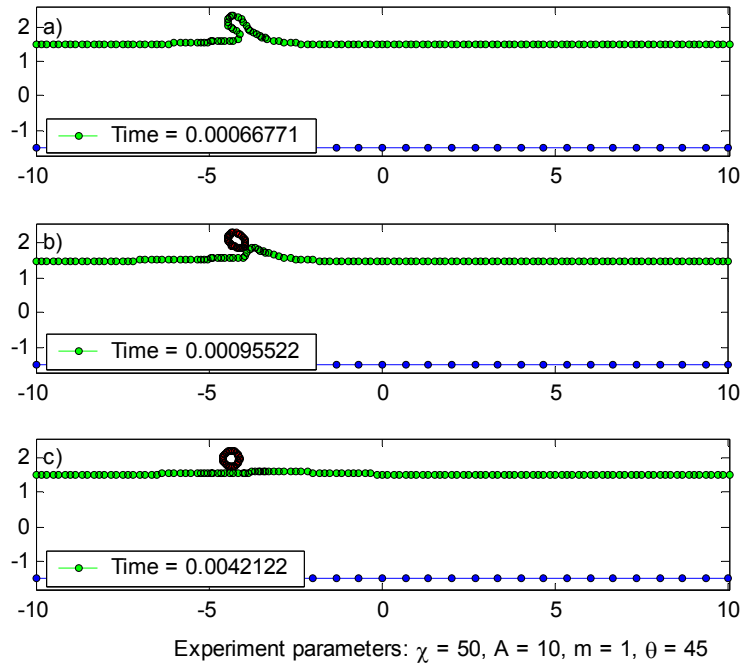


Figure 4.2.4: Morphological evolution of Hillock to the bottle neck and detachment of piece of metal.

The 90° tilting shows almost identical evolution morphologies regardless the intensity of the electron wind, only one modification, which occurs very high winds. The edge-Hillock transforms into edge-void shape, which migrates towards the cathode end. At moderate intensities a second edge-void may form behind the first one, creating doublet. For very high electron winds, the Hillock again transforms into an edge-void, which becomes intruded to the lee side, and finally breaking up from the neck region and generating a tiny inner void. It seems this process may repeat itself many times, since the leeward side of the edge void drifts much faster than the windward side; the both regions combine together at the top by trapping an empty space, which is nothing but a formation of an inner void. These newly formed inner voids migrate towards to cathode end. Strangely, this tiny void doesn't follow a straight path but rather takes a route which closely traces the

contour line of the edge-void. This is due to the strong current crowding taking place between the inner void and the edge-void because of the extremely high electron current densities plus the very close proximities between these two defects. The tilt angle 135° always represent extreme instability and the formation of oscillatory wave packages on the lee as well as on the windward sides of the edge-Hillock. The formation of the oscillatory waves doesn't cause any reduction of the strength of the Hillock. Eventually for the moderate and high electron wind intensities, the windward edge of the hillock starts to intrude to the interior of the bulk region. This follows up by necking and ejection of an interior void. Hillocks also join these waves. These oscillatory waves also detach into grain and migrate towards cathode.

Table 4.2.1: Summary of hillock evolution for two folds crystal symmetry.

HILLOCK	θ	0	45	90	135
X	D				
5	5	D $t_d = 0.03404$	D $t_d = 0.02509$	S (With growth)	OS $t_s = 0.0221$
	10	D $t_d = 0.0204$	D $t_d = 0.01635$	S (With growth)	OS $t_s = 0.0103$
10	5	V $t_v = 0.06384$	D $t_d = 0.01627$	S (With growth)	OS $t_s = 0.0165$
	10	V $t_v = 0.03606$	D $t_d = 0.007115$	S (With growth)	OS $t_s = 0.0034$
25	5	V $t_v = 0.00953$	D $t_d = 0.01369$	S (With growth)	OS $t_s = 0.0045$
	10	V $t_v = 0.006703$	D $t_d = 0.004735$	S (With growth)	OS $t_s = 0.0016$
50	5	V $t_v = 0.0028$	Detachment of piece of metal $t = 0.002095$	V $t_v = 0.01125$	OS $t_s = 0.001$ $Vt_v = 0.00321$
	10	V $t_v = 0.00181$	Detachment of piece of metal $t = 0.0009407$	V $t_v = 0.00946$	OS $t_s = 0.0005$

ii. Four Fold Crystal Symmetry

The four fold crystal symmetry combined with the zero tilt angle may be very troublesome for the interconnects. In all range of electron wind intensities $\chi = 5 - 50$ studied in this work, the edge-Hillock converts into a kink-like wave form, which immediately starts to multiply along the windward direction, especially at high electron wind intensities. The form of the individual waves are stabilized due time, by adapting almost perfect sawtooth shape. This spreading wave package shifts towards the cathode end. For the moderate electron winds, such as $\chi = 25$, the lee side of the hillock transform into wedge shape intrusion pointing to the windward direction. This intrusion produces a very large internal void. This giant size void has very unusual form as illustrated in Fig. (4.2.5), namely; wedge shape-doublet. Definitely it causes a fatal break down of the interconnect line, when hits the opposite edge.

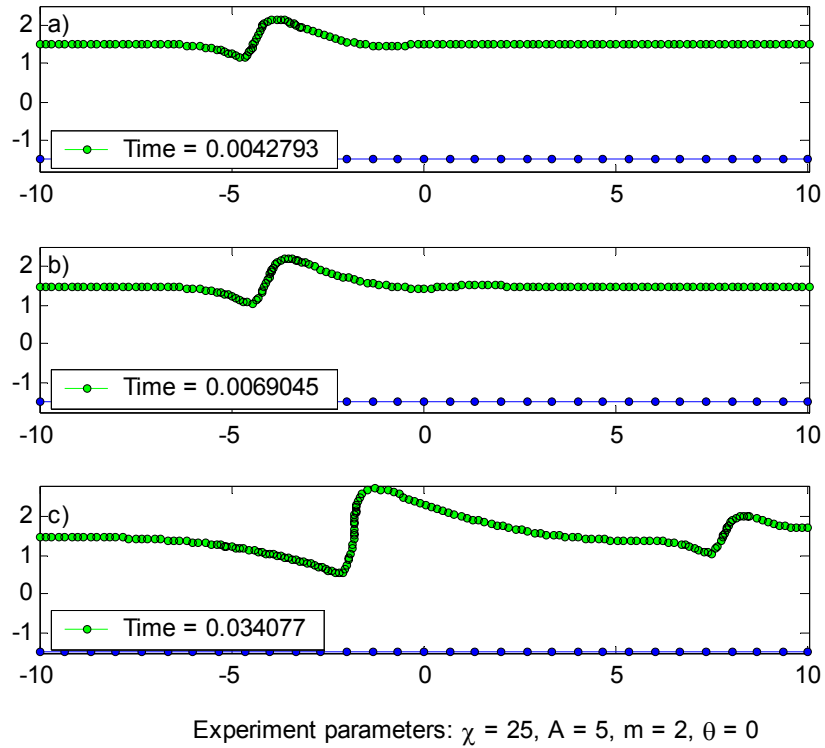


Figure 4.2.5: Hillock morphological evolution to a sawtooth shape.

As can be seen in Fig. (4.2.6), when the tilt angle becomes 30° , the edge-hillock at low and moderate electron wind intensities $\chi = 5 - 25$ dies off gradually, with minor modification in shape such as small bending to lee side. At high intensities as illustrated in Fig. (4.2.7) the Gaussian shape hillock transforms into finger shape hillock bending towards the leeside. This bend finger shape hillock grows without any change in form, and shift rather fast towards the cathode edge, if one uses a high diffusion anisotropy coefficient such as $A = 10$.

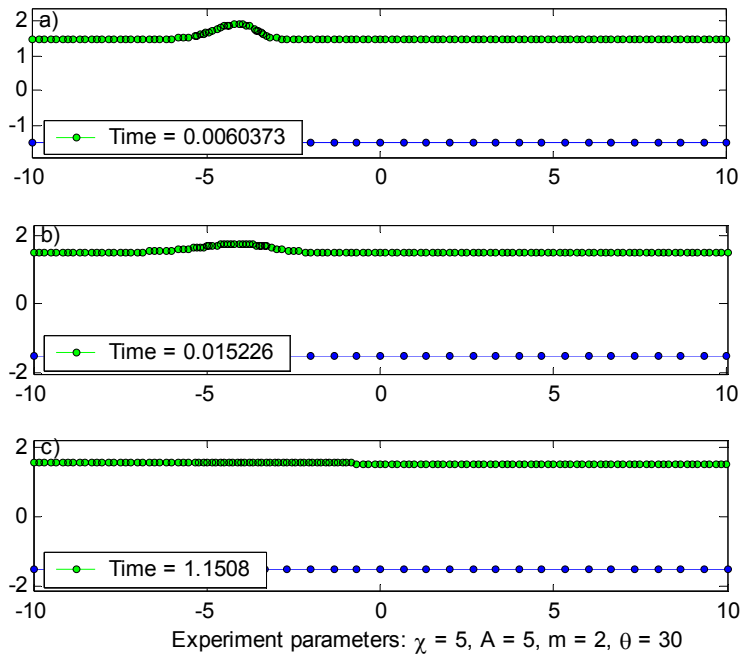


Figure 4.2.6: Morphological evolution of Hillock to perfect flat surface.

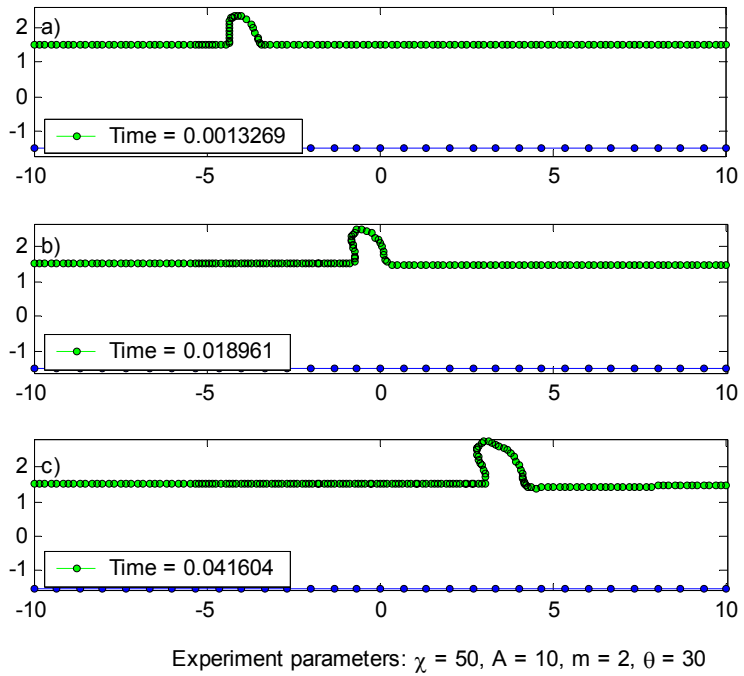


Figure 4.2.7: Morphological evolution of hillock to finger shape hillock.

The general evolution behavior of the edge-Hillock at 45° tilt angle is illustrated in Fig. (4.2.8) and Fig. (4.2.9), for low and high electron wind intensities, respectively. In both extreme cases, the first edge-hillock transforms into the sawtooth morphology, and shifts towards the cathode end. In the case of high electron winds, the multiplication in the number of saw teeth is very obvious while it is drifting steadily along the windward direction.

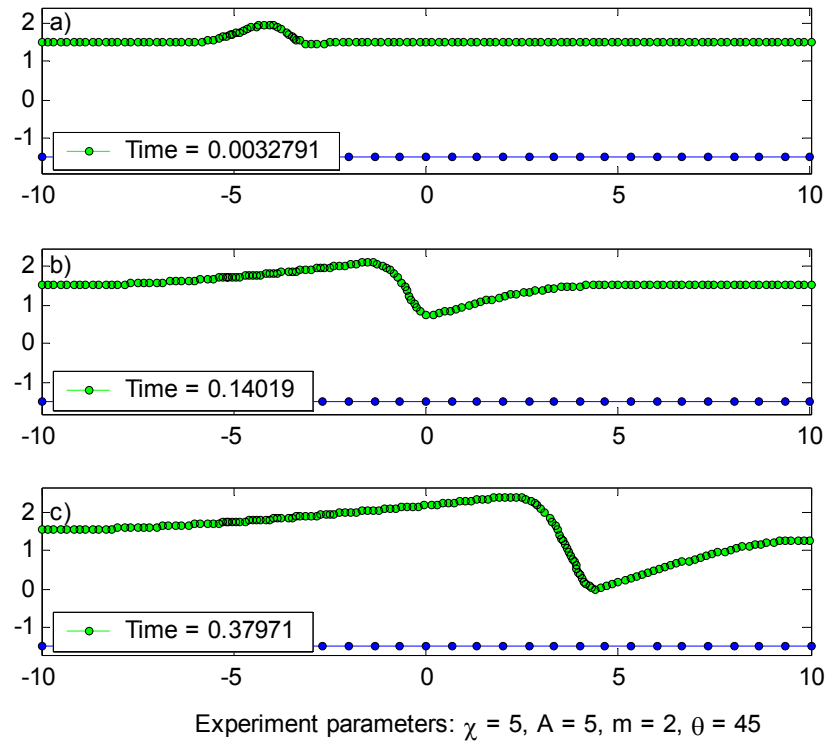


Fig 4.2.8: Morphological evolution of hillock to sawtooth morphology.

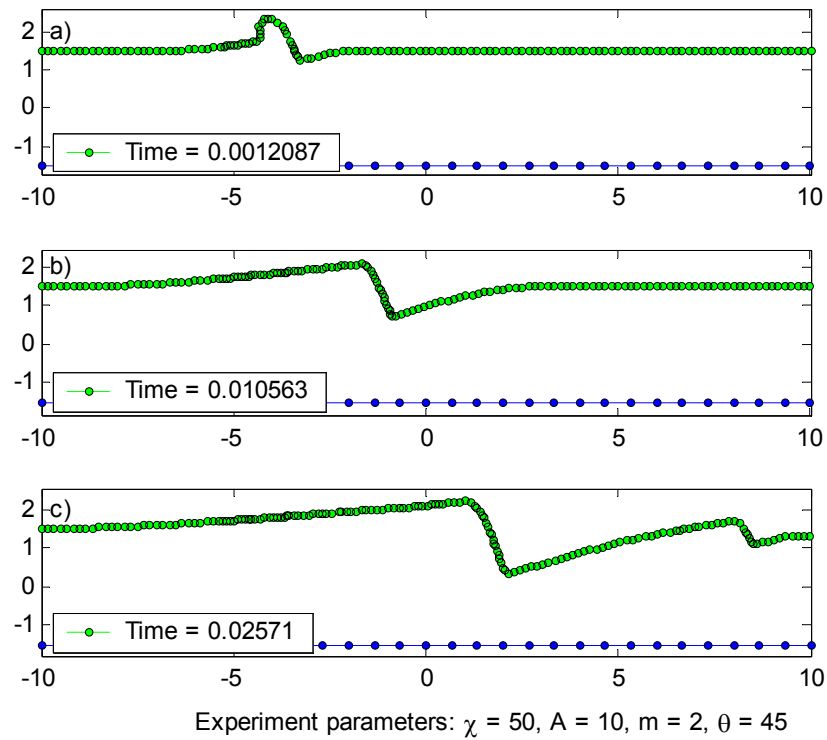


Figure 4.2.9: Morphological evolution of hillock to sawtooth morphology.

When the tilt angle changes to 60° , the surface becomes very unstable, and the oscillatory waves on lee as well as on windward sides start to appear with increasing in intensities. In later stages, the form of these waves transforms into the sawtooth shape having rather sharp windward front. A typical situation is illustrated in Fig. (4.2.10), where $\chi = 25$ and $A = 10$. the intensity of the electron winds doesn't affect the overall evolution behavior.

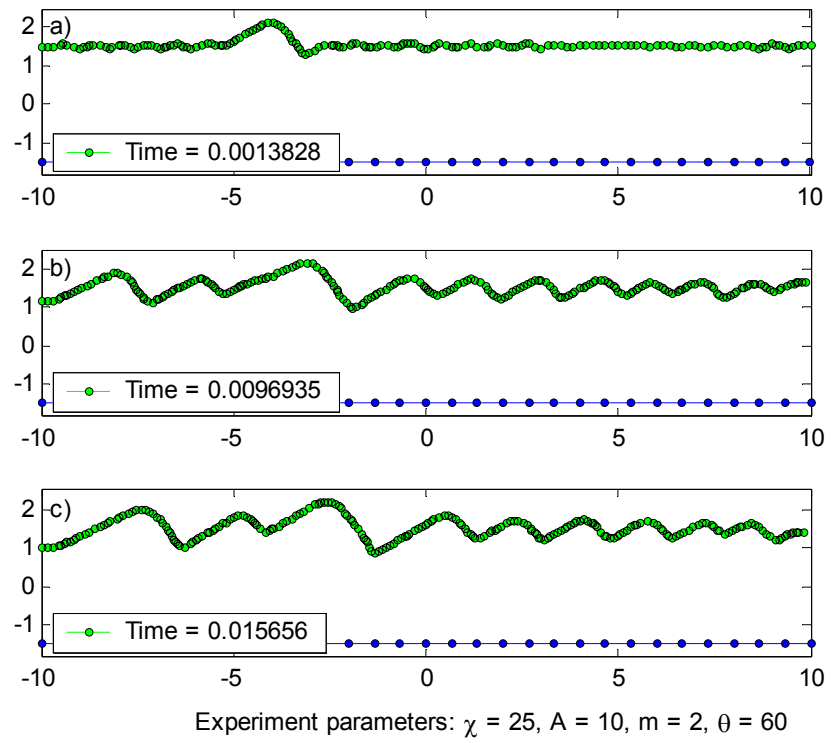
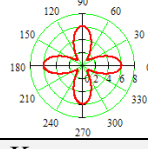
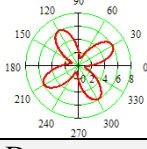
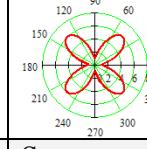
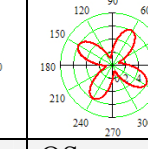
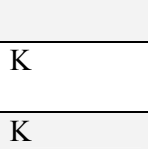
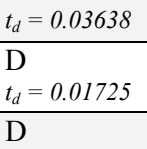
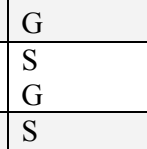
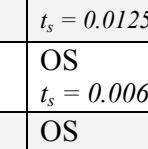


Figure 4.2.10: Formation of oscillatory waves from initial hillock.

Table 4.2.2: Summary of hillock evolution for four folds crystal symmetry.

HILLOCK	θ	0	30	45	60
X	m				
	D				
5	5	K	D $t_d = 0.03638$	S G	OS $t_s = 0.01259$
	10	K	D $t_d = 0.01725$	S G	OS $t_s = 0.00635$
10	5	K	D $t_d = 0.03604$	S G	OS $t_s = 0.004659$
	10	K	D $t_d = 0.01894$	S G	OS $t_s = 0.002054$
25	5	V $t_v = 0.11135$	D $t_d = 0.01711$	S G	OS $t_s = 0.001345$
	10	F $t_f = 0.0525$	D $t_d = 0.0175$	S G	OS $t_s = 0.0006202$
50	5	K G	Hillock move to cath. with decay $t_d = 0.11818$	Double edge void	OS $t_s = 0.000358$
	10	K G	Hillock move to cathode without decay	Double edge void	OS $t_s = 0.000226$

iii. Six Fold Crystal Symmetry, $\{111\}$ planes in FCC:

The finally we have performed very extensive simulation studies to investigate the evolution behavior of $\{111\}$ planes in FCC structures which are subjected to the Gaussian shape extrusions (hillocks) and oriented with various degrees of tilting with respect to the applied electric field. Again the surface drift-diffusion coefficient is chosen as anisotropic, $A = 5-10$ and the applied electron wind intensity spanning a large range of values, $\chi = 5-50$.

The orientation or tilt angle zero with respect to the wind direction results almost similar and sawtooth shape oscillations formations after edge-hillocks convert themselves into the kink-shapes. This evolution kinetics is very speedy at very high electron winds $\chi \geq 50$ such as that immediately formation of the daughter kink shape perturbation takes place on the windward side of the hillock while it was converted in form. The latter stage, the lee side of the converted hillock protrudes and finally hangs over itself creating a bottle neck. The large piece of material ruptures from this bottle neck, leaves the interconnect line, and drifts towards the anode end. In order to simulate this event, which is illustrated in Fig. (4.1.11), the underlayer is assumed to be acting as a shunt for the applied electrostatic field. Therefore, the broken away piece is still subjected to the applied electron wind. After this rupture, the remaining part of the hillock becomes sawtooth in shape and continuous to drift to the cathode end. Meanwhile more and more subsidiary waves are generated on the windward side. The complete package, made up by sawtooth waves, drags towards the cathode end by constantly increasing the number of their members at the front (multiplication). However, this process breaks down when the lower edge of the preceding wave, which is nothing but the original hillock with different face, touches the opposite edge of the interconnect line. At low electron wind, the hillock transform into step like wave front, and proceeds drifting towards the cathode.

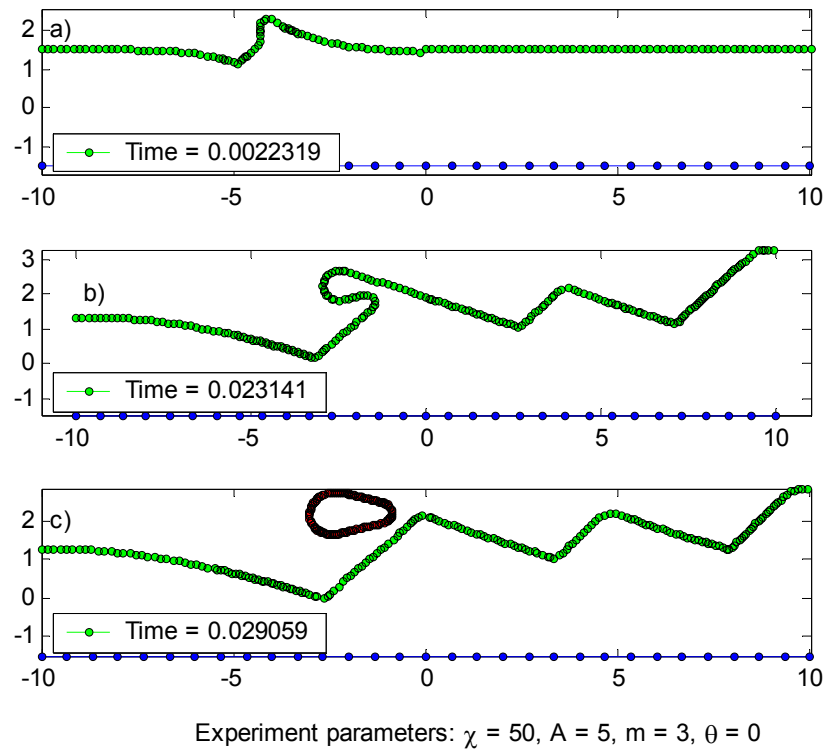


Figure 4.2.11: Morphological evolution of hillock to the kink-shapes and detachment of piece of metal.

For 15° tilt angle, the edge hillock transforms into step like wave, which slowly decays off while shifting towards the cathode side. However, at moderate and high electron winds $\chi \geq 25$, the step like wave starts to grow steadily, while drifting with constant speed in the windward direction. Eventually, the lower edge of the wave front may touch the opposite edge of the interconnect line, and terminates the process completely (electrical shut down).

The edge-hillock transforms into a negative kink-shape wave by lifting up the leeward side, when the tilt angle becomes 30° . This negative kink-wave drifts towards the cathode end with increasing intensity without showing any change in its form. At high electron wind intensities such as $\chi \geq 50$, the multiplication takes place on the windward side. The overall picture looks like a chain of sawtooth waves shifting with uniform speed towards the cathode edge. This process may continue till the lower edge of the preceding wave touches the opposite side of the interconnect line, and breaking the electrical circuit.

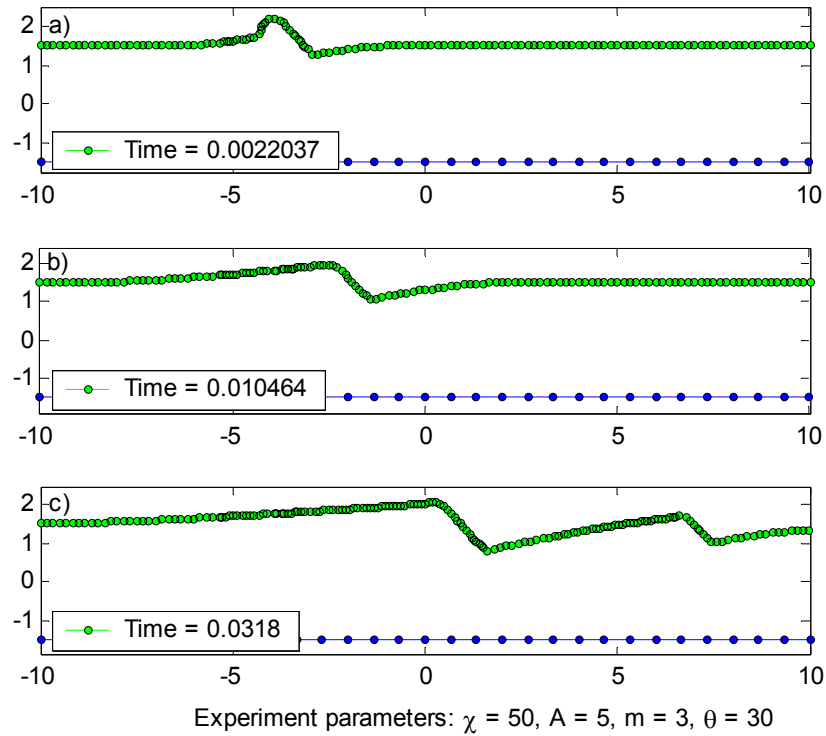


Figure 4.2.12: Morphological evolution of hillock to the negative kink-wave.

We have also investigated a single crystal (FCC) interconnect line having $\{111\}$ surface structure with 45 degrees tilt angle. The Gaussian shape hillock on this plane regardless the intensity of the electron wind shows very unstable behavior. Immediately after it is exposed to the electron wind, the oscillatory waves are produced in both directions. As illustrated in Fig. (4.1.13) these waves grow, while they are drifting towards the cathode end. The anode end shows very much depletion at very high electron wind intensities. This may be due to limited size of the interconnect length adopted in the present simulations experiments in order save the computation time.

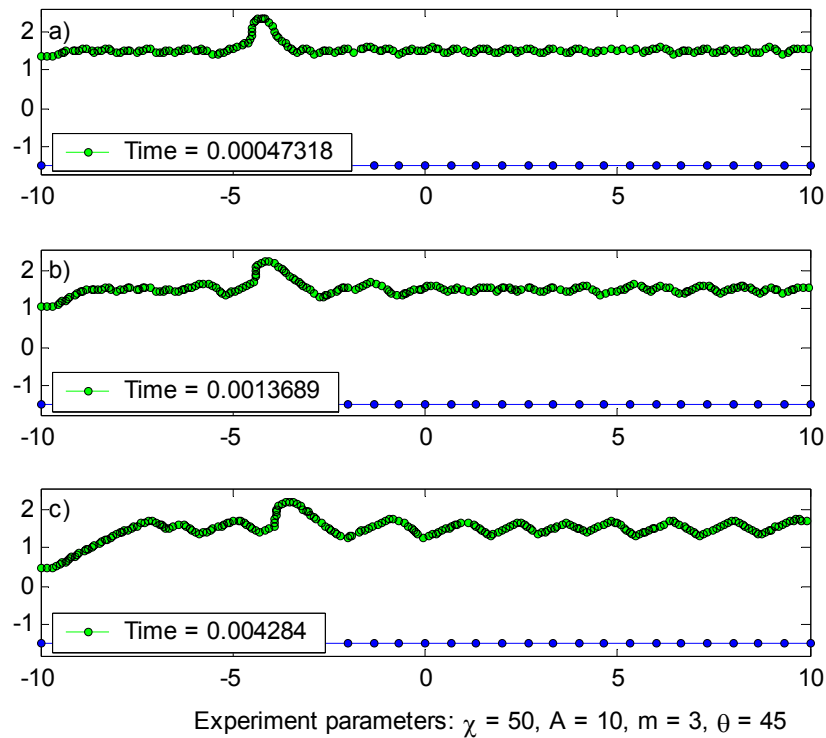
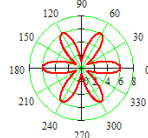
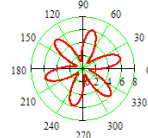
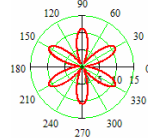
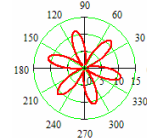


Figure 4.2.13: Morphological evolution of hillock to the oscillatory waves.

Table 4.2.3: Summary of hillock evolution for six folds crystal symmetry.

HILLOCK	θ	0	15	30	45	
X	D m					
		5	K F $t_f = 1.112$	D $t_d = 0.0329$	K G	OS $t_s = 0.0094$
		10	K F $t_f = 0.4152$	D $t_d = 0.03445$	K G	OS $t_s = 0.0030$
		10	K	D $t_d = 0.04625$	K G	OS $t_s = 0.0025$
25	5	K F $t_f = 0.3105$	D ST	K G	OS $t_s = 0.00056$	
	10	K F $t_f = 0.07425$	ST F $t_f = 0.1264$	K G	OS $t_s = 0.00028$	
50	5	Detachment of piece of metal $t = 0.0285$	V $t_d = 0.002478$	K G	OS $t_s = 0.00021$	
	10	K	D ST	K G	OS $t_s = 0.000113$	

CHAPTER 5

CONCLUSIONS

This computer simulation experiments show that the surface crystal structure is extremely important in the determination of the life time of thin film single crystal interconnect lines. Under the applied electrostatic field not only the degree of rotational symmetry (parameter, m) but also the orientation of the surface plane play dominant role in the development of the surface topology and the formation of the fatal EM induced voids. The degree of anisotropy in the surface diffusion coefficient, and the intensity of the electron wind parameter may have great influence on the evolution regime actually taking place on the surfaces and at sidewalls of the interconnects.

Also it has been discovered that the changing the tilt angle for a given crystal plane can cause a significant topological changes at the surface. The stable void or hillock formation or their complete disappearance may dependent on the tilt angle. Similarly, the large tilt angles such as 130° in two fold symmetry causes extreme in surface instabilities. The conditions under which the EM induced inner void may be created? And if they do! Then what type morphology (wedge, slit or round) may be adapted by them? The answers for all these questions are strictly rely on the surface texture of the interconnect lines, and their service operating conditions such as temperature and current density.

BIBLIOGRAPHY

- N., Tu K. (2003). J. Appl. Phys. **94**(9): pp. 5451.
- E., OREN E. and O., OGURTANI T. (2002). Mat. Res. Soc. Symp. Proc. **695** pp. L5.5.1.
- AVERBUCH A. and ISRAELI M. et al. (2002). .
- E., Liniger and L., Gignac et al. (2002). J. Appl. Phys. **92**(4): pp. 1803.
- O., OGURTANI T. and E., OREN E. (2001). J. Appl. Phys. **90**(3): pp. 1564.
- M., KHENLER and A., AVERBUCH et al. (2001). J. Comput. Phys. **170** pp. 764.
- L., Michael N. and C-U., Kim (2001). J. Appl. Phys. **90**(9): pp. 4370.
- SCHIMSCHAK M. and J., KRUG (2000). J. Appl. Phys. **87**(2): pp. 695.
- M., SCHIMSCHAK and J., KRUG (2000). J. Appl. Phys. .
- K., SASAGAWA and M., HASEGAWA et al. (2000). Theoretical and Applied Fracture Mechanics **33** pp. 67.
- MAHADEVAN M. and M., BRADLEY R. (1999). Phys. Rev. B **59**(16): pp. 11037.
- R., FRIDLIN D. and F., BOWER A. (1999). J. Appl. Phys. **85**(6): pp. 3168.
- MAHADEVAN M. and M., BRADLEY R. (1999). Phys. Rev. B **59**(16): pp. 11037.

GUNGOR M.R. and D., MAROUDAS (1999). J. Appl. Phys. **85**(4): pp. 2233. GUNGOR M.R. and D., MAROUDAS (1998). Surface Sci. Lett. **415** pp. 1055.

SCHIMSCHAK M. and J., KRUG (1998). Phys. Rev. Lett. **80**(8): pp. 1674.

F., Fantini and R., LLOYD J. et al. (1998). Microelectronic Engineering **40** pp. 207.

SCHIMSCHAK M. and J., KRUG (1997). Phys. Rev. Lett. **78**(2): pp. 278.

GUNGOR M.R. and D., MAROUDAS (1997). Phys. Rev. Lett. .

R., LLOYD J. (1997). Semicond. Sci. Technol. **12** pp. 1177.

O., KRAFT and E., ARZT (1997). Acta metall. **45**(4): pp. 1599.

G., Pierce D. and G., Brusius P. (1997). Microelectron. Reliab. **37**(7): pp. 1053.

MAHADEVAN M. and M., BRADLEY R. (1996). J. Appl. Phys. **79**(9): pp. 6840.

W., WANG and Z., SUO et al. (1996). J. Appl. Phys. **79**(5): pp. 2394.

MAHADEVAN M. and M., BRADLEY R. (1996). J. Appl. Phys. **79**(9): pp. 6840.

T., MARIEB and P., FLINN et al. (1995). J. Appl. Phys. **78**(2): pp. 1026.

SCHIMSCHAK M. and J., KRUG (1995). Phys. Rev. B **52**(11): pp. 8550.

T., MARIEB and P., FLINN et al. (1995). J. Appl. Phys. **78**(2): pp. 1026.

Z., SUO and W., WANG et al. (1994). Appl. Phys. Lett. **64**(15): pp. 1944.

E., ARZT and O., KRAFT et al. (1994). J. Appl. Phys. **76**(3): pp. 1563.
J., TAO and W., CHEUNG N. et al. (1993). IEEE Transactions on Electron Dev.
14(5): pp. 249.

H., ROSE J. (1992). Appl. Phys. Lett. **61**(18): pp. 2170.

E., SANCHEZ J. and T., McKNELLY L. et al. (1992). J. Appl. Phys. **72**(7): pp. 3201.

E., ARZT and D., NIX W. (1991). J. Mater. Res. **6**(4): pp. 731.

LI C.Y. and BORGESSEN P. et al. (1991). Appl. Phys. Lett. **59**(12): pp. 1464.

KNORR D.B. and TRACY D.B. et al. (1991). Appl. Phys. Lett. **59**(25): pp. 3241.

S., HO P. and T., KWOK (1989). Rep. Prog. Phys. **52** pp. 301.

H., VERBRUGGEN A. (1988). IBM J. Res. Develop. **32**(1): pp. 93.

C., CHANG and H., HUANG (1983). J. Appl. Phys. **54**(5): pp. 2287.

LOBOTKA P. and I., VAVRA (1981). Phys. Stat. Sol. (a) **63** pp. 655.

SCHREIBER H.U. and B., GRABE (1981). SolidState Electronics **24**(12): pp. 1135.

S., VAIDYA and T., SHENG T. et al. (1980). Appl. Phys. Lett. **36**(6): pp. 464.

N., YEREMIN E. (1979). pp. 215.

A., BLECH I. (1976). J. Appl. Phys. **47**(4): pp. 1203.

- A., BLECH I. and C., HERRING (1976). Appl. Phys. Lett. **29**(3): pp. 131.
- P., GLANSDORFF and I., PRIGOGINE (1971). pp. 126.
- S., HO P. (1970). J. Appl. Phys. **41**(1): pp. 64.
- R., BLACK J. (1969). Proceedings of the IEEE **57**(9): pp. 1587.
- R., HAASE (1969). pp. 245.
- I., PRIGOGINE (1961). pp. 28.
- B., HUNTINGTON H. and R., GRONE A. (1961). J. Phys. Chem. Solids **20**(76):.
- A., GUGGENHEIM E. (1959). pp. 46.
- P., BUFF F. (1955). J. Chem. Phys. **23** pp. 419.
- C., HERRING (1951). Phys. Rev. **82**(1): pp. 87.
- R., De GROOTS. (1951). pp. 98.
- Th., De DONDER and P., Van RYSELBERGHE (1936). .
- E., VERSCHAFFELT J. (1936). Bull. Ac. Roy. Belgium (Cl. Sc.) **22** pp. 373.
- WAALS, Van Der and D., BAKER J. (1928). **6**.
- O., OGURTANI T. (2000). "Irreversible Thermokinetics Theory of Surfaces and Interfaces with a Special Reference to Triple Junctions (unpublished)".

GUNGOR M.R. and D., NIX W. "A new mathematical model for void grain boundary interaction (unpublished)".

S., VAIDYA and A.K., SINHA "Effect of texture and grain structure on electromigration in Al0.5%Cu thin films".

R., LLOYD J. "Electromigration for Designers". Simplex solutions .

E., OREN E. "M. Sc. Thesis, Middle East Technical University (2000)".

E., OREN E. "PhD. Thesis, Middle East Technical University (2003)".

OREN E.E. and O., OGURTANI T. "The effect of initial void configuration on the morphological evolution under the action of normalized electron wind forces (unpublished)".

J., GLEIXNER R. and D., NIX W. (1999). J. Appl. Phys. **86**(4): pp. 1932.

SMITH R.W. and D., SROLOVITZ J. (1996). J. Appl. Phys. **79**(3): pp. 1448.

G., COLGAN E. and Y., LI C. et al. (1987). "Void formation in thin Al films". Appl. Phys. Lett. **51**(6): pp. 424.

ZEHE A. and G., RÖPKE (1985). "The effect of impurities on the formation of voids by electromigration in metallic alloys". pp. 407.

CHU X. and MULLINS W.W. et al. (1997). " Spreading of a void along a singular surface during electromigration : A failure mode". Appl. Phys. Lett. **70**(2): pp. 194.

Y., TAKAHASHI and K., TAKAHASHI et al. (1991). "A numerical analysis of void shrinkage process controlled by Cu surface and interface diffusion". Acta. metall. mater. **39**(12): pp. 3199.

APPENDIX

SELECTED EXPERIMENT RESULTS

Initial states of hillock and edge void configuration:

Initial Edge Void Configuration:

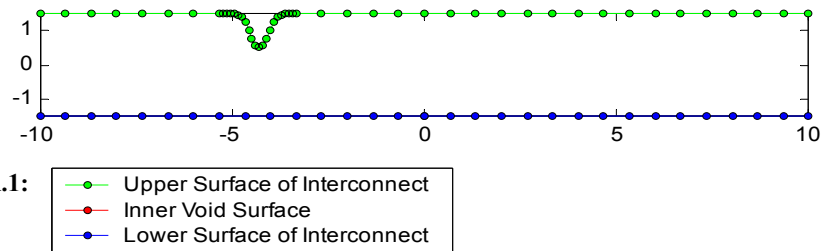


Figure A.1:
 - Upper Surface of Interconnect
 - Inner Void Surface
 - Lower Surface of Interconnect

Initial Hillock Configuration:

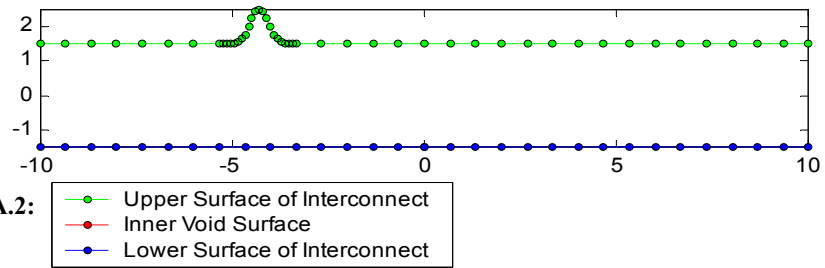


Figure A.2:
 - Upper Surface of Interconnect
 - Inner Void Surface
 - Lower Surface of Interconnect

EXPERIMENT RESULTS:

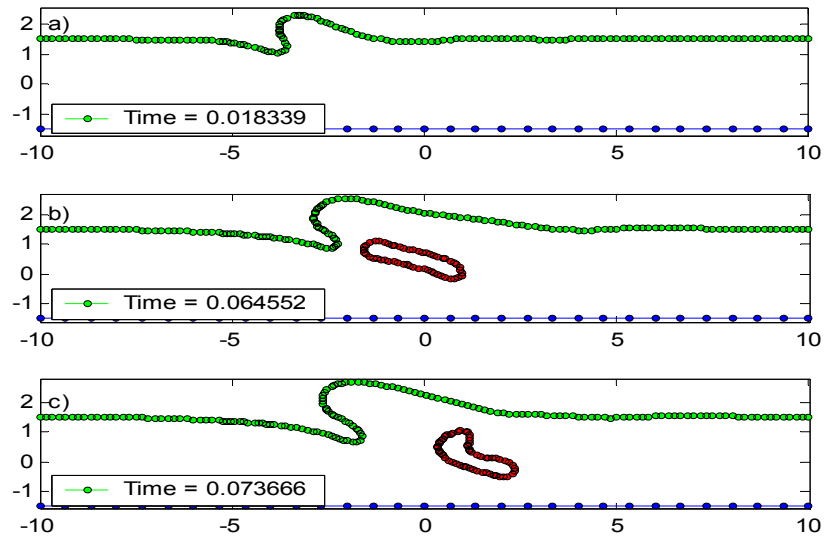


Figure A.3: * Result is shown for Hillock with $\chi = 10$, $A = 5$, $m = 1$, $\theta = 0$

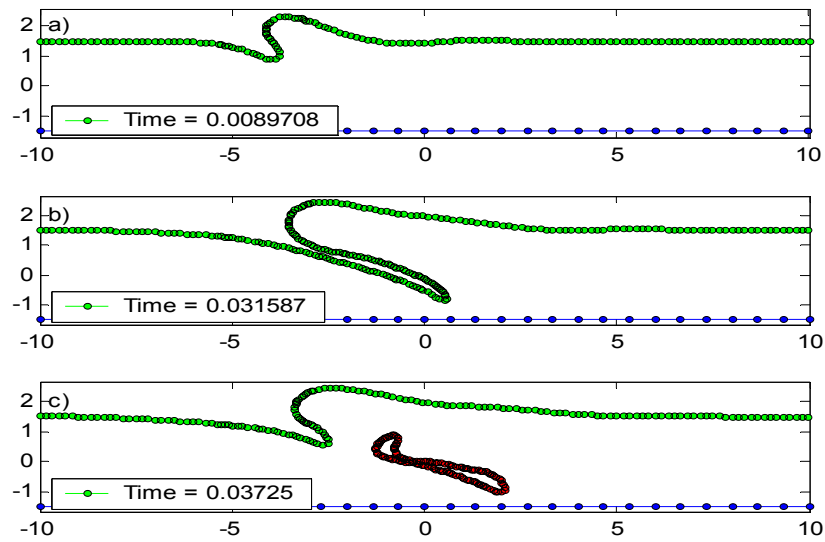


Figure A.4: * Result is shown for Hillock with $\chi = 10$, $A = 10$, $m = 1$, $\theta = 0$

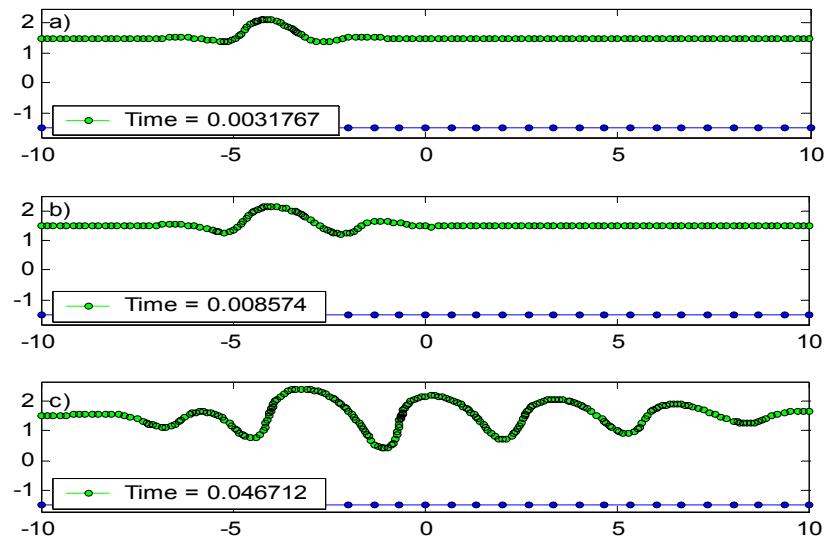


Figure A.5: Result is shown for Hillock with $\chi = 5$, $A = 10$, $m = 1$, $\theta = 135$

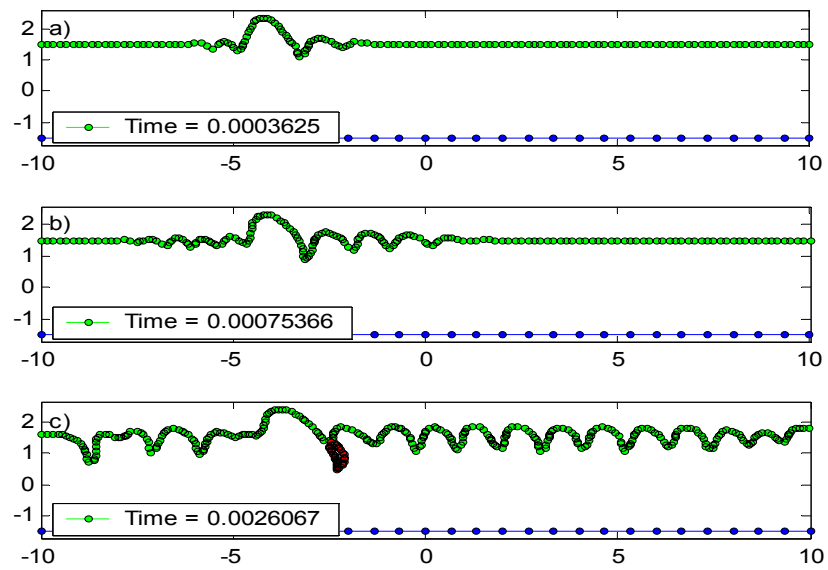


Figure A.6: Result is shown for Hillock with $\chi = 50$, $A = 10$, $m = 1$, $\theta = 135$

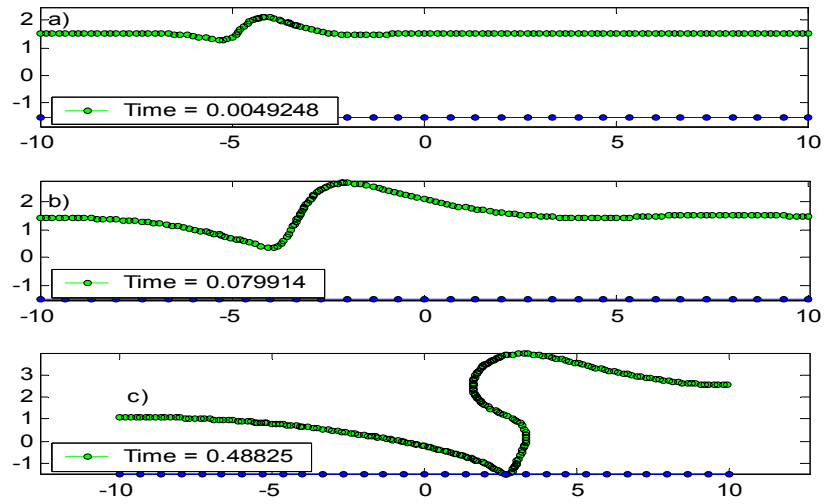


Figure A.7:* Result is shown for Hillock with $\chi = 5$, $A = 10$, $m = 2$, $\theta = 0$

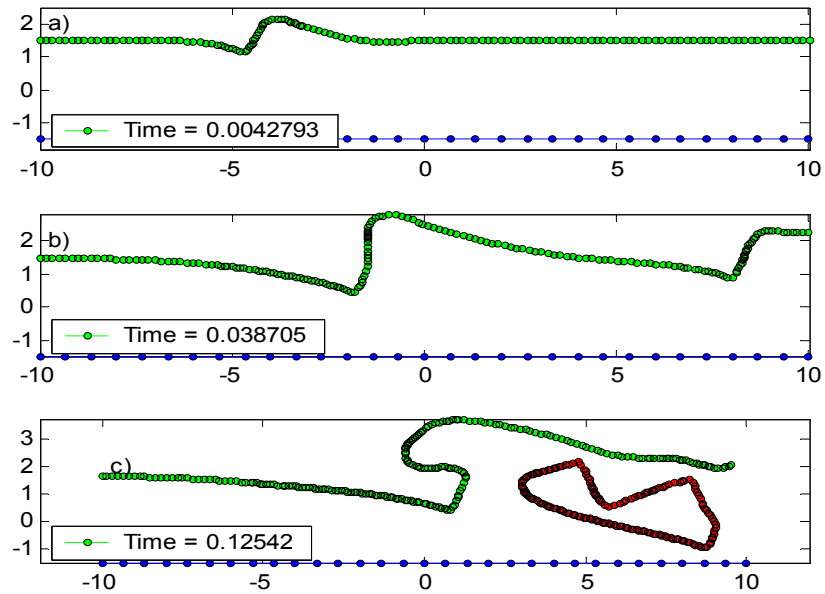


Figure A.8:* Result is shown for Hillock with $\chi = 25$, $A = 5$, $m = 2$, $\theta = 0$

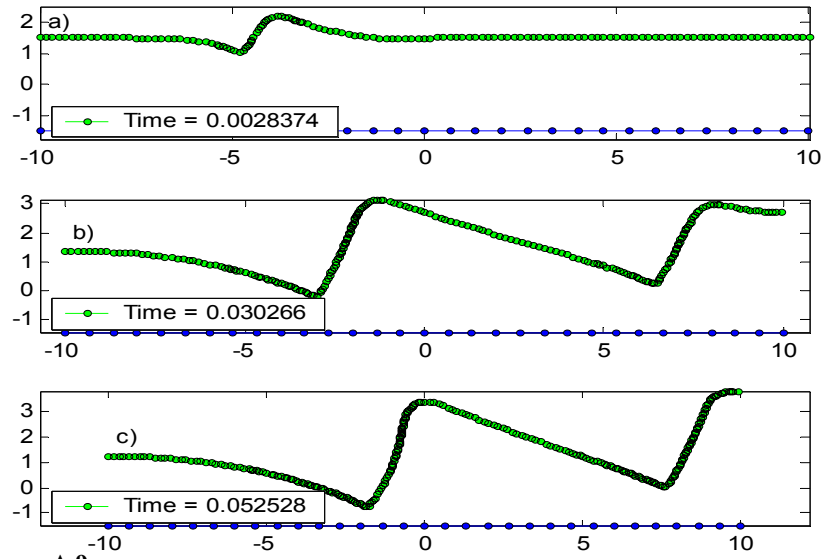


Figure A.9: * Result is shown for Hillock with $\chi = 25$, $A = 10$, $m = 2$, $\theta = 0$

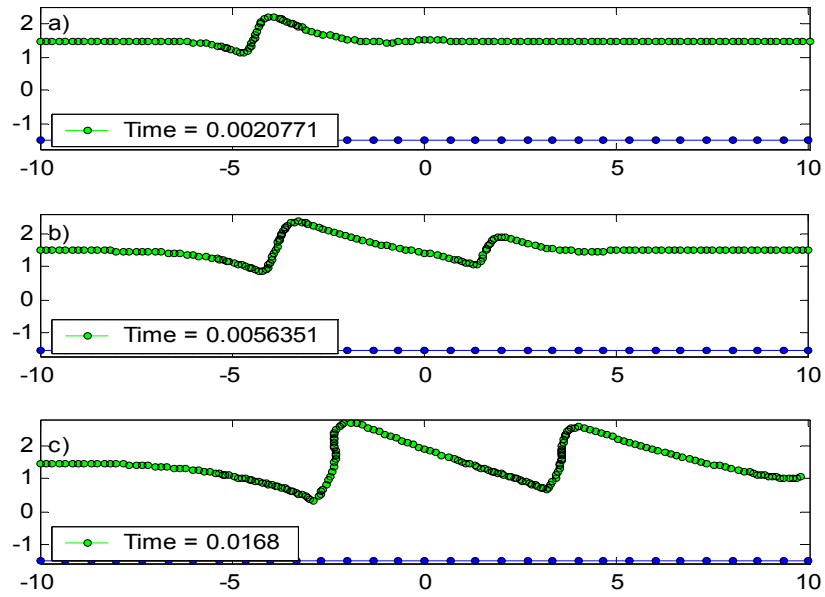


Figure A.10: * Result is shown for Hillock with $\chi = 50$, $A = 5$, $m = 2$, $\theta = 0$

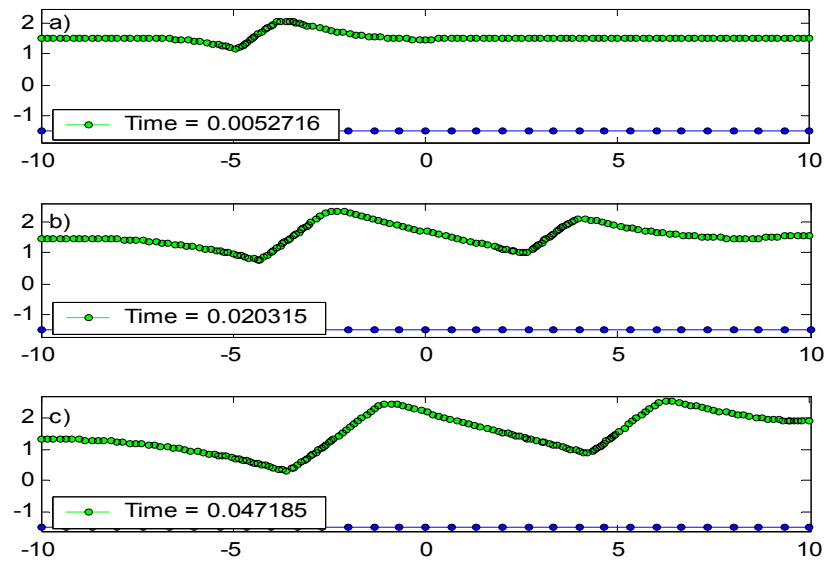


Figure A.11:* Result is shown for Hillock with $\chi = 25$, $A = 5$, $m = 3$, $\theta = 0$

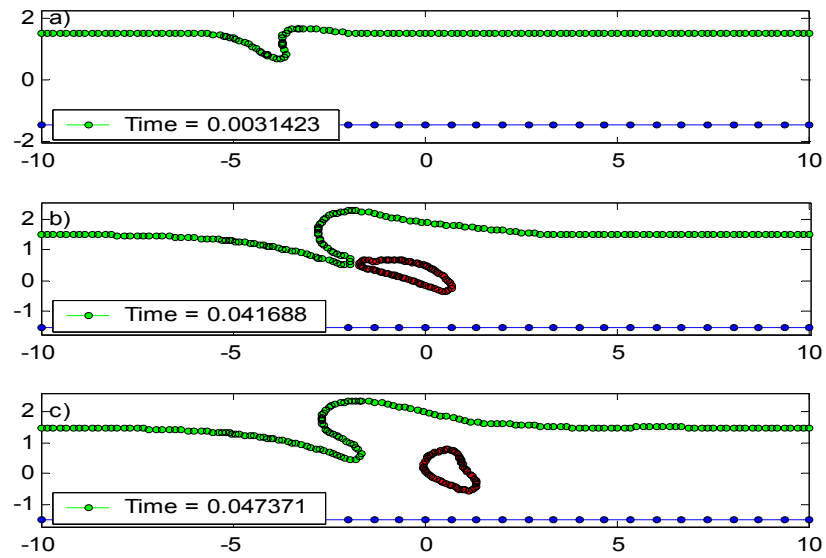


Figure A.12:* Result is shown for Edge Void with $\chi = 10$, $A = 5$, $m = 1$, $\theta = 0$

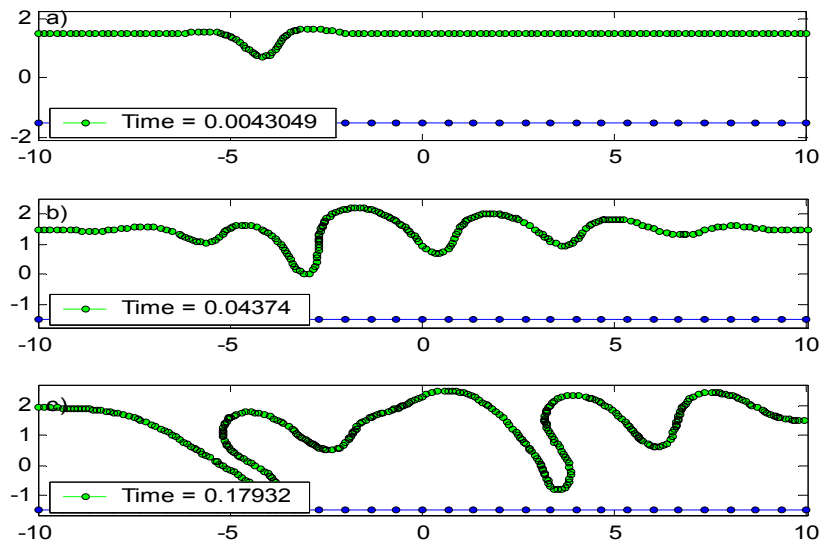


Figure A.13:* Result is shown for Edge Void with $\chi = 5$, $A = 10$, $m = 1$, $\theta = 135$

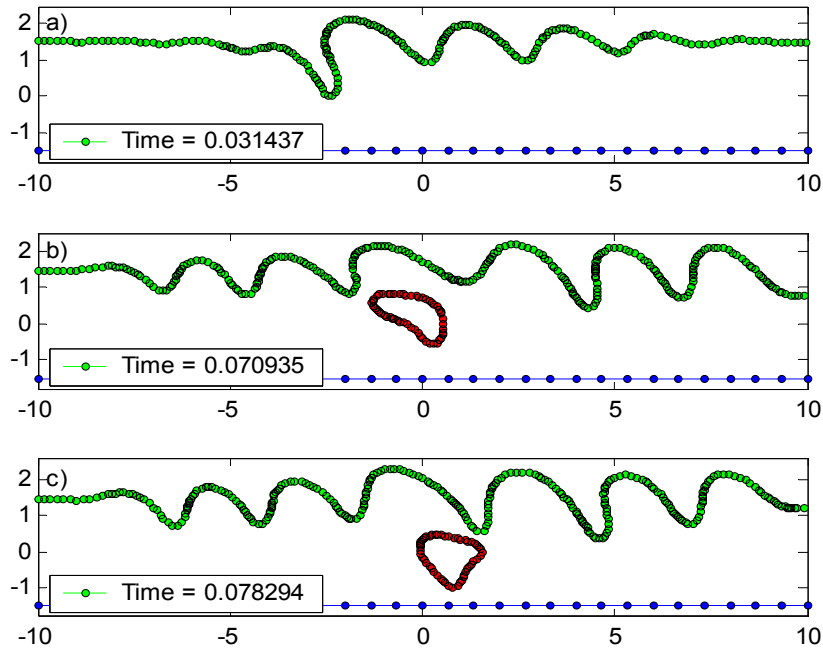


Figure A.14:* Result is shown for Edge Void with $\chi = 10$, $A = 5$, $m = 1$, $\theta = 135$

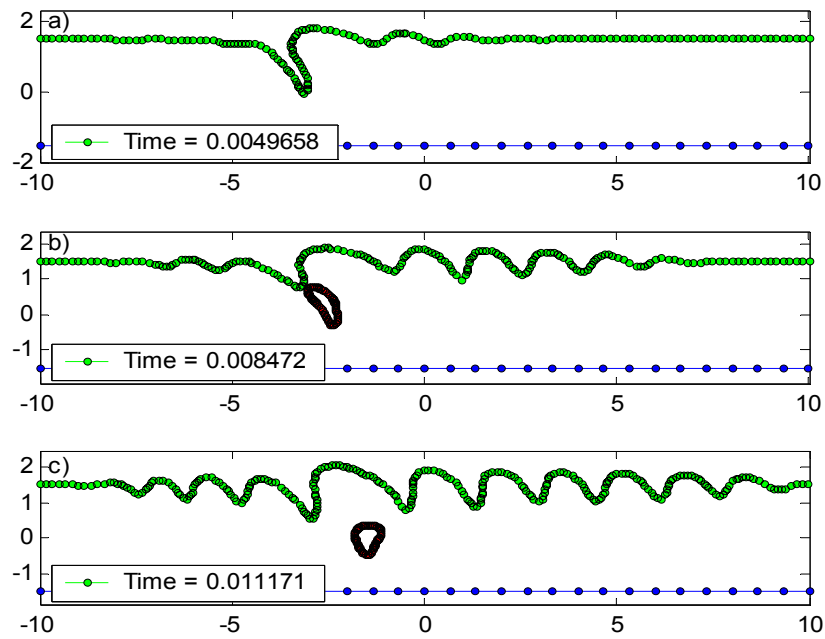


Figure A.15: * Result is shown for Edge Void with $\chi = 25$, $A = 5$, $m = 1$, $\theta = 135$

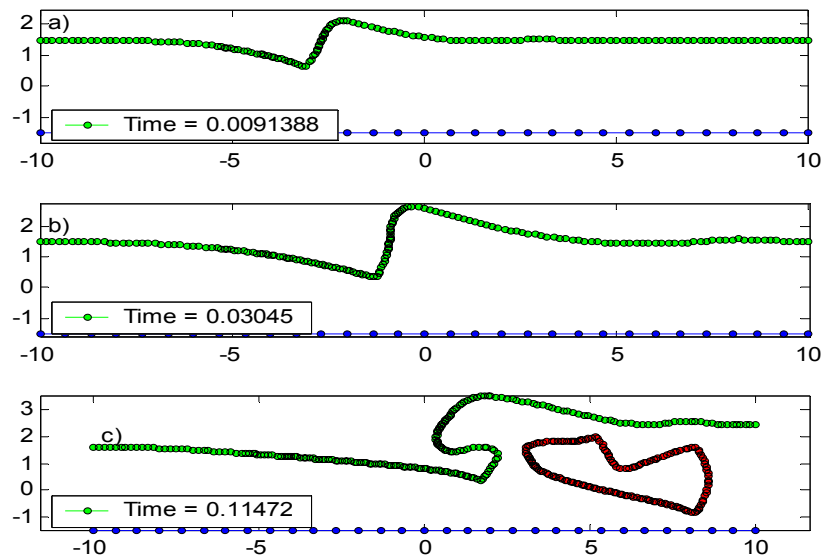


Figure A.16: * Result is shown for Edge Void with $\chi = 25$, $A = 5$, $m = 2$, $\theta = 0$

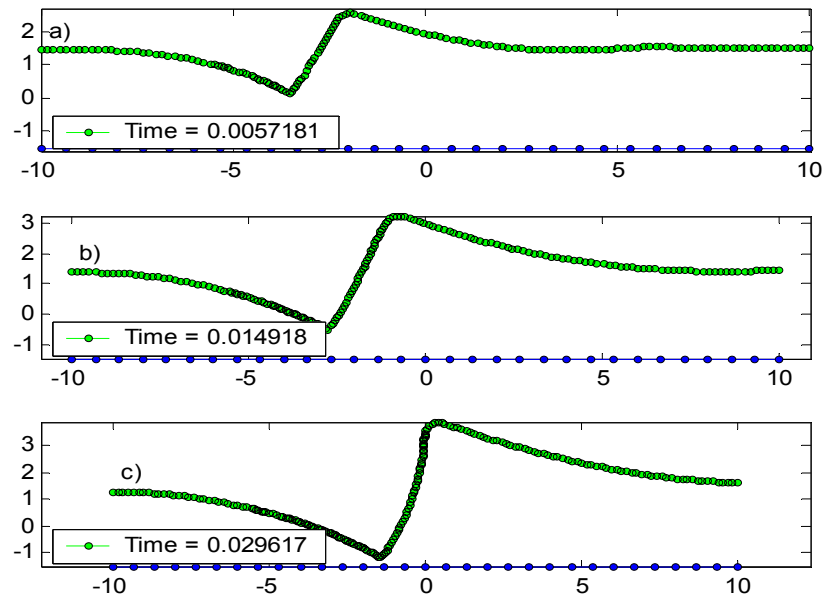


Figure A.17: * Result is shown for Edge Void with $\chi = 50$, $A = 10$, $m = 2$, $\theta = 0$

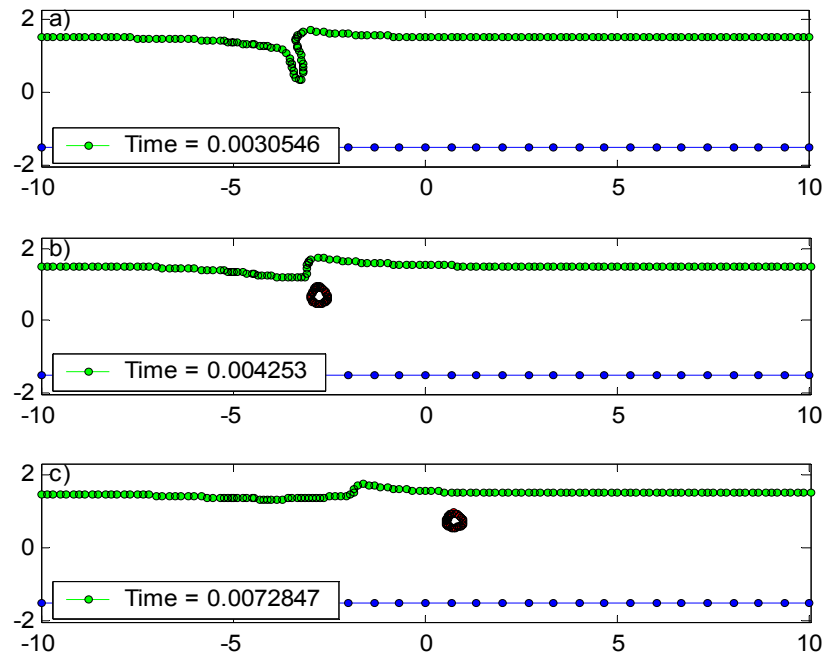


Figure A.18: * Result is shown for Edge Void with $\chi = 50$, $A = 5$, $m = 2$, $\theta = 30$

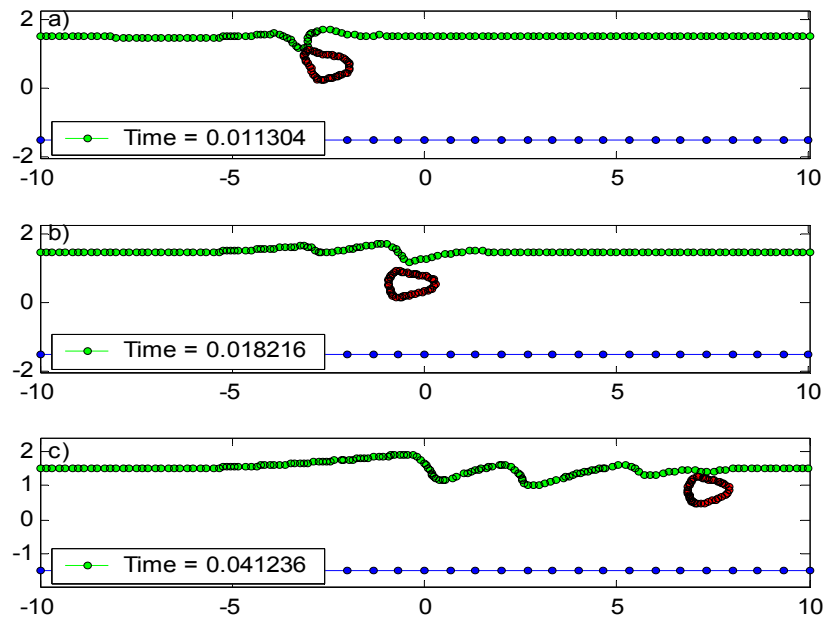


Figure A.19:* Result is shown for Edge Void with $\chi = 25$, $A = 5$, $m = 2$, $\theta = 45$

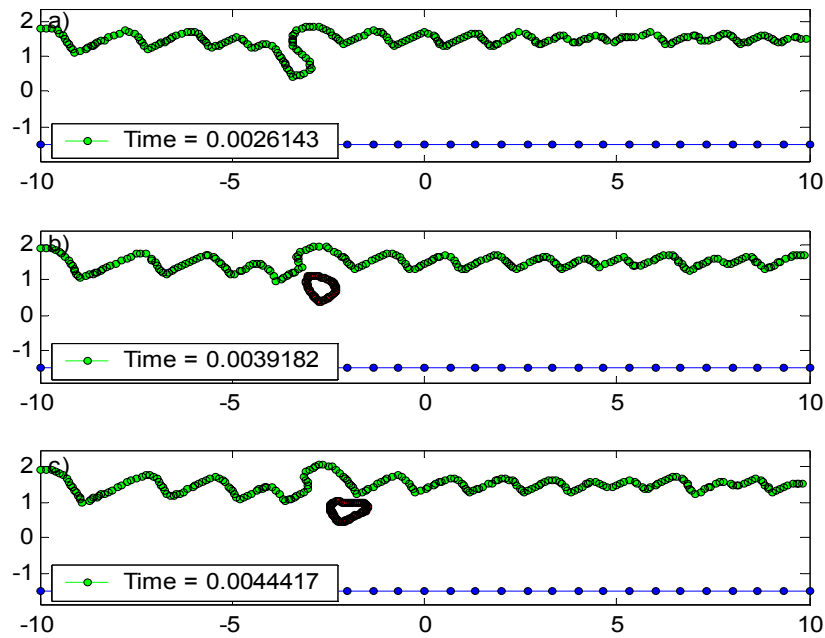


Figure A.20:* Result is shown for Edge Void with $\chi = 50$, $A = 10$, $m = 2$, $\theta = 60$

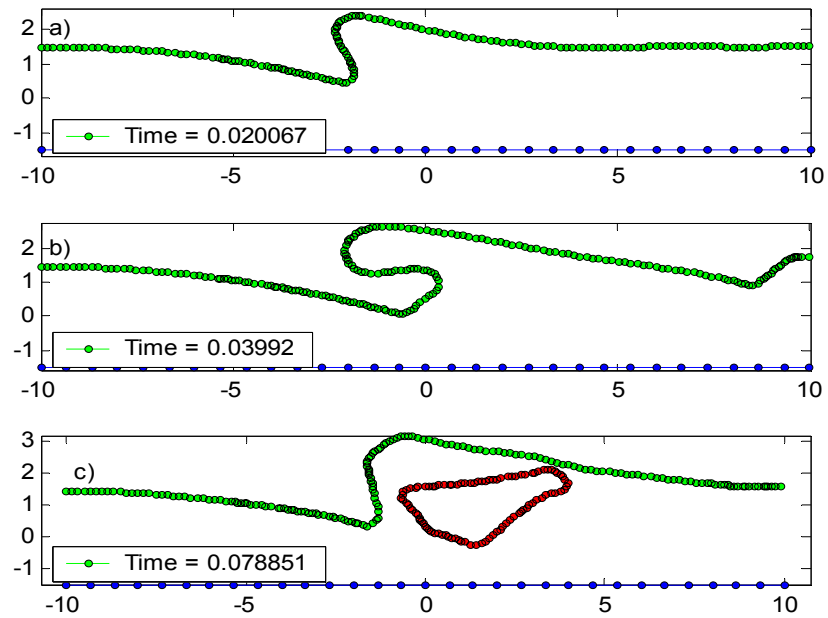


Figure A.21:* Result is shown for Edge Void with $\chi = 25$, $A = 5$, $m = 3$, $\theta = 0$

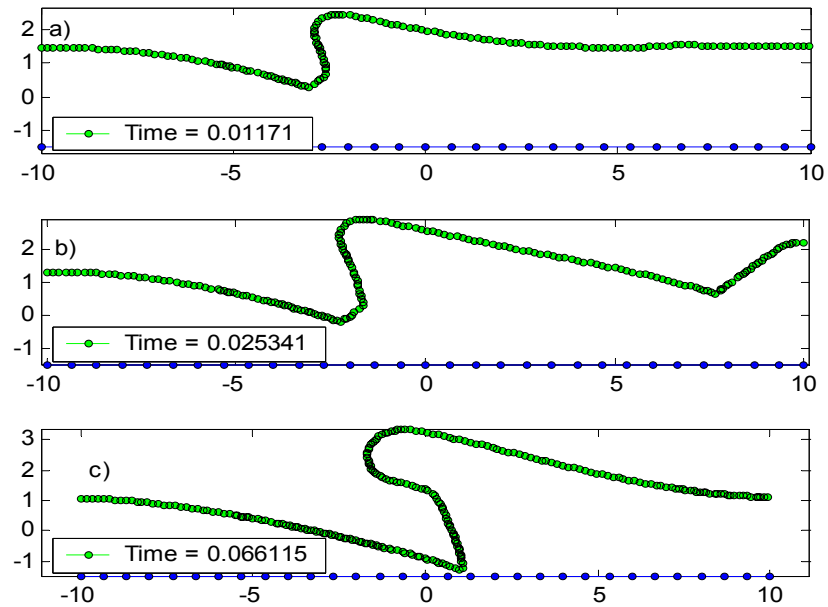


Figure A.22:* Result is shown for Edge Void with $\chi = 25$, $A = 10$, $m = 3$, $\theta = 0$

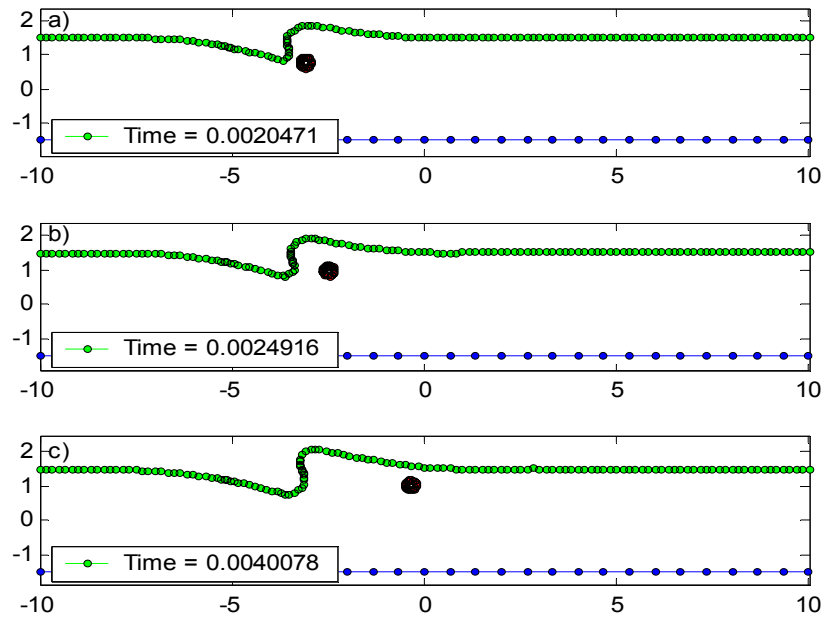


Figure A.23:* Result is shown for Edge Void with $\chi = 50$, $A = 5$, $m = 3$, $\theta = 0$

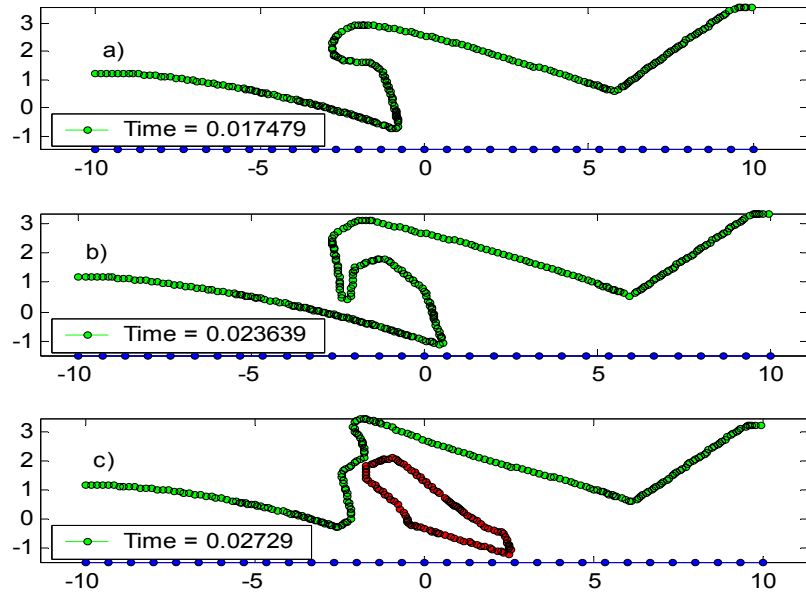


Figure A.24:* Result is shown for Edge Void with $\chi = 50$, $A = 10$, $m = 3$, $\theta = 0$

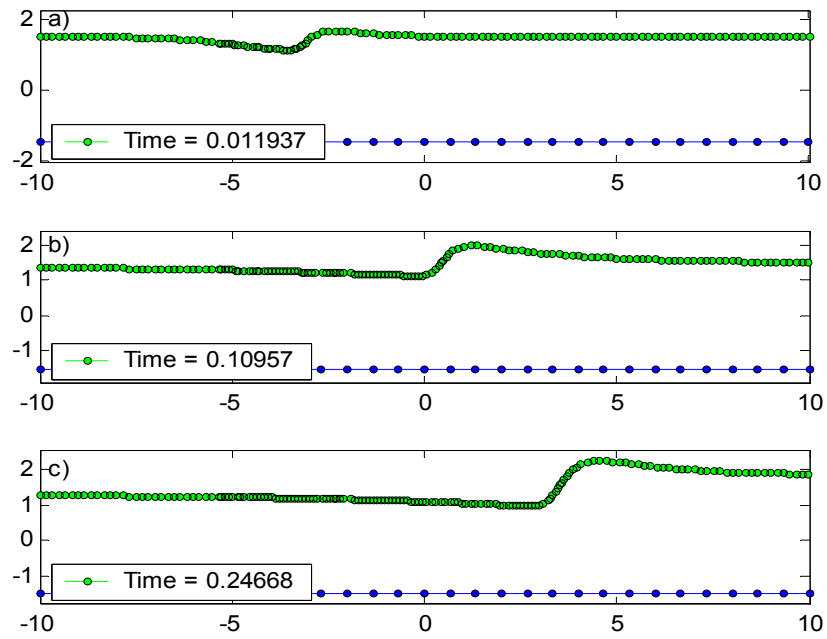


Figure A.25: * Result is shown for Edge Void with $\chi = 5$, $A = 10$, $m = 3$, $\theta = 15$

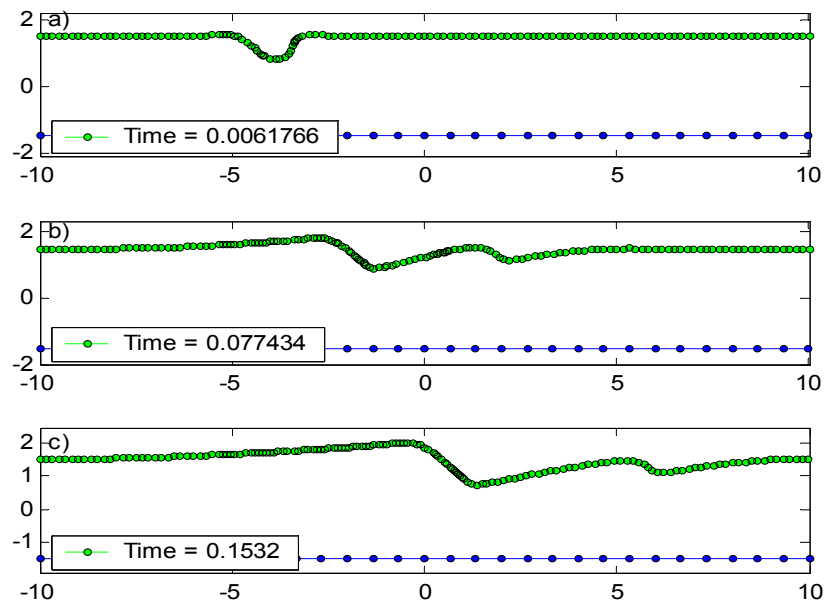


Figure A.26: * Result is shown for Edge Void with $\chi = 10$, $A = 5$, $m = 3$, $\theta = 30$

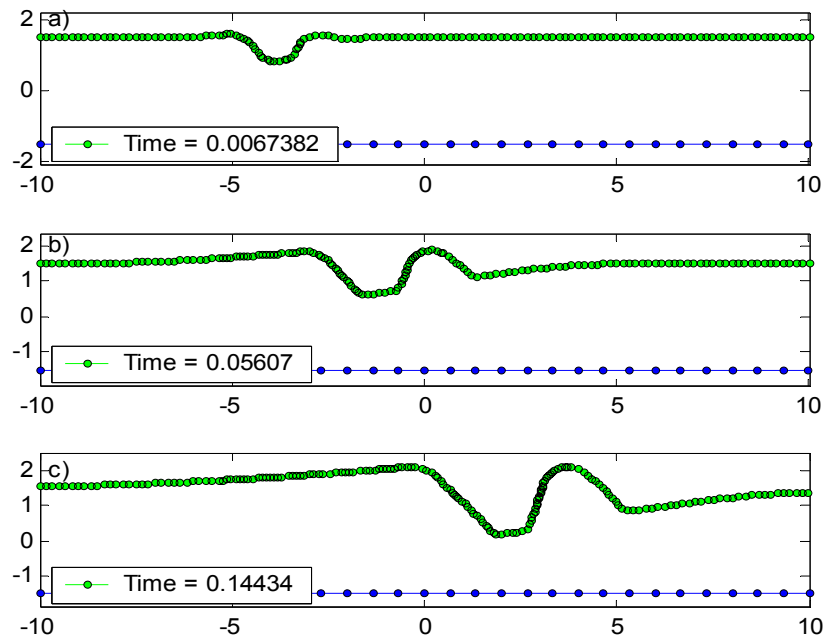


Figure A.27: * Result is shown for Edge Void with $\chi = 10$, $A = 10$, $m = 3$, $\theta = 30$

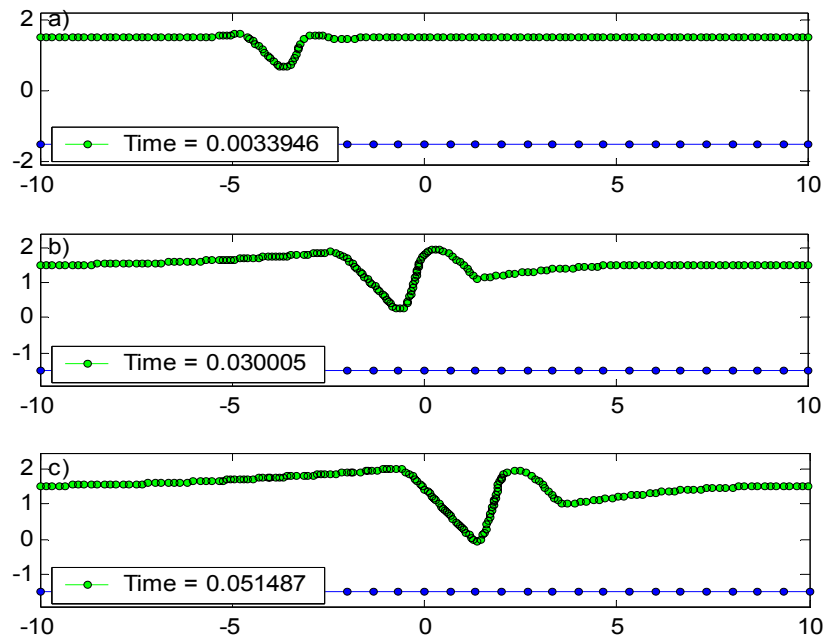


Figure A.28: * Result is shown for Edge Void with $\chi = 25$, $A = 5$, $m = 3$, $\theta = 30$

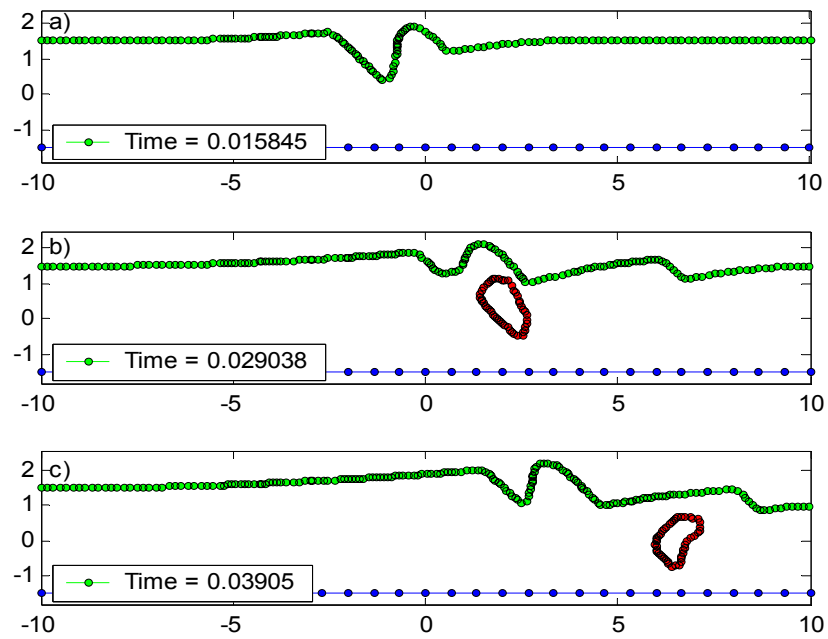


Figure A.29:* Result is shown for Edge Void with $\chi = 50$, $A = 5$, $m = 3$, $\theta = 30$

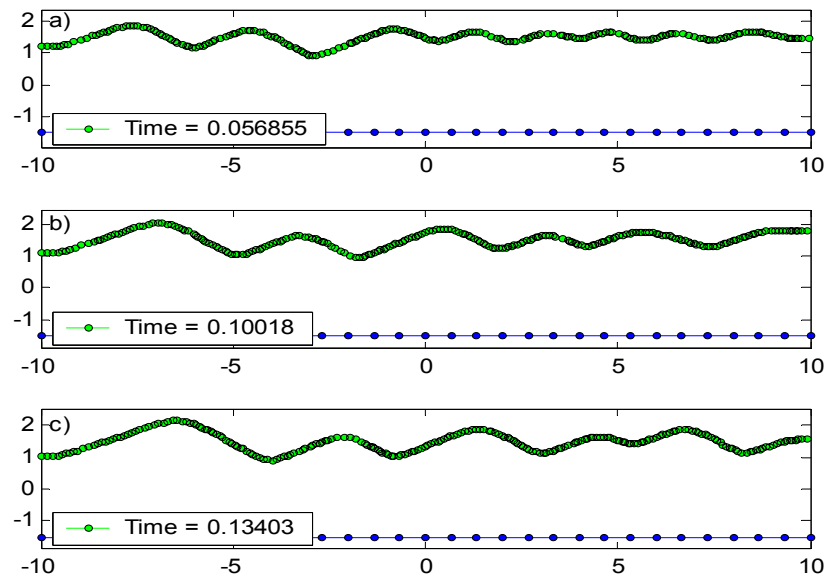


Figure A.30:* Result is shown for Edge Void with $\chi = 5$, $A = 10$, $m = 3$, $\theta = 45$

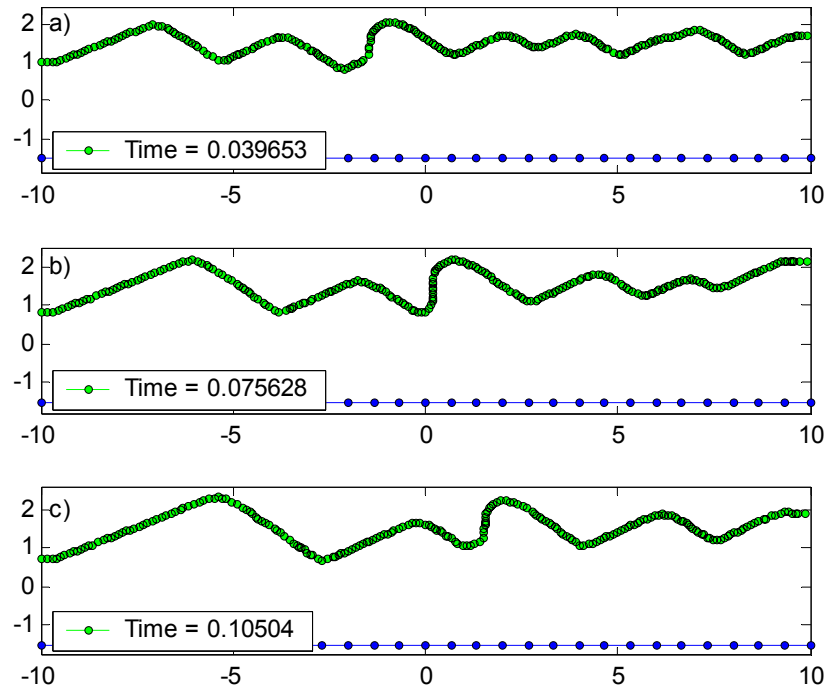


Figure A.31: * Result is shown for Edge Void with $\chi = 10$, $A = 10$, $m = 3$, $\theta = 45$